

UCSB SOUTH POLE 1994 CMB ANISOTROPY MEASUREMENT CONSTRAINTS
ON OPEN AND FLAT- Λ CDM COSMOLOGIES

Ken Ganga¹, Bharat Ratra², Joshua O. Gundersen^{3,4}, and Naoshi Sugiyama⁵

¹*Division of Physics, Mathematics and Astronomy, California Institute of Technology, Pasadena, CA 91125*

²*Center for Theoretical Physics, Massachusetts Institute of Technology, Cambridge, MA 02139*

³*Department of Physics, University of California, Santa Barbara, CA 93106*

⁴*Current address: Department of Physics, Brown University, Box 1843, Providence, RI 02912*

⁵*Department of Physics and Research Center for the Early Universe, University of Tokyo, Tokyo 113*

ABSTRACT

Motivated by steadily improving cosmic microwave background (CMB) anisotropy data, we develop general methods to account for experimental and observational uncertainties in the likelihood analysis of data from a CMB anisotropy experiment. To properly account for the uncertainties requires measured information about various distribution functions (e.g., the calibration distribution function) which in our preliminary analysis here we assume are gaussian.

We account for beamwidth and calibration uncertainties in the UCSB South Pole 1994 (SP94) experiment (Gundersen et al. 1995, hereafter G95), in likelihood analyses of the data (which we assume to be purely CMB anisotropy) that make use of model CMB anisotropy spectra in observationally-motivated, open and spatially-flat Λ , cold dark matter (CDM) cosmogonies.

For the model CMB anisotropy spectra we consider, the SP94 experiment is sensitive to the CMB anisotropy on a somewhat larger, model-dependent, angular scale than the effective angular scale at which the relevant zero-lag SP94 window by itself (i.e., without accounting for the CMB anisotropy spectrum) is most sensitive.

Ignoring calibration and beamwidth uncertainties, we repeat the nominal beamwidth, flat bandpower, likelihood analyses of G95 for the SP94 combined Ka, Q, and (full) Ka + Q data subsets, and derive bandtemperature central values and $\pm 1\sigma$ limits (using the equal tail prescription: $\sim 16\%$ of the area under the probability density distribution function

is below the -1σ limit, and $\sim 84\%$ is below the $+1\sigma$ limit). Our results are consistent with those of G95 to within the expected numerical uncertainty. For establishing the significance of a detection of CMB anisotropy we advocate deriving limits using the highest posterior density (HPD) prescription, since it yields smaller lower limits (here the $\pm 1\sigma$ limits are at equal probability density distribution values, and delimit the $\sim 68\%$ most likely range). (Even accounting for beamwidth and calibration uncertainties, and using the HPD prescription, the Ka, Q, and Ka + Q data show evidence for at least 3σ detections.) Since the HPD limits lead to tighter constraints on the sky signal amplitude, they also provide for greater discrimination between models.

Accounting for calibration and beamwidth uncertainties, the Ka + Q data set is most consistent with the CMB anisotropy shape in $\Omega_0 \sim 0.1 - 0.2$ open models (amongst all the models we consider here), and is not as consistent with those in old ($t_0 \gtrsim 15 - 16$ Gyr), high baryon density ($\Omega_B \gtrsim 0.0175h^{-2}$), low density ($\Omega_0 \sim 0.2 - 0.4$), flat- Λ models. Conclusions regarding model compatibility drawn from the SP94 Ka and Q data subsets are consistent with these results.

We do not have the resolution in model-parameter (Ω_0, h, Ω_B) space to actually construct the complete marginalized (over sky signal amplitude) probability density distribution (i.e., the probability density distribution function for just the cosmological parameters Ω_0, h , and Ω_B). To determine the viable range of these parameters we use the values computed for this marginal probability distribution at isolated points in model-parameter space, and assume that it is a gaussian in the model-parameter values. For the Ka, Q, and Ka + Q data subsets the CMB anisotropy shape in open CDM models with $\Omega_0 = 0.1 - 0.3$ and 0.4 (with a larger h and lower Ω_B), and in the flat bandpower model, ensures that these models are always within 1σ of the most likely low-density open model. Open models with $\Omega_0 = 0.5$ (with a smaller h and a larger Ω_B), fiducial CDM, and all flat- Λ models we consider, are always more than 1σ away from the most likely low-density open model. For the Ka, Q, and Ka + Q data subsets analyzed at the nominal beamwidths, the least likely model CMB anisotropy shape is always within $\sim 1.4 - 1.6\sigma$ of the most likely low-density open model, so the SP94 data do not rule out any of the models we consider here at the 2σ level. These results are qualitatively consistent with those from an analysis of all presently available CMB anisotropy detection data (Ganga, Ratra, & Sugiyama 1996, hereafter GRS).

Model normalizations deduced from the SP94 Ka, Q, and Ka + Q data subsets are mostly consistent with those deduced from the two-year COBE-DMR data, although the Ka data prefer a normalization $\sim 1\sigma$ lower than do the Q data, the Q (and Ka + Q) data favour a slightly higher normalization for the $\Omega_0 = 0.1$ open model than does the DMR, and the Ka (and Ka + Q) data prefer a somewhat lower normalization for the older, higher Ω_B , low-density Λ models than does the DMR. These effects are mostly consistent with the conclusions of GRS.

Accounting for the uncertainties, the SP94 Ka, Q, and Ka + Q data subsets have average $\pm 1\sigma$ HPD bandtemperature error bars $\sim 33 - 36\%$ (compared to $\sim 26 - 32\%$ when beamwidth and calibration uncertainties are ignored) for the flat bandpower model. Since calibration and beamwidth uncertainties, and sample variance, are large contributors, more sky coverage and an accurate determination of the calibration and beamwidth distribution functions should significantly reduce these error bars.

Subject headings: cosmic microwave background — cosmology: observations — large-scale structure of the universe

Submitted to *Astrophysical Journal*

1. INTRODUCTION

Low-density cold dark matter cosmogonies, either with flat spatial hypersurfaces and a cosmological constant Λ (Peebles 1993; Stompor, Górski, & Banday 1995; Scott, Silk, & White 1995; Ostriker & Steinhardt 1995; Ratra & Sugiyama 1995, hereafter RS), or with open spatial hypersurfaces and no Λ (Ratra & Peebles 1994; Kamionkowski et al. 1994; Górski et al. 1995; Liddle et al. 1996; Ratra et al. 1995, hereafter RBGS), are consistent with a fairly large fraction of present observational data.

These data include:

- measurements of the Hubble parameter H_0 ($= 100h \text{ km s}^{-1} \text{ Mpc}^{-1}$), which suggest $h > 0.55$ (e.g., Pierce & Jacoby 1995; Mould et al. 1995; Tanvir et al. 1995; Höflich & Khokhlov 1996; Baum et al. 1995; Whitmore et al. 1995, but also see, e.g., Nugent et al. 1995), and globular cluster age estimates which suggest that the age of the universe $t_0 > 11\text{Gyr}$ (e.g., Bolte & Hogan 1995; Jimenez et al. 1996; Chaboyer et al. 1995);

- dynamical estimates of the mass clustered on small scales $\lesssim 10h^{-1}\text{Mpc}$, which suggest $\Omega_0 \sim 0.05 - 0.35$ (Peebles 1993) [here the present value of the clustered-mass density parameter $\Omega_0 = 8\pi G\rho_b(t_0)/(3H_0^2)$, where G is the gravitational constant and $\rho_b(t_0)$ is the mean clustered-mass density now];
- estimates of Ω_0 from measurements of the plasma mass fraction of the rich clusters, standard nucleosynthesis theory, and the observed light element abundances (e.g., White & Fabian 1995; David, Jones, & Forman 1995);
- dynamical estimates of the mass clustered on scales $\gtrsim 10h^{-1}\text{Mpc}$ (e.g., Cole, Fisher, & Weinberg 1995; Loveday et al. 1995; Baugh 1995; there is, however, some scatter, see, e.g., Dekel et al. 1993; Shaya, Peebles, & Tully 1995);
- the shape of the observed galaxy fluctuation power spectrum (e.g., Peacock & Dodds 1994; Tadros & Efstathiou 1995);
- the observed cluster mass and correlation functions (e.g., Liddle et al. 1996; Viana & Liddle 1995);
- the presence of high redshift ($z \sim 0.5 - 1$) clusters (e.g., Mellier et al. 1994; Luppino & Gioia 1995; Smail & Dickinson 1995), high redshift ($z > 2$) galaxy groups (e.g., Francis et al. 1996; Pascarelle et al. 1996), high redshift ($z \gtrsim 3 - 4$) damped Lyman- α systems (e.g., Giallongo et al. 1994; Lu et al. 1996; Wampler et al. 1996), and the observed similarity of the giant elliptical luminosity functions at $z = 0$ and $z \sim 1$ (e.g., Djorgovski et al. 1995; Glazebrook et al. 1995; Lilly et al. 1995);
- the large-scale CMB spatial anisotropy measured by the COBE-DMR experiment and analyzed in the context of these cosmogonical models (e.g., Bunn & Sugiyama 1995; Górski et al. 1995; Stompor et al. 1995); and
- the smaller-scale CMB spatial anisotropy detected by a number of smaller angular scale experiments (RBGS; RS; GRS).

We emphasize that a number of the above observational estimates are still tentative, and some have large error bars. In particular, any individual set of measurements, by itself, does not have the power to seriously constrain the range of cosmological parameters like Ω_0 and h . It is only the combination of all these different measurements that indicates a low-density cosmogony is a more appropriate model of the universe.

Following the DMR discovery and measurement of the large-scale CMB anisotropy (Smoot et al. 1992; Wright et al. 1992; Bennett et al. 1996; Górski et al. 1996, and

references therein), and the confirmation by FIRS (Ganga et al. 1994), some attention has been focussed on attempts to use the two-year DMR data to constrain cosmologies which are consistent with other cosmological data (e.g., Bunn & Sugiyama 1995; Górski et al. 1995; Stompor et al. 1995; Yamamoto & Bunn 1995). While the two-year DMR data does allow for a much more accurate determination of the normalization of cosmological models than had previously been possible, it, by itself, does not have the discriminative power to significantly constrain other cosmological parameters.

Besides the DMR and FIRS measurements of the large-scale CMB spatial anisotropy, there are now a number of other detections of sky temperature anisotropy on smaller angular scales (Hancock et al. 1996; Piccirillo et al. 1996; Netterfield et al. 1996; G95; Ruhl et al. 1995; de Bernardis et al. 1994; Tanaka et al. 1995; Cheng et al. 1996; Griffin et al. 1996, and references therein). It is of some interest to determine whether these smaller-scale anisotropy measurements can help to significantly constrain cosmological model parameters. Given the error bars associated with these smaller-scale measurements (especially the calibration uncertainty), it is not surprising that even if one makes use of the DMR data to normalize cosmological models (and so fixes one free parameter), a preliminary examination shows that all the smaller-scale anisotropy experiments combined do not very significantly constrain other cosmological parameters (RBGS; RS; GRS). In particular, in a quantitative goodness-of-fit comparison of the CMB anisotropy predictions of two-year DMR-normalized, open and spatially-flat Λ , CDM models to all available CMB anisotropy detection observational data, GRS found that in most cases the 1σ uncertainty in the assumed value of the DMR normalization precludes robust conclusions about model viability.⁶

⁶It is interesting that the new four-year DMR results (Bennett et al. 1996; Górski et al. 1996, and references therein) indicate a normalization slightly lower than that found from the two-year DMR data (mostly a consequence of more detailed modelling of foreground Galactic emission — Banday et al. 1996; Kogut et al. 1996). From Figs. 5 and 6 of GRS which correspond to the models normalized at the -1σ value of the two-year DMR normalization (or, $\sim \sigma/3$ below the nominal value of the four-year DMR normalization), one sees that most models considered by GRS (and here) are consistent, in the goodness-of-fit sense, with the set of all presently available small-scale CMB anisotropy detection data. As four-year DMR normalizations for the open and spatially-flat Λ models are not

This comparison between the theoretical predictions of a model and the smaller-scale sky temperature spatial anisotropy observational data (RBGS; RS; GRS) did not make use of the complete data from each experiment. Rather, it typically made use a single number (with error bars) related to the rms of the temperature spatial anisotropy detected by the experiment. There are two significant issues related to such a sparse representation of the observational data from an experiment. Since the procedure used to extract this single number from the observational data set assumes a form (not necessarily realistic) for the sky temperature spatial anisotropy spectrum (the low signal-to-noise of present data ensures that some such assumption is needed to process the data), typically a gaussian autocorrelation function (although it is now becoming more fashionable to assume a flat bandpower spatial anisotropy angular spectrum), it is of interest to examine how sensitively the final result depends on this assumption (the low signal-to-noise also indicates that there might not be a lot of sensitivity to the assumed functional form), and in particular to determine the result using more realistic forms for the sky anisotropy angular spectrum (e.g., computed in cosmogonies that are consistent with non-CMB observational data). Secondly, although the experiments are sensitive to a range of spatial scales, representing the observational data by a single number effectively discards this additional (spatial correlation) information; it is therefore also of interest to examine whether, if one assumes a model for the sky temperature spatial anisotropy spectrum, this additional spatial correlation information in the observational data allows for a discrimination between different assumed forms for the sky temperature spatial anisotropy.

In this paper we address these issues for the SP94 data set of G95, using theoretical CMB primary spatial anisotropy spectra derived in gaussian, adiabatic, open and spatially-flat Λ , CDM cosmogonies (RBGS; RS).⁷ The SP94 windows are sensitive to the CMB spatial anisotropy on angular scales where the open and flat- Λ model CMB spatial anisotropy spectra are not very scale dependent, so we expect only a weak dependence of the deduced sky signal amplitude on the assumed CMB anisotropy shape.

yet available, in this paper we use the two-year DMR normalizations, when needed.

⁷ Bond & Jaffe (1996) have also analyzed the SP94 data (D. Bond, private communication 1995), mostly making use of CMB anisotropy spectra in spatially-flat models, but considering a wider variety of these models than we have here. A summary of some of their results may be found in Bond (1995).

SP94 is the most recent of the SP CMB anisotropy experiments at the South Pole. The observational results of SP89 are discussed by Meinhold & Lubin (1991) and Meinhold et al. (1993) (this paper includes a description of the ACME telescope used in the SP experiments). An analysis of the SP89 data, in the context of fiducial, scale-invariant, spatially-flat CDM models, and some isocurvature models, is given in Vittorio et al. (1991) and Bond et al. (1991). The SP91 observational results are in Gaier et al. (1992) and Schuster et al. (1993). The Gaier et al. data have been analyzed in the context of fiducial CDM by Górski, Stompor, & Juszkiwicz (1993), Muciaccia et al. (1993) (who also consider tilted CDM models), Dodelson & Jubas (1993), Bunn et al. (1994), and Stompor & Górski (1994) (who also consider the now more fashionable spatially-flat Λ CDM models and also analyze the Schuster et al. data). These analyses only used the data from the highest-frequency channel of the SP91 scans to draw conclusions about the CMB anisotropy. Off-diagonal channel-channel noise correlations were accounted for in the multifrequency reanalysis of SP91 given in G95 (who made use of the flat bandpower approximation for CMB spatial anisotropy). The inclusion of these off-diagonal correlations has little effect on the most probable sky signal amplitude; however, they increase the $\pm 1\sigma$ error bars by $\sim 20\%$.

The SP94 experiment extends the SP91 frequency range by also taking data with a Q-band receiver (in addition to that taken with a Ka-band receiver). Descriptions of the SP94 experiment may be found in Gundersen et al. (1994), G95, and Gundersen (1995). The far-field beam patterns of the Ka-band and Q-band radiometers, coupled to the ACME telescope, were measured in both azimuth and elevation (at 27.7 GHz for Ka and 41.5 GHz for Q). These measurements indicate that in both azimuth and elevation the beams are well-approximated by gaussians down to 30 dB (Gundersen 1995), so here we assume that the beams are gaussian. The beamwidths measured in azimuth and elevation differ from the average beamwidth by $\sim 1.5 - 2\%$ (at one standard deviation), and in our preliminary analysis here we do not explicitly account for this ellipticity but assume circular beams (with beamwidth errors bars that do take account of this difference between the beamwidths measured in azimuth and elevation). Multifrequency beam patterns estimated from observations of the Moon with the Q-band system, and observations of the Eta Carina region with both systems, are consistent with the far-field beam measurements. (Far-field multifrequency two-dimensional beam maps of the far side lobes have not been

made.) Based on the one-dimensional far-field measurements of the beam patterns, the main beam efficiency is estimated to be $> 98\%$. The $< 2\%$ loss to the beam side lobes is not corrected for in our analysis here. A more detailed discussion of these issues may be found in Gundersen (1995).

The Ka-band (26 – 36 GHz) is multiplexed into four channels centered at $\nu = 27.25$, 29.75, 32.25, and 34.75 GHz, with 3 dB bandwidths of 2.5 GHz. The measurements described above indicate that the individual Ka channels have a frequency-dependent gaussian beamwidth $\sigma_G^{(\text{Ka})} \equiv \sigma_{BW}^{(\text{Ka})} \times [27.7 \text{ GHz}/\nu] = (0.70 \pm 0.04)^\circ \times [27.7 \text{ GHz}/\nu]$ (one standard deviation error). The Q-band (38 – 45 GHz) is multiplexed into three equal-width channels centered at $\nu = 39.15$, 41.45, and 43.75 GHz with 3 dB bandwidths of 2.3 GHz and a frequency-dependent gaussian beamwidth $\sigma_G^{(\text{Q})} \equiv \sigma_{BW}^{(\text{Q})} \times [41.5 \text{ GHz}/\nu] = (0.47 \pm 0.04)^\circ \times [41.5 \text{ GHz}/\nu]$ (one standard deviation error). The measured passband central frequency errors are $\sim 1\%$, and are ignored in our analysis. Far-field measurements of the Ka- and Q-band beamwidths were performed at 27.7 and 41.5 GHz respectively. We therefore assume that all four Ka-band beamwidth uncertainties, and all three Q-band beamwidth uncertainties, shift together. However, the Ka-band and Q-band beamwidth uncertainties do not necessarily shift together (since the Ka and Q measurements were performed consecutively, with different horns, but with the same telescope optics). We emphasize that, as noted above, beam patterns estimated from multifrequency observations of the Moon and the Eta Carina region were consistent with the far-field beam measurements.

The SP94 Q and Ka observations were performed consecutively. Since the multiplexing was done after amplification and initial filtering, the HEMT amplifiers and the atmosphere introduce significant intraband channel-channel correlations, which are accounted for in the analysis.

Unlike the stepped scans of SP89 and SP91, SP94 data were taken during smooth, azimuthal, constant declination, constant velocity scans, extending 20° on the sky. While observing, the beam was sinusoidally chopped, with a half peak-to-peak chop amplitude of 1.5° on the sky. The rms fractional uncertainty in the peak-to-peak chop angle was measured to be 0.04% , and is ignored in our analysis. The two-beam/single-difference data were binned into 43 bins, with a binsize of $(20/43)^\circ$ on the sky. As discussed in G95, the relative-pointing uncertainty “on the sky” is $\pm 0.02^\circ$ in azimuth and $\pm 0.05^\circ$ in

elevation, and is ignored in our analysis here. The absolute-pointing uncertainty on the sky is $\pm 0.12^\circ$ in azimuth and in elevation (G95). The absolute-pointing uncertainty is irrelevant for either the Ka- or Q-scan data analyses, but could be a significant issue when the Ka and Q data are combined for the Ka + Q analysis, or when comparing the results of the Ka and Q analyses. However, for reasons discussed below, this is ignored in our analysis here.

The G95 data were taken in smooth scans of $\pm 10^\circ$ on the sky centered at $\alpha = 45^\circ$ and $\delta = -61.8^\circ$ (1994), with a total sky coverage $\sim 20 \text{ deg}^2$. After data editing as described in G95 (which resulted in the removal of $\sim 25\%$ of the data — less for Ka, more for Q — and left 88 h and 108 h of usable Ka- and Q-band data respectively), an offset and linear gradient were removed from the data for each channel and each scan (of angular extent 20° on the sky; we note that the SP group sometimes calls this a half-scan), and for each channel the binned data from the individual scans were coadded (G95). The data were also corrected for atmospheric absorption (G95). This is the reduced data we analyze in this paper.

G95 describe the various tests that were used to examine the integrity of the data and the various tests that indicate that the signal they see is on the sky. These include studying the data binned in heliocentric and azimuthal coordinates, as well as comparing a variety of subsets of the data, including those divided by time, and by telescope azimuthal position. G95 also estimate the contamination expected from Galactic diffuse synchrotron emission, from the Sunyaev-Zel'dovich effect, and from Galactic 20 K dust emission, and show that these are small compared to the signal they see. A more detailed discussion of these tests may be found in Gundersen (1995).

While in our analysis here we assume that the SP94 data is purely CMB anisotropy, it is prudent to bear in mind that one cannot yet conclusively rule out a small amount of undetected, non-CMB, contamination in the data. The G95 time subset check, which shows that when the data is divided into 4, approximately equal, contiguous time series, all 4 subsets are mutually consistent, and also that all combinations of 3 of the 4 subsets are mutually consistent, indicates that transient atmospheric phenomena are not that significant an issue. However, G95 could not rule out non-CMB foreground discrete radio source contamination (see Gundersen et al. 1996 for a discussion of the effects of discrete radio source contamination).

The Ka-band and Q-band radiometers were calibrated (output voltage as a function of temperature input: V/K) using a combination of different methods. Without the ACME telescope, the radiometer V/K were determined for an ambient temperature Eccosorb load and for a liquid nitrogen cold load. These were used in combination with sky zenith scans, and an atmosphere model, to determine the atmospheric contribution to the antenna temperature and to derive a sky zenith temperature. The sky zenith scans were performed with the radiometers coupled to the ACME telescope. The calibration of the radiometers determined from the three different combinations of ambient load, cold load, and sky load, were found to have a relative (channel to channel) uncertainty of 3% and an absolute uncertainty of 10% (one standard deviation). This determination of the calibration was consistent with that determined from a cryogenic termination that was used to produce a load similar to that of the sum of the atmosphere and the CMB.^{8,9} A more detailed discussion of these points may be found in Gundersen (1995). In what follows, we treat the absolute-radiometer-calibration uncertainty as an additional, purely statistical, uncertainty to be included in the likelihood analyses.

Besides accounting for beamwidth and calibration uncertainties, and using CMB spatial anisotropy spectra in observationally motivated cosmologies, our analysis differs from that of G95 in two other respects. Unlike G95, we do not make use of data-weighted windows to quote limits, and we also use a different statistical prescription to determine limits from the probability density distribution functions. A more detailed discussion of these points is given in §2 below.

In the next section we outline the computational techniques used in our analyses here. Our results, and a discussion of them, is in §3, and we conclude in §4.

⁸ Measured microwave emission from the Moon was consistent with a model of the Moon's emission (Keihm 1983) to within the uncertainty ($\sim 20\%$).

⁹ Some CMB anisotropy experiments calibrate on a point source to determine V/Jy. SP94 does not do this, so for SP94 the beamwidth uncertainty does not influence the calibration uncertainty. In our analysis here, the SP94 beamwidth and radiometer-calibration uncertainties are treated as independent sources of uncertainty.

2. COMPUTATION

Using the spherical harmonic decomposition of the CMB spatial anisotropy fractional temperature perturbation, $\delta T/T$, as a function of angular position (θ, ϕ) on the sky,

$$\frac{\delta T}{T}(\theta, \phi) = \sum_{l=2}^{\infty} \sum_{m=-l}^l a_{lm} Y_{lm}(\theta, \phi), \quad (1)$$

we may characterize the CMB spatial anisotropy (in a gaussian model) by the dimensionless angular fluctuation spectrum C_l , which is defined in terms of the ensemble average of the dimensionless expansion coefficients,

$$\langle a_{lm} a_{l'm'}^* \rangle = C_l \delta_{ll'} \delta_{mm'}. \quad (2)$$

One would like to use the SP94 anisotropy observations to measure the C_l s over that range of l where the experiment is sensitive to the anisotropy. However, the broad width of the SP94 windows and the limited sky coverage prevents one from extracting from the SP94 data the value of each individual C_l that the experiment is sensitive to. It is therefore necessary to assume a functional form for the C_l s over the range of l which SP94 is sensitive to, with the normalization ($\propto T_0 \sqrt{C_2}$, where T_0 is the CMB temperature now) allowed to be a free parameter, and with the shape of the C_l allowed to depend on free shape parameters. One may then compare these C_l s to the spectrum of the SP94 data and determine the value of the normalization and the values of the shape parameters (amongst those considered) which best reproduce the data spectrum.

On large angular scales, when the effects of the pressure of the photon-baryon fluid (and matter velocity perturbations at photon decoupling) can be ignored, a reasonably accurate approximation to the CMB anisotropy spectrum in the fiducial CDM model is provided by the flat CMB angular spectrum (Peebles 1982),

$$C_l = \frac{6C_2}{l(l+1)} = \frac{24\pi}{5} \frac{(Q_{\text{rms-PS}}/T_0)^2}{l(l+1)}, \quad (3)$$

where $Q_{\text{rms-PS}}$ is the corresponding quadrupole-moment amplitude of the model CMB anisotropy. This angular spectrum, normalized to best reproduce the two-year (galactic coordinates, quadrupole-excluded) DMR sky maps (Górski et al. 1994) is shown in Fig. 1 (line labelled “Flat”). The 1σ two-year DMR range for $Q_{\text{rms-PS}}$ in this model is given in, e.g., column (2) of Table 16 (last line, labelled “Flat”).

The fiducial CDM model is an Einstein-de Sitter model with gaussian, adiabatic, scale-invariant energy density perturbations (Harrison 1970; Peebles & Yu 1970; Zel'dovich 1972), with standard recombination (Peebles 1993, §6), Hubble parameter $h = 0.5$, and baryon density parameter $\Omega_B = 0.0125h^{-2}$. [Scale-invariant energy density perturbations are generated by quantum-mechanical fluctuations during an early epoch of inflation in a variety of spatially-flat inflation models (e.g., Fischler, Ratra, & Susskind 1985).¹⁰] The primary CMB anisotropy angular spectrum in this model (O14 in Table 2), normalized to best reproduce the two-year (galactic coordinates, quadrupole-excluded) DMR sky maps (Górski et al. 1995), is shown in Fig. 1 (line labelled O14). The 1σ two-year DMR range for $Q_{\text{rms-PS}}$ in the fiducial CDM model is given in, e.g., column (2) of Table 20 (line labelled O14); the corresponding ecliptic-coordinate-normalization values may also be found in this Table (line labelled Λ 12).¹¹ The fiducial CDM model is no longer thought to provide an adequate representation of the observed universe (see discussion at the beginning of §1, and references cited there).

On the other hand, as discussed in the Introduction, low-density open and flat- Λ CDM cosmogonies are consistent with present observational data. For historical reasons (Guth 1981, also see Kazanas 1980; Sato 1981a,b), no longer valid (Gott 1982; Guth & Weinberg 1983),¹² the low-density Λ CDM models considered here are taken to have

¹⁰ It used to be thought that agreement with observational data required an extremely small coupling constant for the inflaton field during inflation. It has since been realized that this is not necessary, and that the small observed CMB anisotropy could, quite generally, be a consequence of the small ratio of the inflation-epoch mass scale to the Planck mass (e.g., Ratra 1991, and references therein). It may be significant that a similar mechanism does seem to be realized in superstring-inspired inflation models (Banks et al. 1995).

¹¹ The galactic- and ecliptic-coordinate DMR maps are slightly different, and this results in a small difference, $\lesssim 0.6 \mu\text{K}$, between the $Q_{\text{rms-PS}}$ values (for the fiducial CDM model) deduced from the two sets of maps (Bennett et al. 1996, and references therein). This difference is manifest in the DMR results for fiducial CDM models O14 and Λ 12 (see the corresponding entries in, e.g., col. [2] of Table 16), which have identical CMB spatial anisotropy spectra, but are normalized using the different maps.

¹² While Gott (1982) and Guth & Weinberg (1983) constructed simple open inflation models, there is also an argument that suggests that if the pre-inflation spatial sections

flat spatial sections, and so the simplest power spectrum for gaussian, adiabatic, energy-density perturbations in these models is the scale-invariant one (and such a spectrum is generated by quantum zero-point fluctuations during an early epoch of inflation in a spatially-flat inflation cosmogony). The simplest spectrum for gaussian adiabatic energy-density perturbations consistent with open spatial sections is that generated by zero-point fluctuations during an early epoch of inflation in an open model (Ratra & Peebles 1994, 1995; Bucher, Goldhaber, & Turok 1995; Lyth & Woszczyna 1995; Yamamoto, Sasaki, & Tanaka 1995; Bucher & Turok 1995).

The values of the parameters Ω_0 , h , and Ω_B (listed in col. [2] of Table 2), which characterize the primary CMB C_l spectra in these low-density CDM models, are chosen to be roughly consistent with present observational estimates of Ω_0 , h , the age of the universe, and the constraints on Ω_B that follow from the observed light element abundances in the standard nucleosynthesis model (RBGS; RS). Two standard-recombination open model C_l spectra (for $\Omega_0 = 0.2$ and 0.5 , $h = 0.75$ and 0.55 , $\Omega_B h^2 = 0.0075$ and 0.0175 , respectively; models O4 and O11 in Table 2) and two standard-recombination, flat- Λ model C_l spectra (for $\Omega_0 = 0.2$ and 0.4 , $h = 0.8$ and 0.55 , $\Omega_B h^2 = 0.0075$ and 0.0175 , respectively; models $\Lambda 2$ and $\Lambda 10$ in Table 2) are shown in Fig. 1. The Λ model C_l s are normalized to the two-year (ecliptic coordinates, quadrupole-excluded) DMR sky maps (Bunn & Sugiyama 1995; also see RS), while the open model C_l normalization uses the galactic coordinates, quadrupole-excluded, maps (Górski et al. 1995; also see RBGS). The 1σ two-year DMR range of $Q_{\text{rms-PS}}$ for these models may be found in, e.g., column (3) of Table 23.

To simplify the comparison to SP94 data, effects of tilt, primordial gravity waves, and reionization are ignored here. This is because in this preliminary analysis we wish to draw conclusions about parameters representing effects that must exist (i.e., Ω_0 , h , and Ω_B). While it is always possible to get a better fit to data by including additional free parameters in a model, we do not believe that constraining models with more than the least possible number of free parameters is as yet warranted. Furthermore, tilt, gravity waves, and early reionization are unlikely to be significant in viable open models, although

were not flat, then, without inordinate fine-tuning, inflation models do not have enough e -foldings during inflation to flatten them (J. R. Gott, private communication 1994). As recently emphasized by Banks et al. (1995), this is indeed what happens in superstring-inspired inflation models.

there are mild indications that some such effect might be required to bring some spatially-flat Λ CDM models into agreement with observational data (Stompor et al. 1995; Scott et al. 1995; Ostriker & Steinhardt 1995; RS; Klypin, Primack, & Holtzman 1995; GRS). We emphasize that any effect which significantly modifies the shape of the C_l used in our analysis here (e.g., isocurvature perturbations, mildly nongaussian CMB anisotropy, etc.) will affect the final results.

The general procedure for the computation of the primary CMB anisotropy angular spectra is discussed by Sugiyama (1995). A discussion of the various assumptions and approximations involved in such a computation (as well as a discussion of the resulting accuracy of the computation), in the fiducial CDM model, may be found in Hu et al. (1995).

Figure 2 shows the zero-lag windows W_l (from eq. [1] of G95) for the seven individual SP94 channels, for the nominal beamwidths. [These are slightly more accurate ($\sim 0.5-2\%$, depending on channel) than those used in G95.] In Fig. 2 we also show the uncertainties, due to the one standard deviation beamwidth uncertainties, in the two windows sensitive to the largest and smallest angular scale CMB spatial anisotropy.

It has become conventional to summarize CMB spatial anisotropy experiment windows in terms of a few parameters (e.g., Bond 1996). These are the peak multipole l_m (the value of l where W_l is at the maximum), the two $l_{e-0.5}$ where $W_{l_{e-0.5}} = e^{-0.5}W_{l_m}$, and the effective multipole $l_e = I(lW_l)/I(W_l)$ where

$$I(W_l) = \sum_{l=2}^{\infty} \frac{(l+0.5)W_l}{l(l+1)}. \quad (4)$$

The values of these parameters, for the nominal and upper and lower one standard deviation beamwidth, individual channel, zero-lag SP94 windows are given in Table 1.¹³ We emphasize that the W_l used here assume that the SP94 beam is gaussian and do not explicitly account for the small ellipticity. Given the other uncertainties, these are very reasonable approximations.

¹³ Note that in our internal computations these (and other) numerical values are not truncated at 2 or 3 significant figures as in the Tables; as a consequence, when the truncated numerical values of the Tables are used to rederive some of our results there will be small differences from the values listed in the Tables.

The range of multipole moments which a CMB spatial anisotropy experiment is sensitive to depends on both the window W_l and the sky signal C_l . So, depending on the form of the sky signal, the window parameters l_e , l_m , and $l_{e-0.5}$ do not necessarily give a good indication of the multipoles l a CMB spatial anisotropy experiment is sensitive to.

CMB spatial anisotropy experiments are sensitive to δT_{rms} , the rms of the sky temperature anisotropy seen through their window,

$$(\delta T_{\text{rms}})^2 = \sum_{l=2}^{\infty} (\delta T_{\text{rms}}^2)_l, \quad (5)$$

where

$$(\delta T_{\text{rms}}^2)_l = T_0^2 \frac{(2l+1)}{4\pi} C_l W_l, \quad (6)$$

and $T_0 = 2.726 \pm 0.010$ K (Mather et al. 1994). Given a model of the CMB spatial anisotropy C_l , $(\delta T_{\text{rms}}^2)_l$ provides a convenient way of establishing the (approximate, since it ignores spatial correlation information) range of multipoles l a CMB spatial anisotropy experiment is sensitive to. In Fig. 3 we plot $(\delta T_{\text{rms}}^2)_l$ for the larger beamwidth (upper one standard deviation) Ka1 and smaller beamwidth (lower one standard deviation) Q3 channel W_l , for the models shown in Fig. 1. In Table 2 we list l_m , the value of l at which $(\delta T_{\text{rms}}^2)_l$ is at a maximum, and $l_{e-0.5}$ the two multipoles where $(\delta T_{\text{rms}}^2)_{l_{e-0.5}} = e^{-0.5} (\delta T_{\text{rms}}^2)_{l_m}$, for these two windows, and for all the models we consider here.

Clearly, the range of multipole moments to which an individual-channel SP94 window is sensitive to is quite model dependent, and this range is not adequately summarized by the W_l parameters l_e and $l_{e-0.5}$. For the model CMB anisotropy spectra we consider here, the SP94 experiment is sensitive to the CMB anisotropy on a somewhat larger angular scale than the effective angular scale determined by the W_l parameter l_e . For the SP94 experiment, and the models we consider here, the $(\delta T_{\text{rms}}^2)_l$ parameters, l_m and $l_{e-0.5}$, do provide an adequate, model-dependent, characterization of the range of l to which the SP94 experiment is sensitive to. This is not true in general, and only works here because the models we consider here have C_l s that are fairly smooth in the relevant range of l -space.

In what follows, we shall have need for the bandtemperature (e.g., Bond 1996),

$$\delta T_l = \frac{\delta T_{\text{rms}}}{\sqrt{I(W_l)}}, \quad (7)$$

where $I(W_l)$ is defined in eq. (4) (note that δT_l does not depend explicitly on l). Compared to δT_{rms} , δT_l has the advantage of being insensitive to the normalization of W_l . As we shall see below, it is still fairly sensitive to the precise shape of W_l .

The reduced SP94 sky temperature anisotropy data used in the analysis of G95 is shown in Fig. 4. In Table 3, line labelled “Sky”, we give the rms of the estimated sky temperature anisotropy, estimated from the data of Fig. 4 as the square root of the difference between the variance of the mean temperatures and the variance of the error bars. As this ignores off-diagonal noise and spatial correlations, as well as the oversampling of points on the sky¹⁴ (which are all accounted for in the likelihood analysis), it could deviate from the true sky anisotropy signal rms by as much as 10 – 20%.

For the purpose of the following discussion we assume that the SP94 sky signal is purely CMB spatial anisotropy without any offset or gradient, which would have been removed while removing instrumental drift. Following Bond et al. (1991), the “bare” likelihood function (e.g., at given beamwidth and nominal calibration) corresponding to a given model C_l spectrum, is calculated according to

$$L(C_l) \propto \frac{1}{\sqrt{\det(\mathbf{f}^T \mathbf{M}^{-1} \mathbf{f}) \det(\mathbf{M})}} e^{-\chi^2/2}, \quad (8)$$

where,

$$\chi^2 = \mathbf{\Delta}^T (\mathbf{M}^{-1} - \mathbf{M}^{-1} \mathbf{f} (\mathbf{f}^T \mathbf{M}^{-1} \mathbf{f})^{-1} \mathbf{f}^T \mathbf{M}^{-1T}) \mathbf{\Delta}. \quad (9)$$

Here $\mathbf{\Delta}$ is the vector of temperature deviations (with $N = 43 \times 7$ elements for the full data set, for example), $\mathbf{M} = \mathbf{C} + \mathbf{\Sigma}$ is the correlation matrix of the data in the context of the model considered (the sum of correlations arising from the specific model considered, $\mathbf{C}(C_l)$, eq. [2] of G95, and instrumental and atmospheric noise, $\mathbf{\Sigma}$). The unwieldy term in the expression for χ^2 arises from marginalizing over all possible values of offset and gradient (assuming a uniform prior in the amplitude of the drifts). \mathbf{f} is the array of functions that have been fit out of the data (in this case an offset and gradient from each channel; it is thus an $N \times 14$ matrix for the full data set). Here, because the bin weights for each channel are fairly uniform, the difference between using unweighted fitting functions and weighted ones, as recommended by Bunn et al. (1994), is small. (This is not the case, however, for

¹⁴ The SP94 FWHM beamwidths are significantly larger than the data-bin-separation on the sky.

other experiments, such as FIRS, which do not uniformly sample the area covered.) As discussed above, we parametrize the model C_l using $Q_{\text{rms-PS}}$ and the shape parameters Ω_0 , h , and Ω_B .

With this prescription, for a given data set all models yield the same likelihood at $Q_{\text{rms-PS}} = 0 \mu\text{K}$ (no sky signal), providing a convenient way to normalize across models.

In Table 3, the lines labelled ‘‘FBP’’, are central δT_{rms} values derived from the results of individual-channel likelihood analyses using the flat bandpower (FBP) angular spectrum (eq. [3]), at the -1σ , nominal, and $+1\sigma$ values of the beamwidth.

To derive the $Q_{\text{rms-PS}}$ central value and limits from the likelihood function for a given C_l and data set, we adopt and advocate the following prescription (Berger 1985, p. 140; Myers, Readhead, & Lawrence 1993, §3.1; Górski et al. 1996).

Bayes’s theorem states that the posterior probability density distribution is proportional to the likelihood function multiplied by the prior probability. Lacking good information to the contrary, here we assume a uniform prior in $Q_{\text{rms-PS}}(\geq 0)$, resulting in a posterior probability density distribution equal to the likelihood function. For SP94, the likelihood functions for the combined Ka, Q, and (full) Ka + Q data subsets are nicely peaked, and well separated from zero sky signal, so we expect only a weak dependence of the deduced sky signal amplitudes on the choice of the prior probability (for reasonable priors).

The central value is taken to be the value of $Q_{\text{rms-PS}}$ at which the probability density distribution peaks (i.e., it is the mode of the posterior distribution). We then integrate the probability density over $Q_{\text{rms-PS}}$, starting from the most likely value of $Q_{\text{rms-PS}}$ and slicing at equal probability density values (this is the highest posterior density prescription, hereafter HPD) until we get to $\sim 95.45\%$ of the total area under the probability density distribution. If the lower value of $Q_{\text{rms-PS}}$ which bounds this area is greater than $0 \mu\text{K}$, we say that there is a 2σ detection; we then determine the two values of $Q_{\text{rms-PS}}$ which enclose $\sim 68.27\%$ of the area under the probability density function, and refer to these as the $\pm 1\sigma$ HPD limits on $Q_{\text{rms-PS}}$. If instead, the $\sim 95.45\%$ HPD lower limit on $Q_{\text{rms-PS}}$ is $0 \mu\text{K}$ (or does not exist), we say that there is no detection; we then integrate the probability density function over $Q_{\text{rms-PS}}$, starting from $0 \mu\text{K}$ until we get to the value of $Q_{\text{rms-PS}}$ that includes $\sim 97.72\%$ [= $1 - 0.5(1 - 0.9545)$] of the total area under the probability density function (this is the equal tail prescription, hereafter ET), and call this value of

$Q_{\text{rms-PS}}$ the 2σ ET upper limit. Of course, the choice of how to define limits depends on what one wishes to use the data for, and will hopefully not be a significant issue when the data improves. The definition we choose to adopt yields smaller lower limits for detections (and so is conservative when used to establish the significance of a detection of anisotropy), and it yields larger upper limits for nondetections. It also leads to the tightest constraint on $Q_{\text{rms-PS}}$, and therefore provides for greater discrimination between models. (This, in fact, is the reason that the HPD prescription is advocated for use with the likelihood method, which is meant to be used to determine as tight a constraint as possible on the relevant model parameters from the data.) These HPD limits are fairly commonly used (e.g., Myers et al. 1993; Górski et al. 1996; Griffin et al. 1996), although a number of other prescriptions are also used.

In all cases we computed limits up to $\pm 3\sigma$ ($\sim 99.73\%$ HPD). Studying these $\pm 3\sigma$ limits, we conclude that, for the purpose of constraining models, the data does not warrant treatment at this level of significance. We emphasize, however, that even accounting for calibration and beamwidth uncertainties, the Ka, Q, and Ka + Q data subsets show evidence for at least 3σ detections.

G95 quote $\pm 1\sigma$ ET (16.0% and 84.0%) limits for the Ka, Q, and Ka + Q anisotropy detection data. Their prescription differs from what we have adopted here. In Table 4 we give the G95 central values and $\pm 1\sigma$ ET limits, and our central values and $\pm 1\sigma$ limits, computed using both the G95 ET prescription and the HPD ($\sim 68.27\%$) prescription. These are given for bandtemperature (eq. [7]), for the combined Ka, Q, and Ka + Q data, extracted using the flat bandpower angular spectrum (eq. [3]) in likelihood analyses, for the nominal beamwidth windows, and ignoring calibration uncertainty. The last two lines of Table 4 give the average of the $\pm 1\sigma$ error bars, in μK and as a percentage of the central value.

Motivated by the steadily improving CMB spatial anisotropy data, we take this opportunity to develop general techniques to account for various sources of uncertainty, both experimental and observational, in the likelihood analysis. As discussed above (eqs. [8] & [9]), we derive “bare” likelihood functions for each model and channel(s), at a given value of the beamwidth(s), $L(Q_{\text{rms-PS}}, \sigma_{BW}^{(A)})$, where $\sigma_{BW}^{(A)}$ is the frequency-independent factor in the A^{th} channel (or channels) beamwidth (as discussed in §1, it is related to the gaussian beamwidth, e.g., for the Ka-channels: $\sigma_G^{(\text{Ka})} = \sigma_{BW}^{(\text{Ka})} \times [27.7 \text{ GHz}/\nu]$). We now

want to account for the additional uncertainties induced by the radiometer-calibration and beamwidth uncertainties. The methods we develop to do this are quite general, and can be extended to account for other sources of uncertainty (like that in the chop amplitude, which is exceedingly small for SP94, and so is ignored here).

If the detector calibration C is not unity, then the real value of the quadrupole-moment amplitude $Q_{\text{rms-PS},C}$ is related to the “bare” value $Q_{\text{rms-PS}}$ through¹⁵

$$Q_{\text{rms-PS},C} = \frac{Q_{\text{rms-PS}}}{C}, \quad (10)$$

where C can be anywhere between 0 and ∞ . If the detector-calibration distribution function, $P(C)$, is known, then the detector-calibration-uncertainty-corrected likelihood is

$$L_C(Q_{\text{rms-PS},C}) = \int_0^\infty dC P(C) L(Q_{\text{rms-PS}}), \quad (11)$$

where we have dropped the $\sigma_{BW}^{(A)}$ argument for now.

While $P(C)$ can be measured, this has not yet been done for SP94 and so here we assume a functional form for $P(C)$. For obvious reasons, we take the detector-calibration distribution to be gaussian,

$$P(C) = \frac{1}{\sqrt{2\pi} \sigma_C} e^{-(C-1)^2/(2\sigma_C^2)}, \quad (12)$$

where σ_C is the width of the detector-calibration distribution: 0.1 for SP94 (G95, note that this is the absolute-detector-calibration distribution width). Eq. (11) then becomes

$$L_C(Q_{\text{rms-PS},C}) = \frac{1}{\sqrt{2\pi} \sigma_C Q_{\text{rms-PS},C}} \times \int_0^\infty dQ_{\text{rms-PS}} e^{-(Q_{\text{rms-PS}} - Q_{\text{rms-PS},C})^2/[2(\sigma_C Q_{\text{rms-PS},C})^2]} L(Q_{\text{rms-PS}}). \quad (13)$$

In passing we note that the factor of $Q_{\text{rms-PS},C}$ in the denominator of the prefactor on the right-hand side of this equation makes the likelihood marginalized over $Q_{\text{rms-PS},C}$ logarithmically divergent at large $Q_{\text{rms-PS},C}$. Since this occurs at extremely large values of $Q_{\text{rms-PS},C}$, this is not an issue that need bother us here, and is most likely due to the invalidity of our assumption (in eq. [12]), that there is a nonzero probability for $C = 0$.

¹⁵ We will eventually drop the subscript C on $Q_{\text{rms-PS},C}$. The meaning of $Q_{\text{rms-PS}}$ should then be clear from the context.

Some intuition about the expression of eq. (13) may be gotten by studying how it transforms simple analytical “bare” likelihoods. If there is no noise and sample variance, and the “bare” likelihood indicates a perfect, Dirac delta, detection at Q_0 ,

$$L(Q_{\text{rms-PS}}) = \delta(Q_{\text{rms-PS}} - Q_0), \quad (14)$$

then from eq. (13),

$$L_C(Q_{\text{rms-PS},C}) = \frac{1}{\sqrt{2\pi} \sigma_C Q_{\text{rms-PS},C}} e^{-(Q_{\text{rms-PS},C} - Q_0)^2 / [2(\sigma_C Q_{\text{rms-PS},C})^2]}, \quad (15)$$

i.e., the detector-calibration uncertainty skews, and broadens the “bare” likelihood, and $L_C(Q_{\text{rms-PS},C})$ has an amplitude ($Q_{\text{rms-PS},C}$) dependent width. If on the other hand, one has a good “bare” detection at Q_0 , with little noise and sample variance (small σ_0), and we assume a gaussian form for the “bare” likelihood,

$$L(Q_{\text{rms-PS}}) = \frac{1}{\sqrt{2\pi} \sigma_0} e^{-(Q_{\text{rms-PS}} - Q_0)^2 / (2\sigma_0^2)}, \quad (16)$$

then in the limit when $\sigma_0 \ll Q_0$ (and assuming that $\sigma_0 \not\gg \sigma_C Q_{\text{rms-PS},C}$ and that $\sigma_C Q_{\text{rms-PS},C} \not\gg Q_0$) it may be shown that eq. (13) results in

$$L_C(Q_{\text{rms-PS},C}) = \frac{1}{\sqrt{2\pi\{(\sigma_C Q_{\text{rms-PS},C})^2 + \sigma_0^2\}}} e^{-(Q_{\text{rms-PS},C} - Q_0)^2 / [2\{(\sigma_C Q_{\text{rms-PS},C})^2 + \sigma_0^2\}]}, \quad (17)$$

i.e., the detector-calibration uncertainty again skews and broadens the “bare” likelihood, and the detector-calibration-uncertainty-corrected likelihood has an amplitude-dependent width. This is what is intuitively expected, and differs a little from the usual naive prescription for accounting for the fractional calibration uncertainty by adding it in quadrature to the error bars derived from the “bare” likelihood (e.g., RBGS; RS).

Although the detector-calibration distribution is not yet known for any experiment, the gaussian assumption (eq. [12]) is probably quite reasonable, and we use this in what follows. It is, however, important to bear in mind that this is an assumption, which can, and should, be checked by direct measurements.

Ideally, one would like to “marginalize” over the beamwidth uncertainty (i.e., treat it as an additional, purely statistical, uncertainty in the likelihood analysis). As discussed above, we assume that the beamwidth uncertainties for all channels shift together. (This

is justified for the individual Ka channels and for the individual Q channels, however, since the Ka-band and Q-band measurements were performed consecutively, using different horns and the same telescope, the Ka and Q beamwidth uncertainties do not necessarily shift together.) For the frequency-independent factors in their beamwidths, G95 measure

$$\begin{aligned}\sigma_{BW,\text{nom}}^{(\text{Ka})} \pm \delta\sigma_{BW}^{(\text{Ka})} &= (0.70 \pm 0.04)^\circ, \\ \sigma_{BW,\text{nom}}^{(\text{Q})} \pm \delta\sigma_{BW}^{(\text{Q})} &= (0.47 \pm 0.04)^\circ.\end{aligned}\tag{18}$$

If the beamwidth distribution function for the Ath channel(s) is $P(\sigma_{BW}^{(A)})$, the beamwidth-uncertainty-“marginalized” and calibration-uncertainty-corrected likelihood is

$$L_{BW,C}^{(A)}(Q_{\text{rms-PS},C}) = \int_0^\infty d\sigma_{BW}^{(A)} P(\sigma_{BW}^{(A)}) L_C(Q_{\text{rms-PS},C}, \sigma_{BW}^{(A)}),\tag{19}$$

where L_C is defined in eq. (13). While $P(\sigma_{BW}^{(A)})$ can actually be measured, this has not yet been done for SP94; instead, one can assume it is a gaussian:

$$P(\sigma_{BW}^{(A)}) = \frac{1}{\sqrt{2\pi} \delta\sigma_{BW}^{(A)}} e^{-(\sigma_{BW}^{(A)} - \sigma_{BW,\text{nom}}^{(A)})^2 / [2(\delta\sigma_{BW}^{(A)})^2]}.\tag{20}$$

This method of accounting for the beamwidth uncertainty is computationally intensive (since a reasonably accurate evaluation of the integral of eq. [19] requires the integrand, and hence the whole likelihood function, at $\gtrsim 50$ different values of the beamwidths in the relevant uncertainty range). It is essential only if one wishes to represent the observational results of an experiment by a single probability density distribution function (e.g., when simultaneously using observational data from two different experiments to constrain models). Since here we are interested in using only the SP94 data to constrain models we choose to adopt a more approximate (and less computationally intensive but still quite accurate) method for accounting for this uncertainty. We account for the beamwidth uncertainty by using the larger upper limit and the smaller lower limit determined from the probability density distribution functions evaluated at the $\pm 1\sigma$ values of the beamwidth (this is for the case of detections, the generalization to the non-detection case is obvious).

Since we have found that the values of the probability density distribution functions marginalized over amplitude $Q_{\text{rms-PS},C}$ are fairly independent of beamwidth, we know that this approximate prescription is not inaccurate for determining them. It is less accurate for determining the limits on the amplitude $Q_{\text{rms-PS},C}$, mostly for the combined Ka + Q data

(since we have analyzed this data set assuming that the Ka- and Q-band beamwidth uncertainties shift together, which they do not necessarily do), and in this case our limits are somewhat overconservative. (A more accurate estimate is possible in this case. However, we do not believe that this is as yet warranted for the purpose of constraining models.) Furthermore, our neglect of the absolute-pointing uncertainty when combining the Ka- and Q-scan data sets (for the Ka + Q analysis) compensates approximately for this effect. [We note that a proper accounting of the absolute-pointing uncertainty would require analyses of the data with the Ka- and Q-scan bins offset on the sky. These need to be performed at various values of the offset, and one then “marginalizes” over the offset (with a gaussian weighting). Again, this is computationally intensive, and we do not believe that it is as yet warranted for the purpose of constraining models.]

In passing, we note that the technique used by G95 to measure their beamwidths, and their results given in eq. (18), simplifies the issue of accounting for the beamwidth uncertainty. If the beamwidths of the different channels are measured at different frequencies, or were found not to factorize into a frequency-dependent term and a frequency-independent term, it would be a slightly more complex matter to properly account for the beamwidth uncertainty.

Finally, we attempt an approximate estimate of the anisotropy spectral index β (Wolack et al. 1993), using both the estimated SP94 “sky” rms, and a theoretical flat bandpower CMB anisotropy angular spectrum (eq. [3]) with the SP94 W_l . For a frequency spectrum $\delta T_{\text{rms}}(\nu) \propto \nu^\beta$, we have

$$\beta = \ln \left[\frac{\delta T_{\text{rms}}(\nu_1)}{\delta T_{\text{rms}}(\nu_2)} \right] \left[\ln \left(\frac{\nu_1}{\nu_2} \right) \right]^{-1}, \quad (21)$$

and for the theoretical flat bandpower angular spectrum this may be rewritten (using eq. [7] and the fact that for a flat bandpower spectrum $\delta T_l = \sqrt{12/5} Q_{\text{rms-PS}}$) as

$$\beta = \ln \left[\sqrt{\frac{I(W_l[\nu_1])}{I(W_l[\nu_2])}} \right] \left[\ln \left(\frac{\nu_1}{\nu_2} \right) \right]^{-1}, \quad (22)$$

where $I(W_l)$ is defined in eq. (4). (Such a computation makes sense for SP94 because the bandpass filters are fairly well modelled as narrow tophats.) The central values of β are given in Table 5 for the nominal beamwidth SP94 windows (these computations use the numerical values of cols. [2] & [12] of Table 1, and those in the row labelled “Sky” of Table

3). The β values estimated using eq. (21) do not account for off-diagonal noise and spatial correlations, nor for the oversampling of points.

In Table 6 we give bandtemperature central values and both ET and HPD $\pm 1\sigma$ limits, derived from flat bandpower likelihood analyses of the individual-channel SP94 data sets. These are for the nominal beamwidth W_l , and ignore calibration uncertainty. The last two lines of Table 6 give the average of the $\pm 1\sigma$ error bars, in μK and as a percentage of the central values.

In Table 7 we give the corresponding numbers derived from flat bandpower likelihood analyses of the combined Ka, Q, and (full) Ka + Q data subsets, now accounting for calibration and beamwidth uncertainties using two prescriptions: (1) that suggested by one of us (JOG) to account for these uncertainties by adding 15% of the central value in quadrature to the G95 ET error bars (by default, this has become the “standard” prescription used in CMB anisotropy field); and (2) that used here to first correct the likelihood functions for these uncertainties, and then to use these corrected likelihood functions to derive the relevant numbers (in this case the lower 1σ limits are those determined from the analyses using the -1σ beamwidth W_l , and the upper 1σ limits are those determined from the analyses at the $+1\sigma$ value of the beamwidth — since this prescription does actually overweight the results for the $\pm 1\sigma$ beamwidth W_l , the error bars derived here are slightly overconservative, probably at the percentage-point level; we emphasize, however, that some of the known uncertainties we have ignored in our preliminary analysis here will compensate for this effect).

Central values and limits for $Q_{\text{rms-PS}}$, for the models we consider here, for all three values of the beamwidths, and both ignoring and accounting for the calibration uncertainty, are given in Tables 8 – 11, for the Ka + Q, Ka, Ka2, and Q2 data sets. The likelihood functions used in the derivation of these numerical values, for some selected models, are shown in Figs. 5(a) – (h). In Fig. 6 we compare, for each of these data sets and for the selected models, the difference in the calibration-uncertainty corrected likelihood functions, at the nominal beamwidth, due to the differences in the model CMB spatial anisotropy spectra. These data sets were chosen for illustrative purposes only: the Ka2 data does not have a detection, and the Q2 data has one of the best detections.

In Tables 12 – 15 we list the values of the probability density distribution functions at the peak, and the marginalized (over $Q_{\text{rms-PS}}$) probability density distribution values¹⁶,

at all three values of the beamwidths, and both ignoring and accounting for calibration uncertainty, for the Ka + Q, Ka, Ka2, and Q2 data sets. The selected models, shown in the Figures, were chosen on the basis of their marginal probability distribution values, for the Ka + Q data set, at the nominal beamwidth, and accounting for calibration uncertainty. (We emphasize that for all the combined SP94 data sets, and some of the individual-channel ones as well, the likelihood functions are peaked, and well-separated from 0 μK . See Figs. 5 and 6. For instance, for the Ka + Q data set the amplitude of the likelihood function at the peak is approximately 10^{19} times larger than that at 0 μK . For such likelihood functions it makes sense to choose between models on the basis of the value of the marginal probability distribution function.) Model O4 (an $\Omega_0 = 0.2$ open model) is the most likely model, followed, amongst our selected models, by Flat (flat bandpower), models O11 and $\Lambda 2$ (an open $\Omega_0 = 0.5$ model and a spatially-flat $\Omega_0 = 0.2$ model), O14 (fiducial CDM), and, the least likely one, $\Lambda 10$ (a flat- Λ $\Omega_0 = 0.4$ model). These selected models include the most and least likely open and flat- Λ ones (from the calibration-uncertainty-corrected, nominal beamwidth, Ka + Q data set analysis) amongst the models we consider here.

Since both the open and flat- Λ model CMB spatial anisotropy spectra shape depend on 3 “free” parameters (Ω_0 , h , and Ω_B), the 14 open and 12 flat- Λ model spectra we use in the analyses here do not provide enough resolution in model-parameter space for us to be able to construct the complete marginalized (over sky-signal amplitude) probability density distribution function, i.e., the probability density distribution function for just the cosmological parameters. (Approximate estimates, discussed below, indicate that the data does not yet allow for robust discrimination between models, so we have decided to not sample model-parameter-space more densely.)

In Tables 16 – 22 we list central values and limits for both $Q_{\text{rms-PS}}$ and δT_l (computed using eqs. [5] – [7]), for all the models and all individual-channel data sets. These account for both beamwidth and calibration uncertainty, with the lower limits being determined from the calibration-uncertainty-corrected probability density distribution functions at the -1σ beamwidth, and the upper limits from those at the $+1\sigma$ beamwidth. In these Tables we also give the corresponding 1σ two-year DMR $Q_{\text{rms-PS}}$ range for the models, accounting

¹⁶The marginalized probability density distribution function is the probability density distribution function for just the cosmological parameters Ω_0 , h , and Ω_B . In what follows we usually call this the “marginal probability distribution function”.

for both statistical and systematic DMR uncertainties (Stompor et al. 1995, also see RBGS; RS), as well as the SP94 maximum and marginalized values of the probability density distribution functions at the nominal beamwidth (accounting for calibration uncertainty).

The corresponding numbers for the combined Ka, Q, and Ka + Q data sets are given in Tables 23 – 25. Except for the flat bandpower model, it is not possible to compute δT_l for these data sets, since they are combinations of data from different windows (it is possible to make up approximate, effective, windows, but since this introduces additional uncertainty, we neither advocate nor adopt this procedure). The corresponding flat bandpower model δT_l values may be found in Table 7.

Figures 7 show SP94 (combined Ka, Q, and Ka + Q data sets) and DMR normalized CMB anisotropy spectra for the selected models, as well as the corresponding individual-channel SP94 results (determined from individual-channel likelihood analyses).

3. RESULTS AND DISCUSSION

From Table 3 we see that the central values of the rms estimated using a flat bandpower angular spectrum in likelihood analyses of an individual-channel data set agree quite well with the central value of the “sky” rms estimated from the data. For three channels they agree to better than 5% and for six channels they agree to better than 20%. This gives some indication of the importance of the off-diagonal noise and spatial correlations, as well as of the oversampling of points, and provides valuable, semiquantitative, confirmation of the likelihood method results. The Ka4 channel “sky” rms differs by $\sim 40\%$ from those derived from the likelihood analyses. The data for this channel does actually look somewhat different from that for the other channels [see the lowest panel of Fig. 4(a)]. To examine whether this can significantly affect the results deduced from the likelihood analyses, we have reanalyzed the combined Ka and Ka + Q data subsets with the Ka4 channel excluded from the analyses. When the Ka4 channel data is dropped from the Ka analysis, the central $Q_{\text{rms-PS}}$ values rise by $\sim 3 - 6\%$ (depending on model), and the 1σ error range broadens by $\sim 5 - 8\%$ (depending on model). When it is excluded from the Ka + Q analysis, the central values drop a little, and the 1σ error ranges slightly tighten. These changes are not big enough to warrant dropping the Ka4 channel data, and the numbers we quote here are from the analyses that include the Ka4 data.

In Table 4 we compare the central values and $\pm 1\sigma$ limits of the bandtemperature derived from likelihood analyses that use the flat bandpower angular spectrum. The numbers are those derived by G95 (16.0% and 84.0% ET) and derived here (both 16.0% and 84.0% ET as well as $\sim 68.27\%$ HPD), for the Ka, Q, and Ka + Q data sets, for the nominal beamwidths, and ignoring calibration uncertainty. The computations described here use more accurate W_l than used by G95 (they differ by $\sim 0.5 - 2\%$, depending on channel), and scaling from our analyses here at three different beamwidths, we estimate that these W_l differences are probably responsible for most of the difference between the δT_l values computed here and in G95. We conclude that, within the expected numerical uncertainty, we reproduce the G95 results for the bandtemperature amplitudes.

Table 4 also gives the $\sim 68.27\%$ HPD $\pm 1\sigma$ limits. We adopt and advocate this prescription to quote limits for detections, since in this case it results in a more conservative -1σ limit than does the corresponding ET prescription. It also leads to slightly tighter average constraints on the bandtemperature, and so provides for slightly greater discrimination between models. Both these effects are evident in the numbers of Table 4: comparing columns (3) & (4), (6) & (7), and (9) & (10), we see that the HPD prescription results in somewhat smaller upper error bars, and somewhat larger lower error bars, than does the ET prescription.

Unlike the Saskatoon (SK) experiments (Wollack et al. 1993; Netterfield et al. 1995, hereafter N95; Netterfield 1995; Netterfield et al. 1996) where the shape in l of the $W_l(\nu)$ used in the β analysis are ν -independent, the shape in l of the SP94 $W_l(\nu)$ are ν -dependent. As this couples spatial (l) and frequency (ν) information, some care is needed when interpreting the results of a β analysis for SP94. In the lower left-hand triangle of Table 5 we list the values of individual-channel-ratio β s derived from the “sky” rms. To estimate combined-channel β s we ignore the Ka4 channel (since we know that the “sky” rms for this channel is significantly higher than that estimated from the likelihood analyses), and average over all the rest of the appropriate individual-channel-ratio β s. We find $\beta_{\text{Ka}} \approx -0.2$, $\beta_{\text{Q}} \approx 2.2$, and $\beta_{\text{Ka+Q}} \approx 0.9$. These should be compared to those derived in G95 from likelihood analyses using the flat bandpower angular spectrum, for the nominal beamwidths, and ignoring calibration uncertainty: $\beta_{\text{Ka}} = 0.2^{+0.9}_{-1.4}$, $\beta_{\text{Q}} = 1.7^{+1.5}_{-1.6}$, and $\beta_{\text{Ka+Q}} = 0.9^{+0.3}_{-0.6}$. Our approximate estimates of the β central values reproduce the more accurate estimates of G95 to within $\sigma/3$ (where σ are the G95 error bars on the β values). This agreement

gives some indication of the importance of off-diagonal noise and spatial correlations, as well as of the effect of oversampling. (In passing we note that it might be of interest to derive the β values from likelihood analyses that account for beamwidth and calibration uncertainty, and using the HPD limits prescription if the likelihood as a function of β is sufficiently peaked.)

Table 5 (upper right-hand triangle) also gives the individual-channel-ratio β s estimated for a theoretical CMB flat bandpower angular spectrum. Averaging as before (but this time also including the Ka4 channel), we find $\beta_{\text{Ka}} \approx 0.5$, $\beta_{\text{Q}} \approx 0.4$, and $\beta_{\text{Ka+Q}} \approx 0.4$. (A similar analysis may be carried through for all the other model CMB angular spectra we use here, and we find $\beta_{\text{Ka}} \sim 0.5 - 0.8$, $\beta_{\text{Q}} \sim 0.4 - 0.6$, and $\beta_{\text{Ka+Q}} \sim 0.4 - 0.7$, with the steeper slopes corresponding to the spatially-flat Λ CDM models.) I.e., since the SP94 W_l couple l and ν information, one does not expect to find $\beta = 0$ even for a pure CMB spectrum. Our approximate β s (derived for the flat bandpower angular spectrum) agree with the central values found by G95, using flat bandpower likelihood analyses, to $\sim \sigma/3$ (Ka) and to $\sim 0.8\sigma$ (Q and Ka + Q). We therefore conclude that the G95 data could be even more consistent with a CMB spectrum than was indicated by them. Although, since the SP94 W_l couple l - and ν -space, the only way to see how inconsistent the G95 β values are with non-CMB foreground contamination is to use a model for both the spatial (l) and frequency (ν) dependence of the assumed non-CMB foreground. While not statistically significant at even the 1σ level (especially since the beamwidth and calibration uncertainties are expected to broaden the G95 β range, although it is not clear what the HPD prescription would do to the range), it might be interesting that our approximate estimate of the central value of β_{Ka} (using a theoretical CMB flat bandpower angular spectrum) reproduces the more accurate G95 flat bandpower likelihood analysis central value to within the accuracy expected for our estimate, and that for all CMB spectra we consider $\beta_{\text{Q}} < \beta_{\text{Ka}}$. It might be of some interest to repeat the G95 β analysis, using model CMB angular spectra (instead of flat bandpower).

It is interesting that, as shown in the second last line of Table 4, the deduced Ka + Q data absolute error bars are larger than those for the Ka data and only slightly smaller than the deduced Q data error bars. Provided that there is no significant non-CMB contamination in one of the bands (which would make the likelihood method, based on an assumed CMB anisotropy spectrum, produce such a behaviour for the error bars), and that the

absolute-pointing uncertainty can be ignored, these error bars only account for statistical (instrumental and atmospheric) noise (which must integrate down) and sample variance uncertainty due to the limited sky coverage, and limited number of independent pixels, of the SP94 data (sample variance can not integrate down without more, independent, sky coverage).

To investigate the behaviour of the error bars, we list, in Table 6, the corresponding bandtemperature central values and ET and HPD limits for the individual channel data sets for a flat bandpower CMB angular spectrum. (The Q1 channel data has a detection for flat bandpower, as well as for some of the low-density open model CMB spectra. However, accounting for calibration and beamwidth uncertainties, the flat bandpower model -2σ HPD δT_l limit is $\sim 1\mu\text{K}$, so it is not a robust detection. The Ka2 channel does not have a detection, independent of the assumed CMB anisotropy spectrum.)

We may approximately model the total absolute average error bars for the combined Ka and Q data sets of Table 4, and for the individual channel data sets of Table 6, using

$$\begin{aligned}\sigma_{\text{tot.,com.}} &= \sqrt{\sigma_{\text{SV}}^2 + \sigma_{\text{N}}^2/N_I}, \\ \sigma_{\text{tot.,ind.}} &= \sqrt{\sigma_{\text{SV}}^2 + \sigma_{\text{N}}^2},\end{aligned}\tag{23}$$

where σ_{SV} is the uncertainty due to sample variance, σ_{N} that due to intrinsic noise, and N_I is the number of channels that contribute to the corresponding combined data set. We emphasize that the model of eq. (23) is approximate (it neglects correlations between channels).

To determine $\sigma_{\text{tot.,ind.}}^{\text{A}}$ (A is either Ka or Q) we use $\sigma_{\text{tot.,ind.}}^{\text{A}} = [\sum_{i=1}^{N_I} (\sigma^{\text{Ai}})^2 / N_I]^{1/2}$ where σ^{Ai} are the individual-channel HPD δT_l average error bars of Table 6. With robust detections only, $\sigma_{\text{tot.,ind.}}^{\text{Ka}} = 13 \mu\text{K}$ ($N_I = 3$) and $\sigma_{\text{tot.,ind.}}^{\text{Q}} = 11 \mu\text{K}$ ($N_I = 2$). With all channels, $\sigma_{\text{tot.,ind.}}^{\text{Ka}} = 12 \mu\text{K}$ ($N_I = 4$) and $\sigma_{\text{tot.,ind.}}^{\text{Q}} = 11 \mu\text{K}$ ($N_I = 3$). Using these numbers and the average HPD δT_l error bars of Table 4, to explain the behaviour of the Ka and Q data error bars, the sample variance and intrinsic noise contributions to the δT_l error bars need to be

$$\begin{aligned}\sigma_{\text{SV}}^{\text{Ka}} &= 6.9(7.7) \mu\text{K}, & \sigma_{\text{N}}^{\text{Ka}} &= 11(9.2) \mu\text{K}, \\ \sigma_{\text{SV}}^{\text{Q}} &= 9.9(9.5) \mu\text{K}, & \sigma_{\text{N}}^{\text{Q}} &= 4.7(5.6) \mu\text{K}.\end{aligned}\tag{24}$$

Here the term in parentheses on the right hand side of each equation is that determined using all channels, and the first terms are those determined using just the robust detection channels. This approximate estimate suggests that the Q data total error bars are dominated by sample variance, the Ka data total error bars are dominated by intrinsic noise, and that the Q data is intrinsically less noisy than the Ka data. The behaviour of the error bars (in Table 4) when the Ka and Q data are combined to form the Ka + Q data set then does not seem very surprising.

It is possible to fairly accurately analytically estimate the sample variance error bars. (A more accurate estimate would make use of simulations, and would be somewhat model dependent. As we are here mostly interested in constraining models using the SP94 data, we do not pursue this option.) We first illustrate the method using the SK93 overlap part of the SK94 experiment (N95), since N95 have performed the requisite simulations and we can use their result to judge how accurate the analytical estimate is.

Most of the weight of the SK93 overlap data comes from the Ka-band observations (L. Page, private communication 1995), which were performed with a beamwidth $\sigma_{\text{FWHM}}^{(\text{Ka})} = 1.4^\circ$. The beam centre traces out a circle of radius 4.4° centered at the NCP, so the experiment has $N_{\text{pix}} = (2\pi \times 4.4^\circ)/1.4^\circ = 20$ pixels (the data is binned into 24 bins, so the SK93 overlap experiment somewhat oversamples). The sample variance error is $\approx 1/\sqrt{2N_{\text{pix}}} = 16\%$. From the Ka93 entry in Table 1 of N95, $\Delta_{\text{rms}} = 37 \mu\text{K}$, so the approximate estimate of the sample variance error bar is $5.9 \mu\text{K}$, which should be compared to the N95 (last paragraph on p. L71) result of $6.5 \mu\text{K}$ (note that this is the sample variance contribution to the δT_{rms} error bars). The analytical estimate of sample variance needs to be increased by 10% to reproduce the N95 result.

Although there are a number of differences between the SK93 overlap and SP94 experiments, the analytical method to estimate sample variance should not be too inaccurate for SP94. At the central Ka-band and Q-band SP94 frequencies, the beamwidths are $\sigma_{\text{FWHM}}^{(\text{Ka})} = 1.5^\circ$ and $\sigma_{\text{FWHM}}^{(\text{Q})} = 1.1^\circ$, so for a 20° scan $N_{\text{pix}}^{(\text{Ka})} = 13$ and $N_{\text{pix}}^{(\text{Q})} = 18$ (SP94 is more oversampled than the SK93 overlap). (We emphasize that our estimates here ignore the small differences between the SP94 individual-channel beamwidths.) Accounting for the 10% correction, the SP94 Ka sample variance is 22%, and the Q sample variance is

18%. Using the Ka and Q δT_l HPD central values of Table 4, and eqs. (23), we find for the sample variance and intrinsic noise contributions to the SP94 δT_l average error bars,

$$\begin{aligned}\sigma_{\text{SV}}^{\text{Ka}} &= 6.2(6.2) \mu\text{K}, & \sigma_{\text{N}}^{\text{Ka}} &= 11(10) \mu\text{K}, \\ \sigma_{\text{SV}}^{\text{Q}} &= 7.0(7.0) \mu\text{K}, & \sigma_{\text{N}}^{\text{Q}} &= 8.5(8.5) \mu\text{K},\end{aligned}\tag{25}$$

which should be compared to the estimates of eqs. (24) (again, the first term on the right hand side of each equation is that determined using just the robust detection channels, and the terms in parentheses use data from all channels). This approximate estimate of the Ka sample variance and intrinsic noise is close to what is required (eqs. [24]) to explain the behaviour of the Ka data error bars. However, the approximate estimate of the Q sample variance indicates that it is not as important (relative to the Q noise) as what is required (eqs. [24]) to explain the behaviour of the Q data error bars. Given the small sky coverage of SP94 ($\sim 20 \text{ deg}^2$), and that our estimates are approximate, this discrepancy might not be statistically significant. More data, with greater sky coverage, is needed to resolve this issue. However, it is clear that sample variance is a significant contributor to the SP94 error bars.

In Table 7 we give bandtemperature central values and $\pm 1\sigma$ limits, that account for calibration and beamwidth uncertainties in two different ways, for the combined Ka, Q and Ka + Q data subsets. (The corresponding uncorrected numbers are given in Table 4.) As mentioned previously, the approximate way of accounting for beamwidth uncertainty used here overweights the $\pm 1\sigma$ beamwidth results and makes the limits derived here somewhat overconservative (possibly at the percentage-point level). However, the known small sources of uncertainty which we have ignored are likely to compensate for this effect. Furthermore, as also mentioned previously, we have ignored the absolute-pointing uncertainty when combining data from the Ka and Q scans (for the Ka + Q data set analysis), and in this case we have also assumed that the Ka and Q beamwidth uncertainties shift together. These effects should approximately compensate, but we emphasize that the results from the Ka + Q data set analysis are less robust than those from either the Ka or Q data subset analyses.

The approximate prescription suggested by one of us (JOG), and universally used in the CMB anisotropy field to account for these uncertainties, results in total 1σ error bar ranges (cols. [2], [5], & [8] of Table 7), that are not very different from the total 1σ HPD

error bar ranges derived here (cols. [4], [7], & [10] of Table 7). Note however that this is because the upper HPD error bars derived here are somewhat smaller and the lower HPD error bars are somewhat larger than these JOG ET error bars, which were previously used to represent the SP94 combined Ka and Q results (RBGS; RS; GRS). Given our understanding of the numerical uncertainties of the computations here, we believe that these differences are numerically significant. If a similar result holds for a number of other small-scale CMB spatial anisotropy experiment data analysis results, then this would raise the lower values of reduced χ^2 found by GRS and probably also tighten the range in the χ^2 values (computed using a variety of prescriptions) for a given model.

Tables 8 – 11 show the effects of the beamwidth- and calibration-uncertainty corrections on the deduced $Q_{\text{rms-PS}}$ central values and limits for some of the SP94 data subsets. The corresponding likelihood functions for the selected models are shown in Figs. 5 and 6.

The windows at the -1σ beamwidth are sensitive to smaller angular scales than those at the nominal value of the beamwidth. The CMB anisotropy spectra we consider here have more power on smaller angular scales (than on larger angular scales), so observational data analyses at the -1σ value of the beamwidth would push these model spectra down (relative to that at the nominal value of the beamwidth), resulting in a lower value of $Q_{\text{rms-PS}}$ for the model. Similarly, at the $+1\sigma$ value of the beamwidth the SP94 data would prefer higher $Q_{\text{rms-PS}}$ values for the model CMB spectra. This effect is clearly evident in the numbers of Tables 8 – 11.

As discussed in the previous section, the calibration uncertainty correction broadens and skews the probability density distribution functions toward higher values of $Q_{\text{rms-PS}}$, resulting in a small increase in the central $Q_{\text{rms-PS}}$ values, and a larger increase in the 1σ limit range. These effects are also clearly evident in the numbers of Tables 8 – 11.

Tables 12 – 15 show the effects of the beamwidth- and calibration-uncertainty corrections on the maximum and marginalized values of the probability density distribution functions for some of the SP94 data subsets. Note that the Ka2 data set does not have a detection. In Table 15 for the Q2 data set, we see that these corrections do not significantly affect the ordering of models with respect to the marginal probability distribution function value. The corrections also have only a small effect on the ordering of models, for the Ka and Ka + Q data subsets (Tables 12 and 13).

It is interesting that at a given beamwidth and calibration-uncertainty treatment, there is a greater range in marginal probability values for the Ka data (Table 13) than there is for the Ka + Q data (Table 12); this larger range is also evident for the Q data (see Table 24). In all cases, among all the models considered here, low-density $\Omega_0 \sim 0.1-0.2$ open models are favoured by the SP94 data. If we assume that the marginal probability distribution (the probability density distribution for just the cosmological parameters Ω_0 , h , and Ω_B) is gaussian, then relative to a model with a renormalized marginal value of unity, a model 1σ away has a value = 0.61, and one 1.5σ away has a value = 0.32. Clearly, the SP94 data do distinguish between the model CMB anisotropy shapes, but not at a very significant level.

Tables 16 – 22 summarize our SP94 individual-channel data set analyses. Columns (5) and (6) in these Tables list the central values and 1σ ranges of band temperature. For a given data set (and beamwidth- and calibration-uncertainty treatment, not all shown here), the bandtemperature values vary by $\sim 0-13\%$ from model to model, with a typical range of $\sim 5\%$. Given the other uncertainties, an analysis based on the flat bandpower CMB spectrum is still quite useful for deriving preliminary, approximate, constraints on models (at least for the SP94 data, which is in a range of l -space that favours this approximation for the models we consider here), but it is not ideal. Furthermore, a flat bandpower analysis cannot provide information about the relative probability of the model CMB anisotropy shapes. Also, when one examines the bandtemperature equivalents of Tables 10 and 11 (as well as those for the individual-channel data not shown here), one notices that the variation in δT_l (central values and limits) with beamwidth (for a given channel) is approximately 0 – 4 percentage points less than the variation in $Q_{\text{rms-PS}}$ with beamwidth (which, depending on model and data subset, can be $\sim 15\%$ between the -1σ and $+1\sigma$ beamwidths). Hence the variation in δT_l with beamwidth is still quite significant (this is particularly true for the flat bandpower spectrum, where δT_l varies as much as $Q_{\text{rms-PS}}$, and so does not take out any of the effect of W_l varying with beamwidth).

Tables 23 – 25 summarize our SP94 combined Ka, Q, and (full) Ka + Q data subset analyses. Since these results are based on data from a combination of windows, it is not possible to accurately compute the corresponding δT_l central values and limits, except for the flat bandpower model (and these are given in Table 7).

Focussing on just the SP94 $Q_{\text{rms-PS}}$ central values and limits from the combined data sets (cols. [4] & [5] of Tables 23 – 25), one notices that for each model the Q-data $Q_{\text{rms-PS}}$ values are somewhat higher than those for the Ka data, however, this is only at approximately 1σ of either the Ka or Q data error bars, and is not significant. Comparing the corresponding δT_l values for the flat bandpower model (cols. [4], [7], & [10] of Table 7) one again notices this effect, but we emphasize that given the errors this is not significant. Furthermore, the Ka + Q data set values are consistent with those from the Ka and Q data subsets (although the Ka + Q data values are much closer to the Q data values).

The individual-channel δT_l central values and ranges (cols. [5] & [6] of Tables 16 – 22) are approximately model independent, for each data set, and so provide a convenient, approximate, summary of the SP94 observational results. Focussing on a given model, one sees, on comparing cols. (5) and (6) in a given line in Tables 16 – 22, that the SP94 δT_l s seem to mildly drop from $l \sim 40$ to $l \sim 50$ (or, at the very least, stay approximately constant), and then seem to mildly rise from $l \sim 50$ to $l \sim 60$ (or at least stay approximately constant, but at a higher value than for the $40 \lesssim l \lesssim 50$ range). (We emphasize that the precise numerical l values are model dependent, and the quoted numbers correspond approximately to those for model O4. We also note that the higher values at larger l are from the Q data, so it is prudent to bear in mind the earlier discussions about β and sample variance.) This effect may be seen more clearly in Figs. 7 (for the selected models), and is related to the effect mentioned in the previous paragraph; again, this is probably not significant. It is interesting that the mildly falling (or flat) δT_l values at lower l are qualitatively consistent with what is seen in the SK94 and SK95 experiments (Netterfield 1995; Netterfield et al. 1996), and that the “dip” or “break” at $l \sim 50 - 60$ is also qualitatively consistent with what is seen in the SK95 experiment (Netterfield et al. 1996).¹⁷ It would be of interest to determine whether or not the SP94 and SK95 “dips” are quantitatively consistent. We emphasize that here we have assumed that the SP94 data is purely CMB anisotropy. The “dip” however might be a consequence of as yet undiscovered small systematic effects, foreground contamination, statistical noise, neglect of the absolute pointing uncertainty, sample variance, or just a result of the CMB anisotropy not being well-described by the models we have used here. Even if there is a “dip” in the CMB

¹⁷ Note that in Figs. 7 – 9 of Netterfield et al. (1996) the SK data are plotted at l_e of the W_l , and not at l_m of the $(\delta T_{\text{rms}}^2)_l$ as done in Fig. 7 here.

anisotropy, it is not very significant in the SP94 data. More data will be needed to resolve these issues.

The marginal probability distribution values for the combined SP94 data sets (cols. [7] of Tables 23 – 25) are similar, although there is a larger range for the Ka and Q data sets than for the Ka + Q data set. CMB anisotropy shapes that are favoured (high marginal probability value) by the Ka data are also favoured by the Q data (and hence by the Ka + Q data). And those that are not favoured (low marginal probability value) by the Q data are also not favoured by the Ka data (and hence neither by the Ka + Q data).

The Ka + Q data, at the nominal beamwidth, and accounting for calibration uncertainty, favour (col. [7] of Table 25) an open $\Omega_0 = 0.2$ model (model O4), among the models we consider here. We do not have the resolution in model-parameter space to construct the complete marginal probability distribution function (the probability density distribution function for just the cosmological parameters), and so cannot properly judge the significance of the values we have computed at isolated points in model-parameter space. To get some idea of the significance of these values we may assume that the marginal distribution is not far from a gaussian. As mentioned above, for a gaussian marginal distribution, a model 1σ away from the most favoured low-density open model CMB anisotropy shape has a marginal value of 0.61, and a model with marginal value 0.32 is 1.5σ away from the most favoured low-density open model. (If the marginal probability distribution function is narrower than a gaussian the above σ -values are overconservative, and if it is wider than a gaussian they are overoptimistic, i.e., for the purpose of ruling out models.) Under the gaussian assumption, the difference between the most favoured low-density open model and the least favoured model (which is always a flat- Λ one) is $\sim 1.4\sigma$ (for Ka + Q) and $\sim 1.6\sigma$ (for Ka or Q), which are not very significant.

We conclude that the SP94 data are most consistent with the CMB anisotropy shape in low-density open CDM models with $\Omega_0 \sim 0.1 - 0.3$ and 0.4 (with larger h and smaller Ω_B), and with the flat bandpower shape (at least among the models we consider here). Since the fiducial CDM and flat- Λ models have CMB anisotropy shapes that are always more than 1σ away (under the gaussian assumption) from the most favoured low-density open model, the SP94 data do not favour these models, especially, old ($t_0 \gtrsim 15 - 16$ Gyr), large baryon density ($\Omega_B \gtrsim 0.0175h^{-2}$), low-density ($\Omega_0 \sim 0.2 - 0.4$), flat- Λ ones. (These results are mostly consistent with the qualitative ones of RBGS and RS, and the

quantitative ones of GRS.) We emphasize, however, that (under the gaussian marginal assumption) the SP94 data do not rule out any of the models we consider here at the 2σ level, on the basis of their CMB anisotropy shape alone.

Finally, we note that the model normalizations deduced from the two-year DMR data and from the SP94 data sets are mostly consistent (although, as mentioned above, the Ka data prefer a normalization $\sim 1\sigma$ below that favoured by the Q data.). The SP94 Q and Ka + Q data favour a slightly higher normalization for the $\Omega_0 = 0.1$ open model than do the two-year DMR data, and the SP94 Ka and Ka + Q data favour a slightly lower normalization of the older (smaller h), higher Ω_B , low-density flat- Λ models than do the two-year DMR data. These results are consistent with those of GRS. It will be of interest to see if the $\Omega_0 = 0.1$ open model can be significantly ruled out on the basis of CMB anisotropy data alone, when the new four-year DMR normalization for this model becomes available.

4. CONCLUSION

We have developed general methods to account for various sources of experimental and observational uncertainty in the likelihood analysis of observational data from a CMB spatial anisotropy experiment.

We have accounted for beamwidth- and calibration-uncertainty in likelihood analyses of the SP94 observational data, that make use of theoretical CMB spatial anisotropy spectra in a variety of observationally-motivated, open and spatially-flat Λ , CDM cosmogonies.

Absolute-radiometer-calibration and beamwidth uncertainties are the largest known sources of uncertainty for the Ka- and Q-scan data from the SP94 experiment (that were not previously explicitly accounted for). In our analysis we have not explicitly accounted for a number of other known (but very much smaller) uncertainties, including: the ellipticity (and possible mild nongaussianity) of the beams; the relative beamwidth uncertainty of the individual-channel beams; the chop-amplitude uncertainty; the effect of the main beam efficiency; the relative-radiometer-calibration uncertainty of the individual channels; the uncertainty in the measured passband frequencies; and the relative-pointing uncertainty. Collectively, these are likely to contribute to the error bars at the percentage-point level. Given that our approximate accounting of the beamwidth uncertainty overweights the $\pm 1\sigma$ beamwidth results, and leads to (Ka and Q) error bars that are overconservative at

the percentage-point level, our neglect of these additional small sources of uncertainty is justified. In addition, when combining the Ka- and Q-scan data (for the Ka + Q data analysis), we have ignored the absolute-pointing uncertainty. We have also analyzed the Ka + Q data set assuming that the Ka and Q beamwidth uncertainties shift together. These two effects, quite likely, compensate, and our Ka + Q data results are not grossly incorrect; however, the Ka and Q results are more robust. Of course, any additional, as yet undiscovered, source of uncertainty could change the results.

In our analyses of the SP94 data we have assumed that it is purely CMB spatial anisotropy; justification for this assumption may be found in G95 and Gundersen (1995).

The combined Ka, Q, and (full) Ka + Q data subsets show evidence for at least 3σ detections of anisotropy. Six (of seven) individual-channel “sky” rms values agree with the rms values derived from individual-channel flat bandpower analyses to within 20%. Predicted flat bandpower β values agree with those found from flat bandpower likelihood analyses by G95, to within a third (Ka) and 0.8 (Q and Ka + Q) of the G95 error bars. Hence the G95 data could be even more consistent with a CMB ν -spectrum than was indicated by them. However, since the SP94 $W_l(\nu)$ couple l - and ν -space, the only way of establishing (from a β -analysis) how inconsistent the SP94 data is with non-CMB contamination would be to use a model for both the l - and ν -dependence of the suspected non-CMB foreground in likelihood analyses of the data. [Only if a multiple-frequency CMB anisotropy experiment has individual-channel window shapes (in l) that are identical does $\beta \neq 0$ indicate that the data are inconsistent with a CMB ν -spectrum.] The behaviour of the Ka data error bars is consistent with what is expected from our approximate estimate of sample variance; the behaviour of the Q data error bars is not as consistent. For all the model CMB spatial anisotropy spectra we consider here, the Q data prefer a somewhat higher normalization than do the Ka data, but this is at only $\sim 1\sigma$ of either the Ka- or Q-data error bars. To see if the differences between the Ka and Q data (as regards β , sample variance, and normalization estimates) is significant will require more data. Until this is accomplished it would be prudent to not draw conclusions using only the full Ka + Q analysis (i.e., one should also consider the implications of both the Ka and Q analyses).

The HPD bandtemperature estimates of Table 7 provide an approximate summary of the SP94 data, and can be used to approximately constrain other models of CMB spatial anisotropy, although likelihood analyses, like those done here, are needed if one wishes to

utilize all the information in the SP94 data. Furthermore, as discussed above, the deduced bandtemperature values typically vary by $\sim 5\%$ from model to model.

While the marginal probability distribution function values show that the SP94 data are clearly sensitive to spatial structure on the sky, they do not significantly distinguish between models (although they do favour low-density open models over older, high Ω_B , low-density, flat- Λ models), and no model considered here is ruled out at the 2σ level by the SP94 data alone (at least in the gaussian marginal probability distribution approximation). The SP94 model normalizations are mostly consistent with those deduced from the two-year DMR data. These results are mostly compatible with what one concludes from a goodness-of-fit analysis of all presently available CMB anisotropy detection data (GRS).

The major contributors to the SP94 Ka- and Q-scan data analyses error bars are (alphabetically): (1) beamwidth uncertainty; (2) calibration uncertainty; (3) intrinsic noise uncertainty; and, (4) sample variance uncertainty. More sky coverage and less oversampling will reduce the sample variance contribution, and longer integration will reduce the intrinsic noise contribution. Measured beamwidth and calibration distribution functions should help reduce the beamwidth- and calibration-uncertainty contributions (unless it turns out that our gaussian approximation is actually narrower than the real distribution function). It should be possible, in the next few years, to acquire data with error bars significantly smaller than the present ones ($\sim 33 - 36\%$).

If measured distribution functions for the parameters of CMB experiments, at least for those that are known to have relatively large uncertainty, become available, the methods we have developed here will allow for a more robust estimate of the sky signal detected in CMB anisotropy experiments, even for presently available CMB anisotropy data.

We acknowledge helpful discussions with D. Bond, K. Górski, and J. Peebles, and are especially indebted to L. Page. KG acknowledges support from NASA grant NAGW-4623.

REFERENCES

- Banday, A. J., et al. 1996, COBE preprint 96-09
- Banks, T., et al. 1995, Phys. Rev., D52, 3548
- Baugh, C. M. 1995, astro-ph/9512011
- Baum, W. A., et al. 1995, AJ, 110, 2537
- Bennett, C. L., et al. 1996, COBE preprint 96-01
- Berger, J. 1985, Statistical Decision Theory and Bayesian Analysis (New York: Springer-Verlag)
- Bolte, M., & Hogan, C. J. 1995, Nature, 376, 399
- Bond, J. R. 1995, CITA preprint CITA-95-28
- Bond, J. R. 1996, in Cosmology and Large Scale Structure, ed. R. Schaeffer, J. Silk, & J. Zinn-Justin (Dordrecht: Elsevier Science Publishers), in press
- Bond, J. R., Efstathiou, G., Lubin, P. M., & Meinhold, P. R. 1991, Phys. Rev. Lett., 66, 2179
- Bond, J. R., & Jaffe, A. 1996, in preparation
- Bucher, M., Goldhaber, A. S., & Turok, N. 1995, Phys. Rev., D52, 3314
- Bucher, M., & Turok, N. 1995, Phys. Rev., D52, 5538
- Bunn, E. F., & Sugiyama, N. 1995, ApJ, 446, 49
- Bunn, E., White, M., Srednicki, M., & Scott, D. 1994, ApJ, 429, 1
- Chaboyer, B., Kernan, P. J., Krauss, L. M., & Demarque, P. 1995, Case Western preprint CWRU-P11-95
- Cheng, E. S., et al. 1996, ApJ, 456, L71
- Cole, S., Fisher, K. B., & Weinberg, D. H. 1995, MNRAS, 275, 515
- David, L. P., Jones, C., & Forman, W. 1995, ApJ, 445, 578
- de Bernardis, P., et al. 1994, ApJ, 422, L33
- Dekel, A., et al. 1993, ApJ, 412, 1
- Djorgovski, S., et al. 1995, ApJ, 438, L13
- Dodelson, S., & Jubas, J. M. 1993, Phys. Rev. Lett., 70, 2224
- Fischler, W., Ratra, B., & Susskind, L. 1985, Nucl. Phys., B259, 730
- Francis, P. J., et al. 1996, ApJ, 457, 490
- Gaier, T., et al. 1992, ApJ, 398, L1
- Ganga, K., Page, L., Cheng, E., & Meyer, S. 1994, ApJ, 432, L15

Ganga, K., Ratra, B., & Sugiyama, N. 1996, ApJ, 461, L1 (GRS)

Giallongo, E., et al. 1994, ApJ, 425, L1

Glazebrook, K., Peacock, J. A., Miller, L., & Collins, C. A. 1995, MNRAS, 275, 169

Górski, K. M., et al. 1996, COBE preprint 96-03

Górski, K. M., et al. 1994, ApJ, 430, L89

Górski, K. M., Ratra, B., Sugiyama, N., & Banday, A. J. 1995, ApJ, 444, L65

Górski, K. M., Stompor, R., & Juszkiewicz, R. 1993, ApJ, 410, L1

Gott III, J. R. 1982, Nature, 295, 304

Griffin, G. S., et al. 1996, in preparation

Gundersen, J. O. 1995, UCSB PhD Thesis

Gundersen, J., et al. 1994, in CMB Anisotropies Two Years After COBE: Observations, Theory and the Future, ed. L. M. Krauss (Singapore: World Scientific), 44

Gundersen, J. O., et al. 1995, ApJ, 443, L57 (G95)

Gundersen, J. O., et al. 1996, in preparation

Guth, A. 1981, Phys. Rev., D23, 347

Guth, A. H., & Weinberg, E. J. 1983, Nucl. Phys., B212, 321

Hancock, S., et al. 1996, in preparation

Harrison, E. R. 1970, Phys. Rev., D1, 2726

Höflich, P. & Khokhlov, A. 1996, ApJ, 457, 500

Hu, W., Scott, D., Sugiyama, N., & White, M. 1995, Phys. Rev., D52, 5498

Jimenez, R., et al. 1996, MNRAS, in press

Kamionkowski, M., Ratra, B., Spergel, D. N., & Sugiyama, N. 1994, ApJ, 434, L1

Kazanas, D. 1980, ApJ, 241, L59

Keihm, S. J. 1983, JPL Internal Memo, 1983 May 2

Klypin, A., Primack, J., & Holtzman, J. 1995, astro-ph/9510042

Kogut, A., et al. 1996, COBE preprint 96-02

Liddle, A. R., Lyth, D. H., Roberts, D., & Viana, P. T. P. 1996, MNRAS, 278, 644

Lilly, S. J., et al. 1995, ApJ, 455, 108

Loveday, J., Efstathiou, G., Maddox, S. J., & Peterson, B. A. 1995, ApJ, submitted

Lu, L., Sargent, W. L. W., Womble, D. S., & Barlow, T. A. 1996, ApJ, 457, L1

Luppino, G. A., & Gioia, I. M. 1995, ApJ, 445, L77

Lyth, D. H., & Woszczyna, A. 1995, Phys. Rev., D52, 3338

Mather, J. C., et al. 1994, ApJ, 420, 439

Meinhold, P. R., et al. 1993, ApJ, 406, 12

Meinhold, P. R., & Lubin, P. 1991, ApJ, 370, L11

Mellier, Y., Dantel-Fort, M., Fort, B., & Bonnet, M. 1994, A&A, 289, L15

Mould, J., et al. 1995, ApJ, 449, 413

Muciaccia, P. F., Mei, S., de Gasperis, G., & Vittorio, N. 1993, ApJ, 410, L61

Myers, S. T., Readhead, A. C. S., & Lawrence, C. R. 1993, ApJ, 405, 8

Netterfield, C. B. 1995, Princeton University PhD Thesis

Netterfield, C. B., et al. 1996, astro-ph/9601197

Netterfield, C. B., et al. 1995, ApJ, 445, L69 (N95)

Nugent, P., et al. 1995, Phys. Rev. Lett., 75, 394

Ostriker, J. P., & Steinhardt, P. J. 1995, Nature, 377, 600

Pascarelle, S. M., et al. 1996, ApJ, 456, L21

Peacock, J. A., & Dodds, S. J. 1994, MNRAS, 267, 1020

Peebles, P. J. E. 1982, ApJ, 263, L1

Peebles, P. J. E. 1993, Principles of Physical Cosmology (Princeton: Princeton University Press)

Peebles, P. J. E., & Yu, J. T. 1970, ApJ, 162, 815

Piccirillo, L., et al. 1996, in preparation

Pierce, M. J., & Jacoby, G. H. 1995, AJ, 110, 2885

Ratra, B. 1991, Phys. Lett., B260, 21

Ratra, B., Banday, A. J., Górski, K. M., & Sugiyama, N. 1995, Princeton preprint PUPT-1558 (RBGS)

Ratra, B., & Peebles, P. J. E. 1994, ApJ, 432, L5

Ratra, B., & Peebles, P. J. E. 1995, Phys. Rev., D52, 1837

Ratra, B., & Sugiyama, N. 1995, Princeton preprint PUPT-1559 (RS)

Ruhl, J. R., et al. 1995, ApJ, 453, L1

Sato, K. 1981a, Phys. Lett., 99B, 66

Sato, K. 1981b, MNRAS, 195, 467

Schuster, J., et al. 1993, ApJ, 412, L47

Scott, D., Silk, J., & White, M. 1995, Science, 268, 829

Shaya, E. J., Peebles, P. J. E., & Tully, R. B. 1995, ApJ, 454, 15

Smail, I., & Dickinson, M. 1995, *ApJ*, 455, L99
Smoot, G. F., et al. 1992, *ApJ*, 396, L1
Stompor, R., & Górski, K. M. 1994, *ApJ*, 422, L41
Stompor, R., Górski, K. M., & Banday, A. J. 1995, *MNRAS*, 277, 1225
Sugiyama, N. 1995, *ApJS*, 100, 281
Tadros, H., & Efstathiou, G. 1995, *MNRAS*, 276, L45
Tanaka, S. T., et al. 1995, *ApJ*, submitted
Tanvir, N. R., Shanks, T., Ferguson, H. C., & Robinson, D. R. T. 1995, *Nature*, 377, 27
Viana, P. T. P., & Liddle, A. R. 1995, Sussex preprint SUSSEX-AST 95/11-1
Vittorio, N., et al. 1991, *ApJ*, 372, L1
Wampler, E. J., et al. 1996, *A&A*, in press
White, D. A., & Fabian, A. C. 1995, *MNRAS*, 273, 72
Whitmore, B. C., et al. 1995, *ApJ*, 454, L73
Wollack, E. J., et al. 1993, *ApJ*, 419, L49
Wright, E. L., et al. 1992, *ApJ*, 396, L13
Yamamoto, K., & Bunn, E. F. 1995, *ApJ*, submitted
Yamamoto, K., Sasaki, M., & Tanaka, T. 1995, *ApJ*, 455, 412
Zel'dovich, Ya. B. 1972, *MNRAS*, 160, 1P

FIGURE CAPTIONS

Fig. 1.– CMB anisotropy multipole moments $l(l+1)C_l/(2\pi) \times 10^{10}$ (broken lines, scale on left axis) as a function of multipole l , to $l = 300$, for selected models O4, O11, O14, Λ 2, Λ 10, and Flat, normalized to the two-year DMR maps. See Table 25 for model-parameter values. Also shown are two SP94 individual-channel, zero-lag, nominal beamwidth, window functions W_l (solid lines, scale on right axis), sensitive to the largest (Ka1) and smallest (Q3) angular scales. See Table 1 for window function parameter values.

Fig. 2.– Individual-channel, nominal beamwidth, zero-lag SP94 window functions W_l (solid lines), as a function of l , to $l = 300$. Also shown (hatched regions) is the uncertainty in the windows sensitive to the largest (Ka1) and smallest (Q3) angular scales, due to the one standard deviation uncertainty in the beamwidths. See Table 1 for window function parameter values.

Fig. 3.– $(\delta T_{\text{rms}}^2)_l$ (eq. [6]) as a function of l , to $l = 250$, for (upper panel) the larger beamwidth (upper one standard deviation) Ka1 channel window, and for (lower panel) the smaller beamwidth (lower one standard deviation) Q3 channel window, for the selected models shown in Fig. 1, normalized to the two-year DMR data. See Tables 2 and 25 for numerical values. Note that the peak sensitivity of an SP94 individual-channel window function corresponds to a different angular scale in each of the models.

Fig. 4.– SP94 data of G95. (a) Individual-channel Ka data. (b) Individual-channel Q data.

Fig. 5.– Likelihood functions, as a function of $Q_{\text{rms-PS}}$ (to $Q_{\text{rms-PS}} = 60\mu\text{K}$), derived from analyses using: the nominal beamwidth, ignoring (solid lines), and accounting for (dotted lines), calibration uncertainty; the -1σ beamwidth, ignoring (short dashed lines), and accounting for (long dashed lines), calibration uncertainty; and, the $+1\sigma$ beamwidth, ignoring (dot-short dash lines), and accounting for (dot-long dash lines) calibration uncertainty. In (a) & (b) are those for the Ka + Q data, in (c) & (d) those for the Ka data, in (e) & (f) those for the Ka2 data (which does not have a detection), and in (g) & (h) those for the Q2 data (which is one of the best individual-channel detections). The 6 individual panels shown for each of these SP94 data sets correspond to the 6 selected models of Fig. 1. See Table 2 for model-parameter values. In each panel the likelihood functions have been renormalized such that the peak value is unity for the one with the highest peak

value. See Tables 8 – 15 for numerical values derived from the corresponding probability density distribution functions.

Fig. 6.– Likelihood functions, as a function of $Q_{\text{rms-PS}}$ (to $Q_{\text{rms-PS}} = 60\mu\text{K}$), for the 6 selected models (O4, O11, O14, $\Lambda 2$, $\Lambda 10$, and Flat) of Fig. 1 (line styles are identical to those used in Figs. 1 and 3), from the nominal beamwidth analyses, and accounting for calibration uncertainty, for the Ka + Q, Ka, Ka2, and Q2 data sets. See Table 2 for model-parameter values, and Tables 8 – 15 for numerical values derived from the corresponding probability density distribution functions.

Fig. 7.– CMB anisotropy bandtemperature predictions and observational results. Hatched regions are what would be seen by a series of ideal, Kronecker-delta window-function, experiments, for the model normalized to the 1σ (correlated) range from the two-year DMR data (hatched region with smaller vertical extent), and for the model normalized to the 1σ (correlated) range from the SP94 combined Q (upper panel), Ka (central panel), and full Ka + Q (lower panel) data subsets (hatched region with larger vertical extent). These are evaluated using the appropriate model C_l spectrum in eq. (7) for a Kronecker-delta W_l . Both normalizations account for all major known uncertainties. Also shown are the corresponding SP94 individual-channel observational results (determined from likelihood analyses that use the appropriate model CMB spatial anisotropy spectrum). Solid squares correspond to detections, and are placed at the peak of the probability density distribution function from the nominal beamwidth analysis (accounting for calibration uncertainty). The vertical error bars on the points corresponding to detections are $\pm 1\sigma$ HPD error bars. Solid inverted triangles are 2σ ET upper limits from the $+1\sigma$ beamwidth analysis (accounting for calibration uncertainty). Vertical error bars account for all major known uncertainties. From left to right, the observational data points correspond to the Ka1 to Q3 data results, and they are placed at l_m determined from $(\delta T_{\text{rms}}^2)_l$ (eq. [6]) for the appropriate model. The horizontal lines on the SP94 individual-channel observational results represent the l -space width of the corresponding W_l , and terminate at $l_{e-0.5}$ determined from $(\delta T_{\text{rms}}^2)_l$ using the $+1\sigma$ beamwidth W_l for the lower value of $l_{e-0.5}$ and the -1σ beamwidth W_l for the higher value. The 6 sets of 3 panels each [(a) to (f)] correspond to the 6 selected models of Fig. 1. See Table 2 for model-parameter values, Tables 23 – 25 for the SP94 (combined data subsets) model normalizations and the two-year DMR model normalizations, and Tables 16 – 21 for the SP94 individual-channel results.

Figure 1

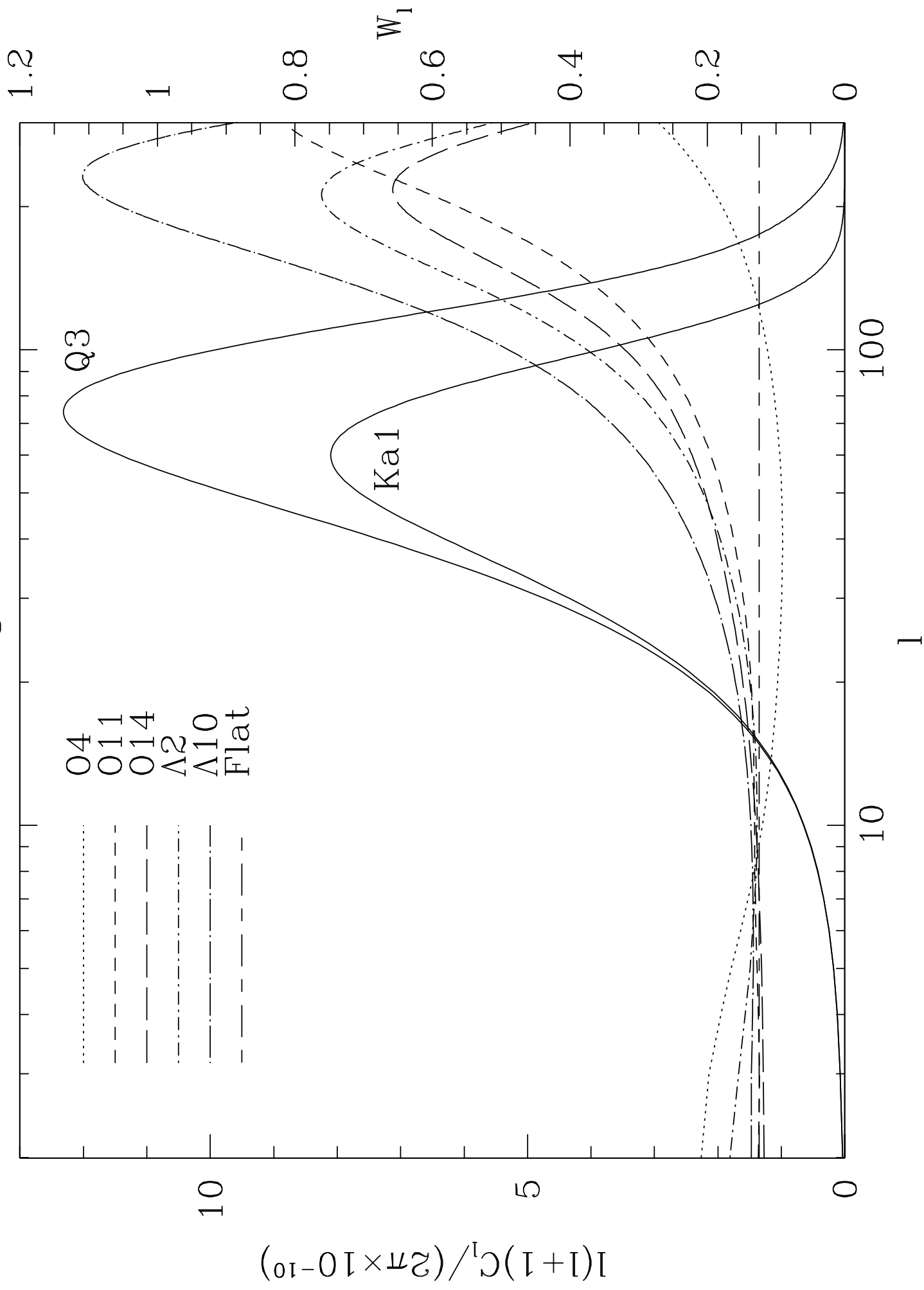


Figure 2

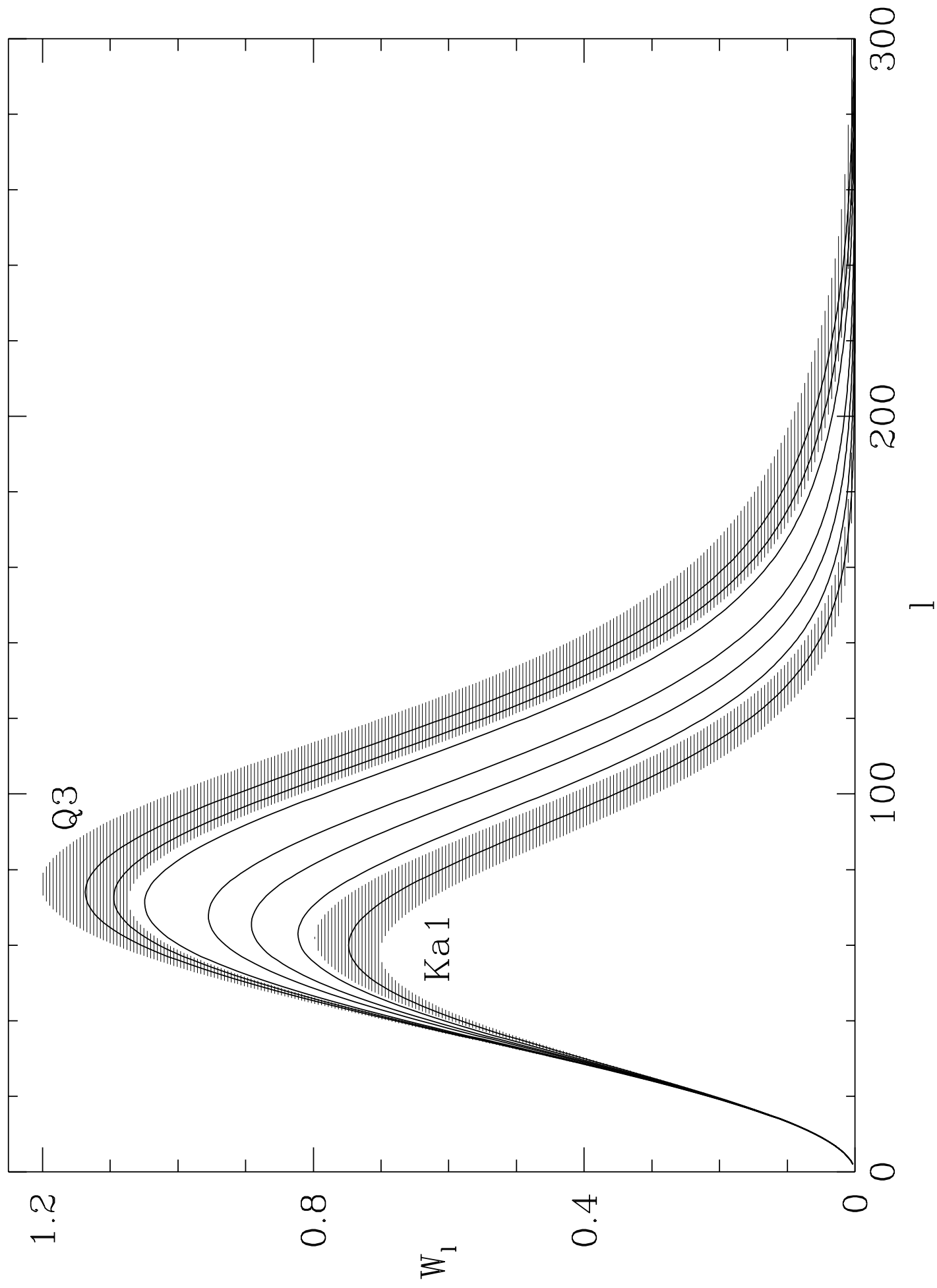


Figure 3

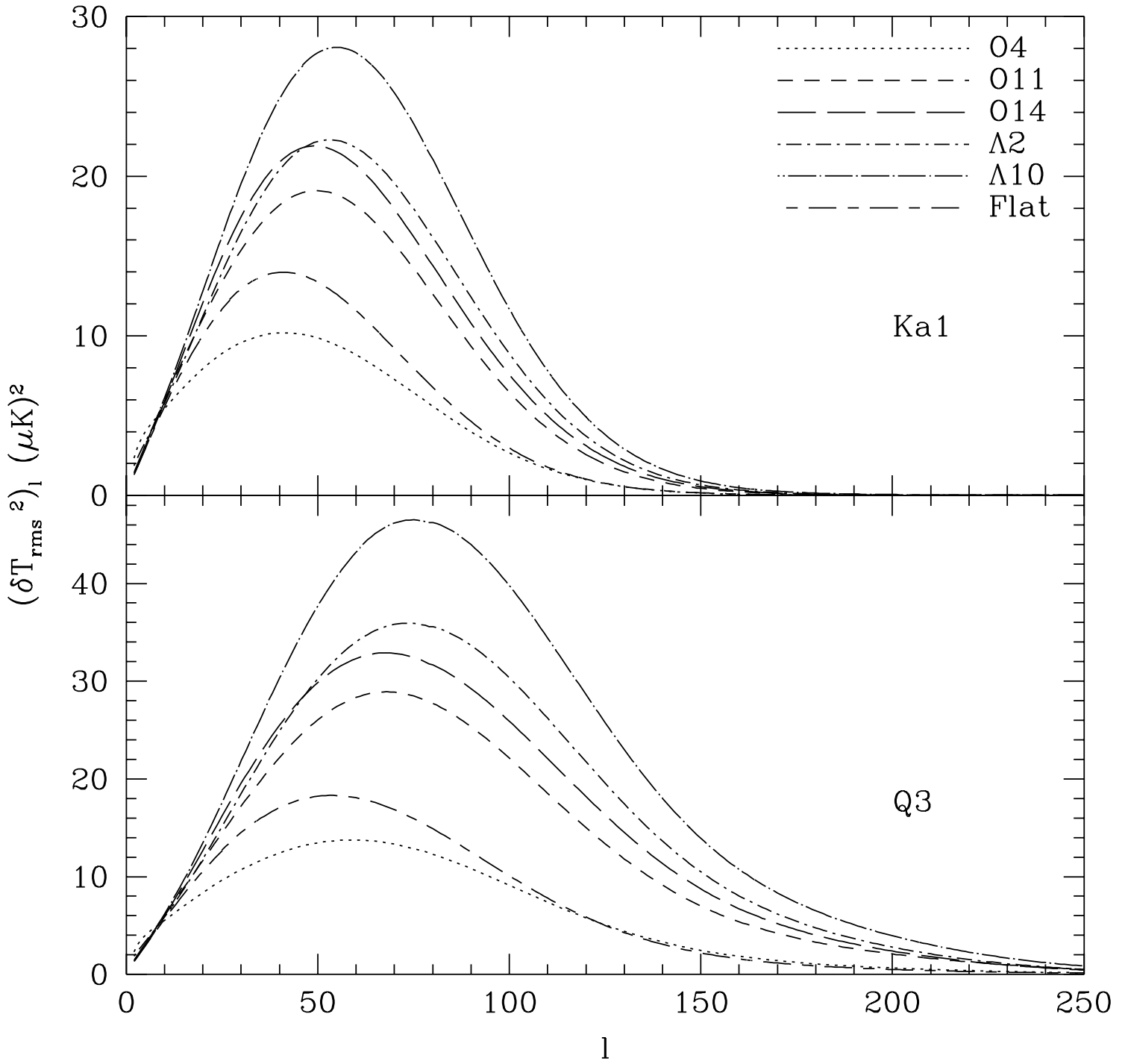


Figure 4(a)

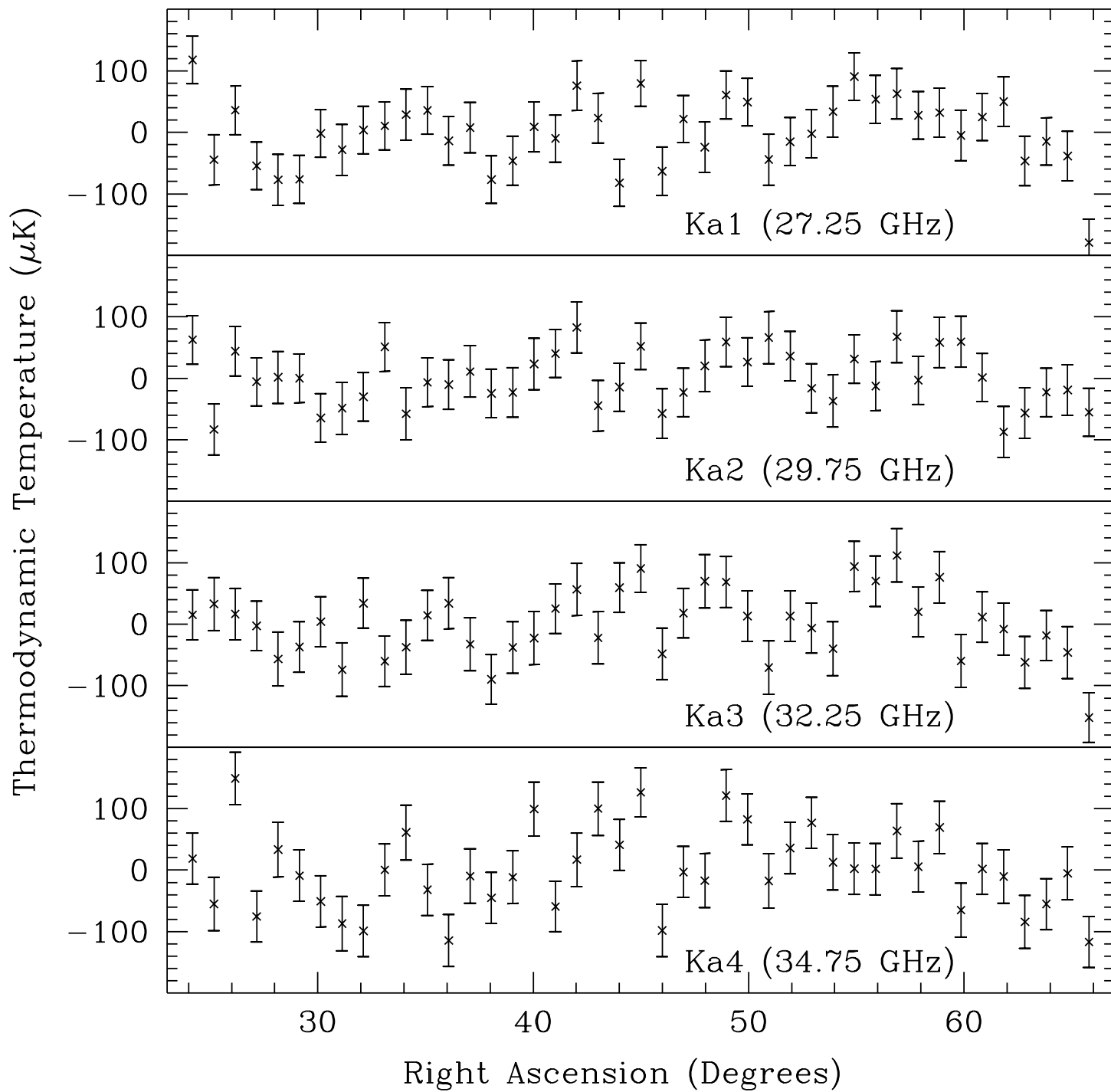


Figure 4(b)

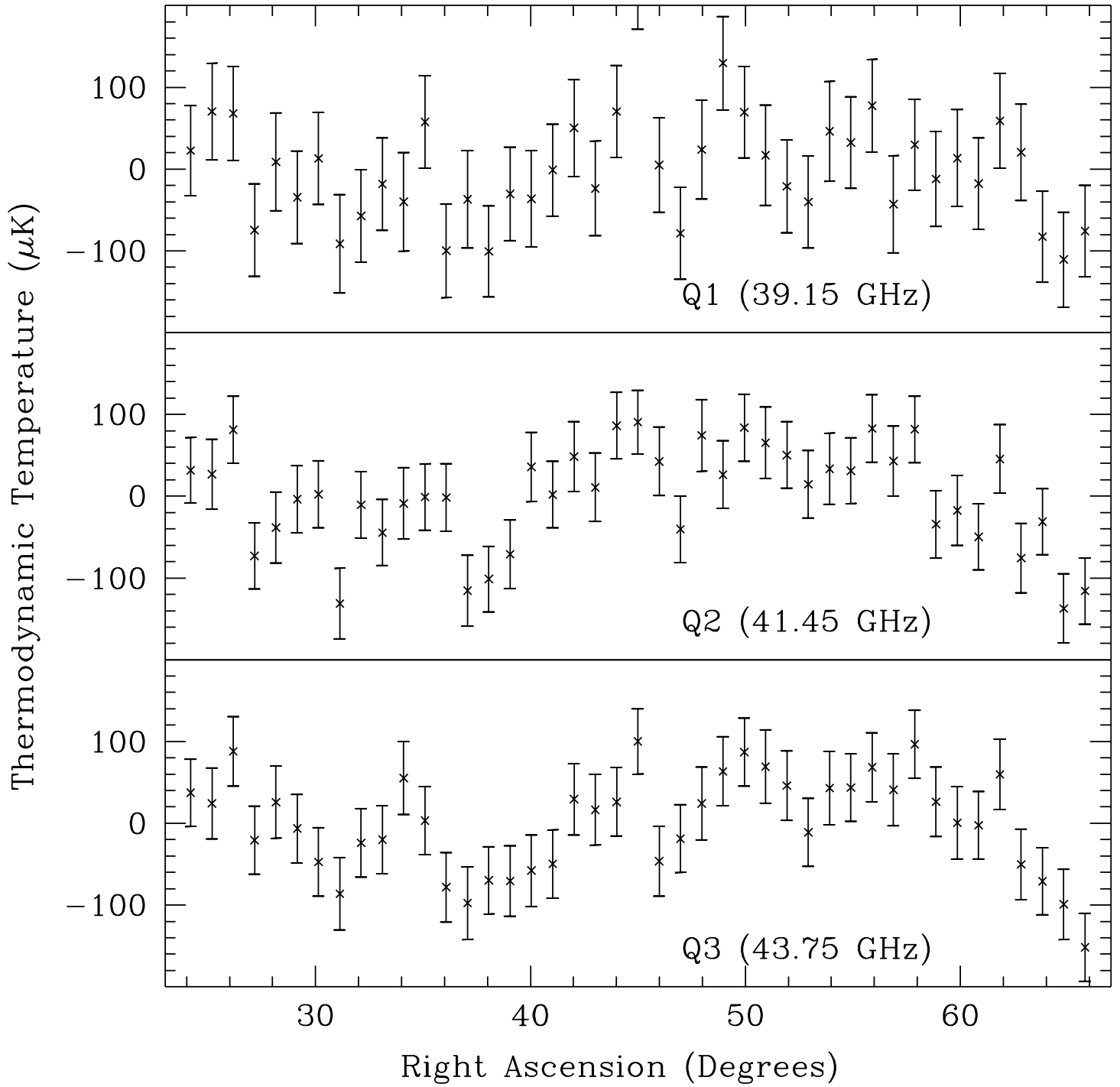


Figure 5(a)

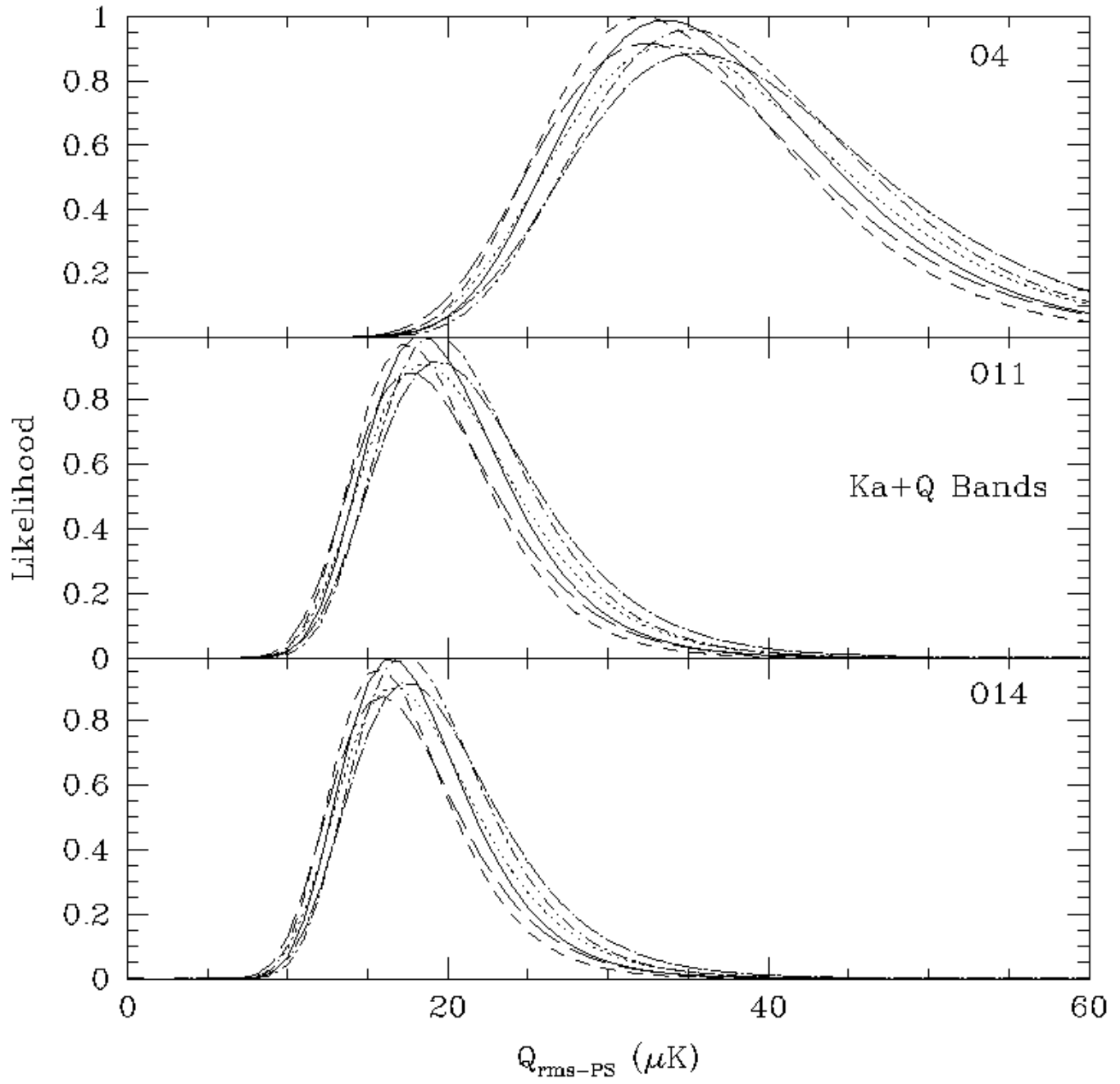


Figure 6

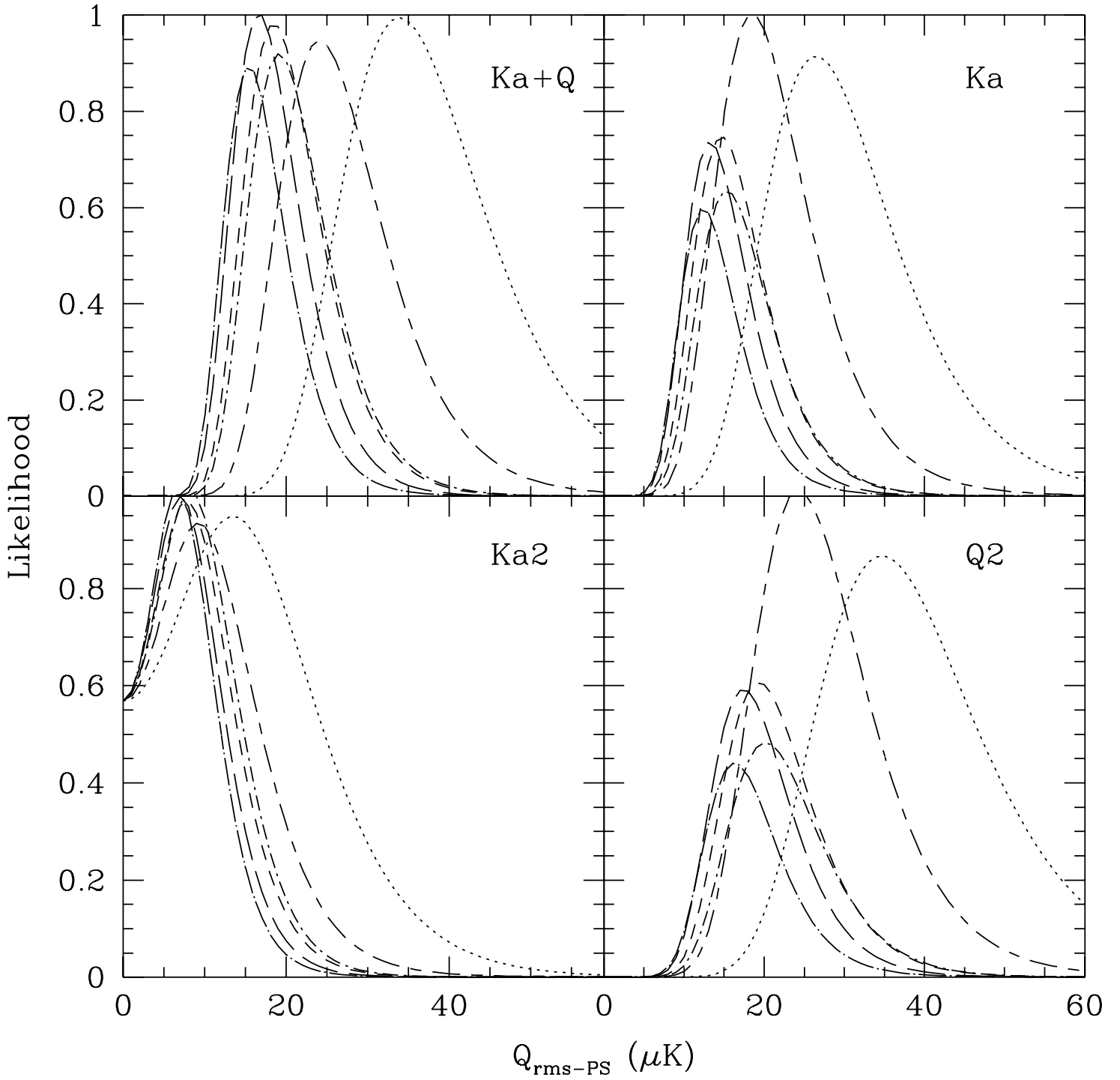


Figure 7(a)

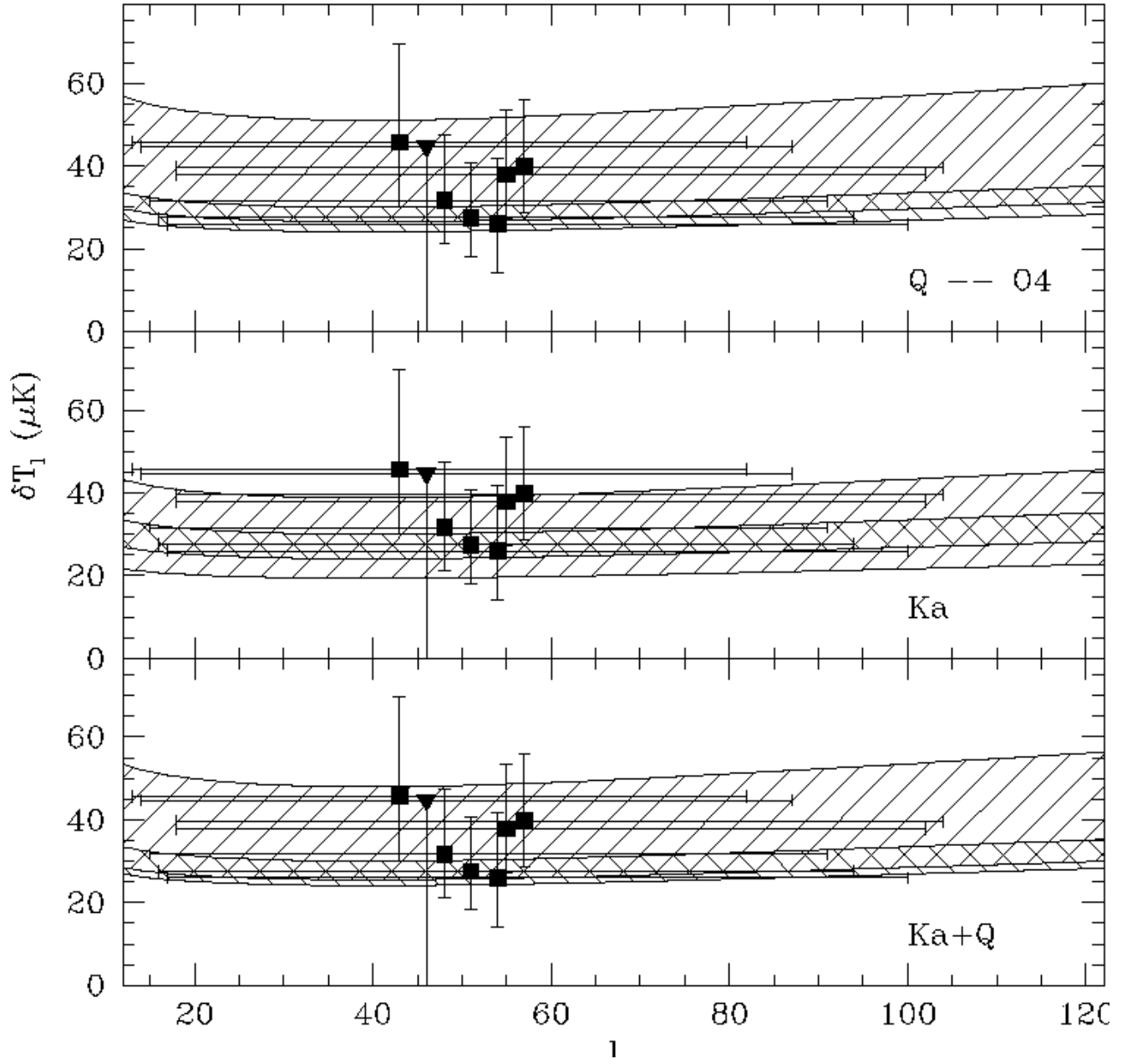


TABLE 1
Numerical Values for the Individual Channel, Zero-Lag, Window Function Parameters

Beamwidth:		-1σ					Nom.					$+1\sigma$				
Ch. #	Freq. (GHz)	$l_{e-0.5}$	l_e	l_m	$l_{e-0.5}$	$\sqrt{I(W_l)}$	$l_{e-0.5}$	l_e	l_m	$l_{e-0.5}$	$\sqrt{I(W_l)}$	$l_{e-0.5}$	l_e	l_m	$l_{e-0.5}$	$\sqrt{I(W_l)}$
(1)	(2)	(3)	(4)	(5)	(6)	(7)	(8)	(9)	(10)	(11)	(12)	(13)	(14)	(15)	(16)	(17)
Ka1	27.25	34	55.2	62	95	1.04	33	53.4	60	92	1.01	32	51.6	58	89	0.977
Ka2	29.75	35	58.0	65	100	1.09	34	56.1	63	97	1.06	33	54.4	61	94	1.03
Ka3	32.25	37	60.5	67	104	1.14	36	58.7	65	101	1.10	35	56.9	64	98	1.07
Ka4	34.75	38	62.8	70	107	1.17	37	61.0	68	105	1.14	36	59.2	66	102	1.11
Q1	39.15	40	67.1	73	114	1.24	39	64.4	71	110	1.20	38	61.9	69	106	1.16
Q2	41.45	41	68.8	75	116	1.27	40	66.1	73	112	1.23	38	63.7	70	109	1.19
Q3	43.75	42	70.4	76	118	1.29	40	67.8	74	115	1.26	39	65.3	72	111	1.22

TABLE 2
Numerical Values for Parameters Characterizing the Shape of $(\delta T_{\text{rms}}^2)_l$

Window:		$+1\sigma$ Ka1			-1σ Q3		
#	$(\Omega_0, h, \Omega_B h^2)$	$l_{e-0.5}$	l_m	$l_{e-0.5}$	$l_{e-0.5}$	l_m	$l_{e-0.5}$
(1)	(2)	(3)	(4)	(5)	(6)	(7)	(8)
O1	(0.1, 0.75, 0.0125)	7	38	74	14	55	102
O2	(0.2, 0.65, 0.0175)	14	43	79	22	63	108
O3	(0.2, 0.70, 0.0125)	13	42	78	21	61	107
O4	(0.2, 0.75, 0.0075)	13	41	77	20	59	104
O5	(0.3, 0.60, 0.0175)	17	47	81	27	66	111
O6	(0.3, 0.65, 0.0125)	16	46	80	25	64	108
O7	(0.3, 0.70, 0.0075)	16	44	78	24	61	106
O8	(0.4, 0.60, 0.0175)	19	48	82	29	67	111
O9	(0.4, 0.65, 0.0125)	18	47	80	27	64	109
O10	(0.4, 0.70, 0.0075)	18	45	79	25	62	106
O11	(0.5, 0.55, 0.0175)	21	50	83	31	68	113
O12	(0.5, 0.60, 0.0125)	20	48	81	29	66	110
O13	(0.5, 0.65, 0.0075)	19	46	79	27	63	107
O14	(1.0, 0.50, 0.0125)	22	49	83	31	68	115
Λ 1	(0.1, 0.90, 0.0125)	28	57	90	40	76	121
Λ 2	(0.2, 0.80, 0.0075)	24	53	87	35	73	120
Λ 3	(0.2, 0.75, 0.0125)	26	55	88	37	75	121
Λ 4	(0.2, 0.70, 0.0175)	27	56	89	39	76	122
Λ 5	(0.3, 0.70, 0.0075)	23	52	86	34	72	119
Λ 6	(0.3, 0.65, 0.0125)	25	54	88	36	74	120
Λ 7	(0.3, 0.60, 0.0175)	27	56	89	38	75	121
Λ 8	(0.4, 0.65, 0.0075)	23	51	85	32	70	118
Λ 9	(0.4, 0.60, 0.0125)	24	53	87	35	73	119
Λ 10	(0.4, 0.55, 0.0175)	26	55	88	37	75	121
Λ 11	(0.5, 0.60, 0.0125)	23	51	86	33	71	118
Λ 12	(1.0, 0.50, 0.0125)	22	49	83	31	68	115
Flat	...	16	41	73	21	54	96
W_l	...	32 ^a	51.6 ^b	89 ^a	42 ^a	70.4 ^b	118 ^a

^a $l_{e-0.5}$ for the window. ^b l_e for the window.

TABLE 3
Numerical Values for Rms Temperature Anisotropies^a

Channel:	Ka1	Ka2	Ka3	Ka4	Q1	Q2	Q3
“Sky” ^b	39	18	36	51	33	47	42
FBP, -1σ W_l ^c	46	15	35	31	31	46	50
FBP, Nom. W_l ^c	46	15	35	31	31	46	50
FBP, $+1\sigma$ W_l ^c	46	15	34	31	31	46	50

^a δT_{rms} in μK . ^bEstimated from the data of Fig. 4, as discussed in §2. ^cConverted to rms (using eq. [7]) from the results of the likelihood analysis for the flat bandpower (FBP) angular spectrum (eq. [3]), at, respectively, the -1σ , nominal, and $+1\sigma$ values of the beamwidth.

TABLE 4
Numerical Values for Bandtemperature^a, Derived from Likelihood Analyses Assuming a Flat Bandpower Angular Spectrum, for the Nominal Beamwidth W_l , and Ignoring Calibration Uncertainty

Data Set: Analysis: (1)	Ka			Q			Ka + Q		
	G95 ^b (2)	Here ^b (3)	Here ^c (4)	G95 ^b (5)	Here ^b (6)	Here ^c (7)	G95 ^b (8)	Here ^b (9)	Here ^c (10)
-1σ Limit	24	23	21	33	33	30	30	31	29
Central Value	29	28	28	40	39	39	36	37	37
$+1\sigma$ Limit	43	42	39	55	55	51	50	52	48
Ave. Abs. Err. ^d :	± 9.5	± 9.5	± 9.0	± 11	± 11	± 10	± 10	± 10	± 9.5
Ave. Fra. Err. ^e :	$\pm 33\%$	$\pm 34\%$	$\pm 32\%$	$\pm 28\%$	$\pm 28\%$	$\pm 27\%$	$\pm 28\%$	$\pm 28\%$	$\pm 26\%$

^a δT_l (eq. [7]) in μK . ^bET (16.0% & 84.0%) prescription. ^cHPD ($\sim 68.27\%$) prescription. ^dAverage absolute error in μK . ^eAverage fractional error, as a fraction of the central value.

TABLE 5
Numerical Values for β , from the “Sky” Rms^a, and from a Theoretical Flat Bandpower CMB Angular Spectrum^b

Channel	Ka1	Ka2	Ka3	Ka4	Q1	Q2	Q3
Ka1	...	0.55	0.53	0.52	0.48	0.47	0.46
Ka2	-8.7	...	0.51	0.50	0.46	0.45	0.44
Ka3	-0.47	8.6	...	0.48	0.44	0.43	0.42
Ka4	1.1	6.7	4.6	...	0.42	0.41	0.40
Q1	-0.49	2.1	-0.51	-3.7	...	0.40	0.39
Q2	0.43	2.9	1.0	-0.48	6.3	...	0.38
Q3	0.15	2.2	0.49	-0.85	2.2	-2.1	...

^aLower left-hand triangle. Estimated from the ratio of the signal in the channel of the first row, to the signal in the channel of the first column (eq. [21]). ^bUpper right-hand triangle. Estimated from the ratio of the signal in the channel of the first column, to the signal in the channel of the first row (eq. [22]).

TABLE 6
 Numerical Values for Bandtemperature^a, Derived from Likelihood Analyses Assuming a Flat Bandpower Angular Spectrum, for the Individual-Channel Data Sets, for the Nominal Beamwidth W_i , and Ignoring Calibration Uncertainty

Data Set:	Ka1	Ka1	Ka2	Ka2	Ka3	Ka3	Ka4	Ka4	Q1	Q1	Q2	Q2	Q3	Q3
Prescript.:	ET	HPD	ET	HPD	ET	HPD	ET	HPD	ET	HPD	ET	HPD	ET	HPD
(1)	(2)	(3)	(4)	(5)	(6)	(7)	(8)	(9)	(10)	(11)	(12)	(13)	(14)	(15)
-1σ Limit	36	31	6.2	3.6	24	22	21	19	17	15	31	28	33	30
Central Value	46	46	14	14	31	31	27	27	26	26	37	37	40	40
$+1\sigma$ Limit	71	65	27	24	49	45	41	39	41	39	53	50	56	52
Ave. Abs. Err. ^b :	± 17	± 17	± 10	± 10	± 12	± 11	± 10	± 10	± 12	± 12	± 11	± 11	± 11	± 11
Ave. Fra. Err. ^c :	$\pm 38\%$	$\pm 37\%$	$\pm 74\%$	$\pm 71\%$	$\pm 40\%$	$\pm 37\%$	$\pm 37\%$	$\pm 37\%$	$\pm 46\%$	$\pm 46\%$	$\pm 30\%$	$\pm 30\%$	$\pm 29\%$	$\pm 28\%$

^a δT_i (eq. [7]) in μK . ET limits are $\sim 15.87\%$ & $\sim 84.13\%$ and HPD limits are $\sim 68.27\%$. ^bAverage absolute error in μK . ^cAverage fractional error, as a fraction of the central value.

TABLE 7
 Numerical Values for Bandtemperature^a, Derived from Likelihood Analyses Assuming a Flat Bandpower Angular Spectrum, and Accounting for Beamwidth and Calibration Uncertainties

Data Set:	Ka			Q			Ka + Q		
Prescript.:	JOG ^b	ET ^c	HPD ^c	JOG ^b	ET ^c	HPD ^c	JOG ^b	ET ^c	HPD ^c
(1)	(2)	(3)	(4)	(5)	(6)	(7)	(8)	(9)	(10)
-1σ Limit	22	23	20	31	32	29	28	30	27
Central Value	29	29	29	40	39	39	36	37	37
$+1\sigma$ Limit	44	45	41	57	59	55	51	56	52
Ave. Abs. Err. ^d :	± 11	± 11	± 10	± 13	± 13	± 13	± 11	± 13	± 12
Ave. Fra. Err. ^e :	$\pm 38\%$	$\pm 38\%$	$\pm 36\%$	$\pm 33\%$	$\pm 35\%$	$\pm 33\%$	$\pm 32\%$	$\pm 35\%$	$\pm 34\%$

^a δT_i (eq. [7]) in μK . ^bJOG prescription to account for calibration and beamwidth uncertainties by adding 15% of the central value in quadrature to the G95 ET (16.0% & 84.0%) prescription error bars. ^cET ($\sim 15.87\%$ & $\sim 84.13\%$) and HPD ($\sim 68.27\%$) limits from the beamwidth- and calibration-uncertainty corrected probability density distribution functions. ^dAverage absolute error in μK . ^eAverage fractional error, as a fraction of the central value.

TABLE 8
Numerical Values for $Q_{\text{rms-PS}}^{\text{a}}$, from Likelihood Analyses Using the Ka + Q Data Set

Beamwidth:	-1σ	-1σ	-1σ	-1σ	Nom.	Nom.	Nom.	Nom.	$+1\sigma$	$+1\sigma$	$+1\sigma$	$+1\sigma$
Cal. Corr. ^b :	No	No	Yes	Yes	No	No	Yes	Yes	No	No	Yes	Yes
# ^c	CV ^d Limits ^e		CV ^d Limits ^e		CV ^d Limits ^e		CV ^d Limits ^e		CV ^d Limits ^e		CV ^d Limits ^e	
(1)	(2)	(3)	(4)	(5)	(6)	(7)	(8)	(9)	(10)	(11)	(12)	(13)
O1	31	25 - 40	32	24 - 42	33	26 - 42	33	25 - 44	34	27 - 45	34	26 - 46
O2	31	24 - 39	31	24 - 41	32	25 - 41	32	25 - 43	33	26 - 43	34	26 - 45
O3	31	25 - 40	32	24 - 42	33	26 - 42	33	25 - 44	34	27 - 44	35	26 - 46
O4	32	25 - 41	32	25 - 43	34	26 - 43	34	26 - 45	35	27 - 46	35	27 - 47
O5	26	21 - 34	26	20 - 35	27	22 - 35	28	21 - 36	29	23 - 37	29	22 - 38
O6	27	21 - 35	27	21 - 36	28	22 - 36	29	22 - 38	30	23 - 38	30	23 - 40
O7	28	22 - 36	28	22 - 37	29	23 - 38	30	23 - 39	31	24 - 40	31	24 - 41
O8	22	17 - 28	22	17 - 29	23	18 - 29	23	18 - 30	24	19 - 31	24	18 - 32
O9	23	18 - 29	23	18 - 30	24	19 - 30	24	18 - 31	25	19 - 32	25	19 - 33
O10	23	19 - 30	24	18 - 31	25	19 - 32	25	19 - 33	26	20 - 33	26	20 - 34
O11	17	14 - 22	18	14 - 23	18	14 - 23	18	14 - 24	19	15 - 25	19	15 - 26
O12	18	14 - 23	18	14 - 24	19	15 - 25	19	15 - 25	20	16 - 26	20	16 - 27
O13	19	15 - 24	19	15 - 25	20	16 - 26	20	16 - 27	21	16 - 27	21	16 - 28
O14	16	12 - 20	16	12 - 21	16	13 - 21	17	13 - 22	17	14 - 22	17	13 - 23
Λ 1	19	15 - 24	19	15 - 25	20	16 - 25	20	15 - 26	21	16 - 26	21	16 - 27
Λ 2	18	14 - 23	18	14 - 24	19	15 - 24	19	15 - 25	20	16 - 26	20	16 - 26
Λ 3	17	14 - 22	17	13 - 22	18	14 - 23	18	14 - 24	19	15 - 24	19	15 - 25
Λ 4	16	13 - 21	16	13 - 21	17	14 - 22	17	13 - 22	18	14 - 23	18	14 - 24
Λ 5	17	13 - 21	17	13 - 22	18	14 - 23	18	14 - 23	19	15 - 24	19	14 - 25
Λ 6	16	13 - 20	16	12 - 21	17	13 - 21	17	13 - 22	18	14 - 22	18	14 - 23
Λ 7	15	12 - 19	15	12 - 20	16	13 - 20	16	12 - 21	17	13 - 21	17	13 - 22
Λ 8	16	13 - 21	16	13 - 21	17	14 - 22	17	13 - 23	18	14 - 23	18	14 - 24
Λ 9	15	12 - 19	15	12 - 20	16	13 - 21	16	13 - 21	17	13 - 22	17	13 - 22
Λ 10	14	12 - 18	15	11 - 19	15	12 - 19	15	12 - 20	16	13 - 20	16	13 - 21
Λ 11	15	12 - 19	15	12 - 20	16	13 - 20	16	13 - 21	17	13 - 22	17	13 - 22
Λ 12	16	12 - 20	16	12 - 21	16	13 - 21	17	13 - 22	17	14 - 22	17	13 - 23
Flat	23	18 - 30	23	18 - 31	24	19 - 31	24	18 - 32	25	19 - 33	25	19 - 34

^aIn μK . ^bIgnoring (No), and accounting for (Yes), the calibration-uncertainty correction. ^cSee Table 2 for model-parameter values. ^dCentral values (CV) are where the probability density distribution functions peak. ^eLimits are the $\pm 1\sigma$ ($\sim 68.27\%$ HPD) range.

TABLE 9
Numerical Values for $Q_{\text{rms-PS}}^{\text{a}}$, from Likelihood Analyses Using the Ka Data Set

Beamwidth:	-1σ	-1σ	-1σ	-1σ	Nom.	Nom.	Nom.	Nom.	$+1\sigma$	$+1\sigma$	$+1\sigma$	$+1\sigma$
Cal. Corr. ^b :	No	No	Yes	Yes	No	No	Yes	Yes	No	No	Yes	Yes
# ^c	CV ^d	Limits ^e	CV ^d	Limits ^e	CV ^d	Limits ^e	CV ^d	Limits ^e	CV ^d	Limits ^e	CV ^d	Limits ^e
(1)	(2)	(3)	(4)	(5)	(6)	(7)	(8)	(9)	(10)	(11)	(12)	(13)
O1	25	18 – 33	25	18 – 34	25	19 – 35	26	19 – 36	26	19 – 36	26	19 – 37
O2	24	18 – 33	24	18 – 34	25	19 – 34	25	18 – 35	26	19 – 36	26	19 – 37
O3	25	18 – 34	25	18 – 35	26	19 – 35	26	19 – 36	27	20 – 36	27	19 – 37
O4	25	19 – 34	26	19 – 35	26	19 – 36	26	19 – 37	27	20 – 37	27	20 – 38
O5	21	16 – 28	21	15 – 29	22	16 – 29	22	16 – 30	22	17 – 31	23	16 – 32
O6	21	16 – 29	22	16 – 30	22	17 – 30	22	16 – 31	23	17 – 32	23	17 – 32
O7	22	16 – 30	22	16 – 31	23	17 – 31	23	17 – 32	24	17 – 32	24	17 – 33
O8	17	13 – 23	18	13 – 24	18	13 – 24	18	13 – 25	19	14 – 25	19	14 – 26
O9	18	13 – 24	18	13 – 25	19	14 – 25	19	14 – 26	19	14 – 26	19	14 – 27
O10	19	14 – 25	19	14 – 26	19	14 – 26	19	14 – 27	20	15 – 27	20	15 – 28
O11	14	10 – 19	14	10 – 19	15	11 – 20	15	11 – 20	15	11 – 21	15	11 – 21
O12	15	11 – 20	15	11 – 20	15	11 – 20	15	11 – 21	16	12 – 21	16	11 – 22
O13	15	11 – 21	15	11 – 21	16	12 – 21	16	12 – 22	16	12 – 22	16	12 – 23
O14	13	9.4 – 17	13	9.3 – 17	13	9.7 – 18	13	9.7 – 18	14	10 – 19	14	10 – 19
Λ 1	15	11 – 20	15	11 – 21	16	12 – 21	16	12 – 22	16	12 – 22	17	12 – 23
Λ 2	15	11 – 20	15	11 – 20	15	11 – 20	15	11 – 21	16	12 – 21	16	12 – 22
Λ 3	14	10 – 18	14	10 – 19	14	11 – 19	14	11 – 20	15	11 – 20	15	11 – 21
Λ 4	13	9.8 – 18	13	9.7 – 18	14	10 – 18	14	10 – 19	14	11 – 19	14	11 – 20
Λ 5	14	10 – 18	14	10 – 19	14	11 – 19	14	10 – 20	15	11 – 20	15	11 – 21
Λ 6	13	9.6 – 17	13	9.5 – 18	13	10 – 18	14	9.9 – 19	14	10 – 19	14	10 – 19
Λ 7	12	9.1 – 16	12	9.0 – 17	13	9.5 – 17	13	9.4 – 18	13	9.8 – 18	13	9.8 – 18
Λ 8	13	9.8 – 18	13	9.7 – 18	14	10 – 18	14	10 – 19	14	11 – 19	14	10 – 20
Λ 9	12	9.2 – 17	12	9.1 – 17	13	9.6 – 17	13	9.5 – 18	13	10 – 18	14	9.9 – 19
Λ 10	12	8.7 – 16	12	8.6 – 16	12	9.1 – 16	12	9.0 – 17	13	9.5 – 17	13	9.4 – 18
Λ 11	12	9.2 – 17	12	9.1 – 17	13	9.5 – 17	13	9.5 – 18	13	9.9 – 18	13	9.8 – 19
Λ 12	13	9.4 – 17	13	9.3 – 17	13	9.7 – 18	13	9.7 – 18	14	10 – 19	14	10 – 19
Flat	18	13 – 24	18	13 – 25	18	13 – 25	18	13 – 26	19	14 – 26	19	14 – 27

^aIn μK . ^bIgnoring (No), and accounting for (Yes), the calibration-uncertainty correction. ^cSee Table 2 for model-parameter values. ^dCentral values (CV) are where the probability density distribution functions peak. ^eLimits are the $\pm 1\sigma$ ($\sim 68.27\%$ HPD) range.

TABLE 10
 Numerical Values for $Q_{\text{rms-PS}}^{\text{a}}$, from Likelihood Analyses Using the Ka2 Data Set

Beamwidth:	-1σ	-1σ	-1σ	-1σ	Nom.	Nom.	Nom.	Nom.	$+1\sigma$	$+1\sigma$	$+1\sigma$	$+1\sigma$
Cal. Corr. ^b :	No	No	Yes	Yes	No	No	Yes	Yes	No	No	Yes	Yes
# ^c	CV ^d	Limits ^e	CV ^d	Limits ^e	CV ^d	Limits ^e	CV ^d	Limits ^e	CV ^d	Limits ^e	CV ^d	Limits ^e
(1)	(2)	(3)	(4)	(5)	(6)	(7)	(8)	(9)	(10)	(11)	(12)	(13)
O1	13	< 36	13	< 37	13	< 37	13	< 39	13	< 39	13	< 40
O2	13	< 35	13	< 36	13	< 37	13	< 38	13	< 38	13	< 40
O3	13	< 36	13	< 37	13	< 37	13	< 39	14	< 39	14	< 41
O4	13	< 37	13	< 38	14	< 38	13	< 40	14	< 40	14	< 42
O5	11	< 30	11	< 31	12	< 31	11	< 33	12	< 33	12	< 34
O6	11	< 31	11	< 32	12	< 32	12	< 34	12	< 34	12	< 35
O7	12	< 32	12	< 33	12	< 33	12	< 35	12	< 35	12	< 36
O8	9.3	< 25	9.3	< 26	9.6	< 26	9.6	< 27	9.8	< 27	9.8	< 28
O9	9.6	< 26	9.6	< 27	9.8	< 27	9.8	< 28	10	< 28	10	< 29
O10	9.9	< 27	9.8	< 28	10	< 28	10	< 29	10	< 29	10	< 31
O11	7.6	< 20	7.6	< 21	7.8	< 21	7.8	< 22	8.0	< 22	8.0	< 23
O12	7.8	< 21	7.8	< 22	8.0	< 22	8.0	< 23	8.2	< 23	8.2	< 24
O13	8.1	< 22	8.1	< 23	8.3	< 23	8.3	< 24	8.5	< 24	8.5	< 25
O14	6.8	< 18	6.9	< 19	7.1	< 19	7.1	< 20	7.3	< 20	7.3	< 21
Λ 1	8.2	< 21	8.2	< 22	8.6	< 22	8.5	< 23	8.9	< 23	8.9	< 25
Λ 2	7.9	< 21	7.9	< 21	8.2	< 22	8.2	< 23	8.5	< 23	8.5	< 24
Λ 3	7.5	< 19	7.5	< 20	7.8	< 20	7.8	< 21	8.1	< 22	8.1	< 23
Λ 4	7.2	< 18	7.2	< 19	7.5	< 19	7.4	< 20	7.7	< 20	7.7	< 21
Λ 5	7.4	< 19	7.4	< 20	7.7	< 20	7.7	< 21	7.9	< 21	7.9	< 22
Λ 6	7.0	< 18	7.0	< 19	7.3	< 19	7.3	< 20	7.5	< 20	7.5	< 21
Λ 7	6.7	< 17	6.7	< 18	6.9	< 18	6.9	< 19	7.2	< 19	7.2	< 20
Λ 8	7.1	< 19	7.1	< 19	7.4	< 20	7.4	< 20	7.6	< 21	7.6	< 22
Λ 9	6.7	< 17	6.7	< 18	7.0	< 18	7.0	< 19	7.2	< 19	7.2	< 20
Λ 10	6.4	< 16	6.4	< 17	6.6	< 17	6.7	< 18	6.9	< 18	6.9	< 19
Λ 11	6.7	< 17	6.7	< 18	7.0	< 18	7.0	< 19	7.2	< 19	7.2	< 20
Λ 12	6.8	< 18	6.9	< 19	7.1	< 19	7.1	< 20	7.3	< 20	7.3	< 21
Flat	9.1	< 26	9.1	< 27	9.2	< 27	9.2	< 28	9.4	< 28	9.3	< 29

^aIn μK . ^bIgnoring (No), and accounting for (Yes), the calibration-uncertainty correction. ^cSee Table 2 for model-parameter values. ^dCentral values (CV) are where the probability density distribution functions peak. ^eLimits are 2σ ($\sim 97.72\%$ ET) upper limits.

TABLE 11
Numerical Values for $Q_{\text{rms-PS}}^{\text{a}}$, from Likelihood Analyses Using the Q2 Data Set

Beamwidth:	-1σ	-1σ	-1σ	-1σ	Nom.	Nom.	Nom.	Nom.	$+1\sigma$	$+1\sigma$	$+1\sigma$	$+1\sigma$
Cal. Corr. ^b :	No	No	Yes	Yes	No	No	Yes	Yes	No	No	Yes	Yes
# ^c	CV ^d Limits ^e		CV ^d Limits ^e		CV ^d Limits ^e		CV ^d Limits ^e		CV ^d Limits ^e		CV ^d Limits ^e	
(1)	(2)	(3)	(4)	(5)	(6)	(7)	(8)	(9)	(10)	(11)	(12)	(13)
O1	32	24 - 43	33	24 - 44	33	25 - 44	34	25 - 46	34	26 - 46	35	26 - 47
O2	32	24 - 42	32	24 - 44	33	25 - 44	33	25 - 45	34	26 - 46	34	25 - 47
O3	33	25 - 43	33	24 - 44	34	26 - 45	34	25 - 46	35	26 - 46	35	26 - 48
O4	33	25 - 44	34	25 - 46	34	26 - 46	35	26 - 47	36	27 - 47	36	26 - 49
O5	28	21 - 36	28	21 - 37	29	22 - 38	29	21 - 39	30	22 - 39	30	22 - 40
O6	28	21 - 37	29	21 - 39	29	22 - 39	30	22 - 40	30	23 - 40	31	23 - 42
O7	29	22 - 39	29	22 - 40	30	23 - 40	30	23 - 41	31	24 - 42	31	23 - 43
O8	23	17 - 30	23	17 - 31	24	18 - 31	24	18 - 32	25	19 - 33	25	18 - 34
O9	24	18 - 31	24	18 - 32	24	19 - 32	25	18 - 33	25	19 - 34	26	19 - 35
O10	25	19 - 32	25	18 - 33	25	19 - 34	26	19 - 35	26	20 - 35	26	20 - 36
O11	18	14 - 24	19	14 - 25	19	15 - 25	19	14 - 26	20	15 - 26	20	15 - 27
O12	19	15 - 25	19	14 - 26	20	15 - 26	20	15 - 27	21	16 - 27	21	15 - 28
O13	20	15 - 26	20	15 - 27	21	16 - 27	21	15 - 28	21	16 - 29	22	16 - 29
O14	17	13 - 22	17	12 - 23	17	13 - 23	17	13 - 24	18	14 - 24	18	13 - 25
Λ 1	20	15 - 26	20	15 - 27	21	16 - 27	21	16 - 28	22	16 - 29	22	16 - 30
Λ 2	19	15 - 25	19	14 - 26	20	15 - 26	20	15 - 27	21	16 - 28	21	16 - 28
Λ 3	18	14 - 24	18	14 - 25	19	14 - 25	19	14 - 26	20	15 - 26	20	15 - 27
Λ 4	17	13 - 23	17	13 - 24	18	14 - 24	18	14 - 25	19	14 - 25	19	14 - 26
Λ 5	18	14 - 24	18	13 - 24	19	14 - 25	19	14 - 25	19	15 - 26	20	15 - 26
Λ 6	17	13 - 22	17	13 - 23	18	13 - 23	18	13 - 24	18	14 - 24	19	14 - 25
Λ 7	16	12 - 21	16	12 - 22	17	13 - 22	17	13 - 23	17	13 - 23	18	13 - 24
Λ 8	17	13 - 23	17	13 - 23	18	14 - 24	18	13 - 24	19	14 - 25	19	14 - 25
Λ 9	16	12 - 21	16	12 - 22	17	13 - 22	17	13 - 23	18	13 - 23	18	13 - 24
Λ 10	15	12 - 20	16	12 - 21	16	12 - 21	16	12 - 22	17	13 - 22	17	13 - 23
Λ 11	16	12 - 21	16	12 - 22	17	13 - 22	17	13 - 23	18	13 - 23	18	13 - 24
Λ 12	17	13 - 22	17	12 - 23	17	13 - 23	17	13 - 24	18	14 - 24	18	13 - 25
Flat	23	18 - 31	24	17 - 32	24	18 - 32	24	18 - 33	25	19 - 33	25	18 - 34

^aIn μK . ^bIgnoring (No), and accounting for (Yes), the calibration-uncertainty correction. ^cSee Table 2 for model-parameter values. ^dCentral values (CV) are where the probability density distribution functions peak. ^eLimits are the $\pm 1\sigma$ ($\sim 68.27\%$ HPD) range.

TABLE 12
Renormalized Maximum and Marginalized (over $Q_{\text{rms-PS}}$) Values of the Probability Density
Distribution Functions, for the Ka + Q Data Set

Beamwidth:	-1σ	-1σ	Nom.	Nom.	$+1\sigma$	$+1\sigma$	-1σ	-1σ	Nom.	Nom.	$+1\sigma$	$+1\sigma$
Cal. Corr. ^a :	No	Yes	No	Yes	No	Yes	No	Yes	No	Yes	No	Yes
# ^b	Max. ^c	Max. ^c	Max. ^c	Max. ^c	Max. ^c	Max. ^c	Mar. ^d	Mar. ^d	Mar. ^d	Mar. ^d	Mar. ^d	Mar. ^d
(1)	(2)	(3)	(4)	(5)	(6)	(7)	(8)	(9)	(10)	(11)	(12)	(13)
O1	1.0	1.0	0.99	0.99	0.94	0.95	1.0	1.0	0.99	0.99	0.98	0.98
O2	0.97	0.97	0.98	0.99	0.96	0.97	0.93	0.93	0.95	0.95	0.96	0.96
O3	0.98	0.98	0.98	0.98	0.95	0.96	0.96	0.96	0.97	0.97	0.98	0.98
O4	0.98	0.98	0.98	0.98	0.94	0.95	1.0	1.0	1.0	1.0	1.0	1.0
O5	0.96	0.95	0.98	0.98	0.97	0.97	0.78	0.78	0.80	0.80	0.82	0.82
O6	0.97	0.96	0.98	0.98	0.96	0.97	0.82	0.82	0.83	0.83	0.85	0.85
O7	0.98	0.97	0.98	0.98	0.95	0.96	0.86	0.86	0.87	0.87	0.88	0.88
O8	0.95	0.95	0.98	0.97	0.97	0.97	0.64	0.64	0.66	0.66	0.68	0.68
O9	0.97	0.96	0.98	0.98	0.97	0.97	0.68	0.68	0.69	0.69	0.71	0.71
O10	0.98	0.98	0.99	0.99	0.97	0.97	0.72	0.72	0.73	0.73	0.74	0.74
O11	0.94	0.93	0.97	0.97	0.97	0.97	0.50	0.50	0.52	0.52	0.54	0.54
O12	0.96	0.96	0.99	0.99	0.98	0.98	0.54	0.54	0.56	0.56	0.58	0.58
O13	0.99	0.98	1.0	1.0	0.98	0.99	0.59	0.59	0.60	0.60	0.61	0.61
O14	0.95	0.95	0.99	0.99	1.0	1.0	0.46	0.46	0.48	0.48	0.50	0.50
A1	0.78	0.77	0.83	0.82	0.85	0.85	0.44	0.44	0.47	0.47	0.50	0.50
A2	0.86	0.86	0.91	0.91	0.93	0.93	0.47	0.47	0.50	0.50	0.53	0.53
A3	0.83	0.82	0.88	0.87	0.90	0.90	0.42	0.42	0.45	0.45	0.48	0.48
A4	0.80	0.79	0.85	0.84	0.88	0.87	0.39	0.39	0.42	0.42	0.45	0.45
A5	0.89	0.89	0.94	0.93	0.96	0.95	0.46	0.46	0.48	0.48	0.51	0.51
A6	0.85	0.84	0.90	0.90	0.92	0.92	0.41	0.41	0.43	0.43	0.46	0.46
A7	0.82	0.81	0.87	0.86	0.90	0.89	0.37	0.37	0.40	0.40	0.42	0.42
A8	0.92	0.91	0.96	0.96	0.98	0.98	0.45	0.45	0.48	0.48	0.51	0.51
A9	0.88	0.87	0.92	0.92	0.94	0.94	0.41	0.41	0.43	0.43	0.46	0.46
A10	0.84	0.83	0.89	0.88	0.91	0.91	0.36	0.36	0.39	0.39	0.42	0.42
A11	0.91	0.90	0.95	0.95	0.97	0.96	0.42	0.42	0.44	0.44	0.47	0.47
A12	0.95	0.95	0.99	0.99	1.0	1.0	0.46	0.46	0.48	0.48	0.50	0.50
Flat	0.95	0.95	0.93	0.93	0.88	0.89	0.70	0.70	0.69	0.69	0.68	0.68
Highest ^{c,d} :	1.4	1.3	1.4	1.3	1.4	1.3	2.7	2.8	2.9	2.9	3.0	3.0

^aIgnoring (No), and accounting for (Yes), the calibration-uncertainty correction. ^bSee Table 2 for model-parameter values. ^cRenormalized maximum values of the probability density distribution functions, renormalized such that it is unity for the model with the highest maximum value of the probability density distribution function, for this data set, and the appropriate beamwidth and calibration-uncertainty treatment. The last line of the table gives the value for the model with highest maximum value of the probability density distribution function when the likelihoods are normalized according to $L(Q_{\text{rms-PS}} = 0 \mu\text{K}) = 10^{-19}$. ^dRenormalized values of the marginalized (over $Q_{\text{rms-PS}}$) probability density distribution functions, renormalized such that it is unity for the model with the highest marginal probability distribution function value, for this data set, and the appropriate beamwidth and calibration-uncertainty treatment. The last line of the table gives the value for the model with the highest marginal probability distribution function value when the likelihoods are normalized according to $L(Q_{\text{rms-PS}} = 0 \mu\text{K}) = 10^{-20}$.

TABLE 13
Renormalized Maximum and Marginalized (over $Q_{\text{rms-PS}}$) Values of the Probability Density
Distribution Functions, for the Ka Data Set

Beamwidth:	-1σ	-1σ	Nom.	Nom.	$+1\sigma$	$+1\sigma$	-1σ	-1σ	Nom.	Nom.	$+1\sigma$	$+1\sigma$
Cal. Corr. ^a :	No	Yes	No	Yes	No	Yes	No	Yes	No	Yes	No	Yes
# ^b	Max. ^c	Max. ^c	Max. ^c	Max. ^c	Max. ^c	Max. ^c	Mar. ^d	Mar. ^d	Mar. ^d	Mar. ^d	Mar. ^d	Mar. ^d
(1)	(2)	(3)	(4)	(5)	(6)	(7)	(8)	(9)	(10)	(11)	(12)	(13)
O1	0.96	0.96	0.97	0.97	0.98	0.98	1.0	1.0	1.0	1.0	1.0	1.0
O2	0.84	0.84	0.86	0.86	0.88	0.88	0.85	0.85	0.87	0.87	0.88	0.88
O3	0.87	0.87	0.89	0.89	0.90	0.90	0.90	0.90	0.91	0.91	0.92	0.92
O4	0.90	0.90	0.91	0.91	0.93	0.92	0.96	0.96	0.96	0.96	0.97	0.97
O5	0.79	0.78	0.81	0.81	0.83	0.83	0.68	0.68	0.69	0.69	0.71	0.71
O6	0.82	0.82	0.84	0.84	0.86	0.86	0.73	0.73	0.74	0.74	0.76	0.76
O7	0.86	0.86	0.88	0.87	0.89	0.89	0.79	0.79	0.80	0.80	0.81	0.81
O8	0.76	0.75	0.78	0.78	0.81	0.80	0.54	0.54	0.56	0.56	0.57	0.57
O9	0.80	0.80	0.82	0.82	0.84	0.84	0.59	0.59	0.61	0.61	0.62	0.62
O10	0.84	0.84	0.86	0.86	0.88	0.88	0.65	0.65	0.66	0.66	0.67	0.67
O11	0.72	0.72	0.75	0.75	0.78	0.77	0.41	0.41	0.43	0.43	0.44	0.44
O12	0.77	0.76	0.79	0.79	0.82	0.81	0.46	0.46	0.47	0.47	0.49	0.49
O13	0.82	0.82	0.84	0.84	0.86	0.86	0.52	0.52	0.53	0.53	0.54	0.54
O14	0.71	0.70	0.74	0.73	0.77	0.77	0.36	0.36	0.38	0.38	0.39	0.39
A1	0.52	0.52	0.55	0.55	0.58	0.58	0.32	0.32	0.34	0.34	0.35	0.35
A2	0.61	0.60	0.64	0.63	0.67	0.67	0.36	0.36	0.38	0.38	0.39	0.39
A3	0.57	0.56	0.60	0.59	0.63	0.63	0.32	0.32	0.33	0.33	0.35	0.35
A4	0.53	0.53	0.56	0.56	0.60	0.59	0.28	0.28	0.30	0.30	0.32	0.32
A5	0.63	0.63	0.67	0.66	0.70	0.69	0.35	0.35	0.37	0.37	0.38	0.38
A6	0.59	0.58	0.62	0.62	0.65	0.65	0.31	0.31	0.32	0.32	0.34	0.34
A7	0.55	0.55	0.58	0.58	0.62	0.61	0.27	0.27	0.29	0.29	0.30	0.30
A8	0.66	0.66	0.69	0.69	0.73	0.72	0.35	0.35	0.37	0.37	0.39	0.39
A9	0.61	0.61	0.64	0.64	0.68	0.67	0.31	0.31	0.32	0.32	0.34	0.34
A10	0.57	0.57	0.60	0.60	0.63	0.63	0.27	0.27	0.28	0.28	0.30	0.30
A11	0.65	0.64	0.68	0.67	0.71	0.71	0.32	0.32	0.34	0.34	0.35	0.35
A12	0.71	0.70	0.74	0.73	0.77	0.77	0.36	0.36	0.38	0.38	0.39	0.39
Flat	1.0	1.0	1.0	1.0	1.0	1.0	0.76	0.76	0.75	0.75	0.74	0.74
Highest ^{c,d} :	1.0	0.97	1.0	0.95	0.99	0.94	1.8	1.9	1.9	1.9	2.0	2.0

^aIgnoring (No), and accounting for (Yes), the calibration-uncertainty correction. ^bSee Table 2 for model-parameter values. ^cRenormalized maximum values of the probability density distribution functions, renormalized such that it is unity for the model with the highest maximum value of the probability density distribution function, for this data set, and the appropriate beamwidth and calibration-uncertainty treatment. The last line of the table gives the value for the model with highest maximum value of the probability density distribution function when the likelihoods are normalized according to $L(Q_{\text{rms-PS}} = 0 \mu\text{K}) = 10^{-6}$. ^dRenormalized values of the marginalized (over $Q_{\text{rms-PS}}$) probability density distribution functions, renormalized such that it is unity for the model with the highest marginal probability distribution function value, for this data set, and the appropriate beamwidth and calibration-uncertainty treatment. The last line of the table gives the value for the model with the highest marginal probability distribution function value when the likelihoods are normalized according to $L(Q_{\text{rms-PS}} = 0 \mu\text{K}) = 10^{-7}$.

TABLE 14
Renormalized Maximum and Marginalized (over $Q_{\text{rms-PS}}$) Values of the Probability Density Distribution Functions, for the Ka2 Data Set

Beamwidth:	-1σ	-1σ	Nom.	Nom.	$+1\sigma$	$+1\sigma$	-1σ	-1σ	Nom.	Nom.	$+1\sigma$	$+1\sigma$
Cal. Corr. ^a :	No	Yes	No	Yes	No	Yes	No	Yes	No	Yes	No	Yes
# ^b	Max. ^c	Max. ^c	Max. ^c	Max. ^c	Max. ^c	Max. ^c	Mar. ^d	Mar. ^d	Mar. ^d	Mar. ^d	Mar. ^d	Mar. ^d
(1)	(2)	(3)	(4)	(5)	(6)	(7)	(8)	(9)	(10)	(11)	(12)	(13)
O1	0.93	0.94	0.93	0.93	0.93	0.93	0.96	0.96	0.96	0.96	0.96	0.96
O2	0.96	0.96	0.95	0.96	0.95	0.95	0.97	0.97	0.97	0.97	0.97	0.97
O3	0.95	0.95	0.95	0.95	0.95	0.95	0.98	0.98	0.99	0.99	0.99	0.99
O4	0.94	0.95	0.94	0.94	0.94	0.94	1.0	1.0	1.0	1.0	1.0	1.0
O5	0.97	0.97	0.97	0.97	0.96	0.97	0.84	0.84	0.85	0.85	0.85	0.85
O6	0.96	0.96	0.96	0.96	0.96	0.96	0.86	0.86	0.87	0.87	0.87	0.87
O7	0.95	0.96	0.95	0.95	0.95	0.95	0.88	0.88	0.89	0.89	0.89	0.89
O8	0.97	0.97	0.97	0.97	0.97	0.97	0.70	0.70	0.71	0.71	0.71	0.71
O9	0.97	0.97	0.96	0.96	0.96	0.96	0.72	0.72	0.73	0.73	0.73	0.73
O10	0.96	0.96	0.95	0.96	0.95	0.95	0.74	0.74	0.75	0.75	0.75	0.75
O11	0.98	0.98	0.98	0.98	0.98	0.98	0.57	0.57	0.57	0.57	0.58	0.58
O12	0.97	0.97	0.97	0.97	0.97	0.97	0.59	0.59	0.59	0.59	0.60	0.60
O13	0.96	0.96	0.96	0.96	0.96	0.96	0.61	0.61	0.61	0.61	0.61	0.62
O14	0.99	0.99	0.98	0.98	0.98	0.98	0.52	0.52	0.52	0.52	0.53	0.53
A1	1.0	1.0	1.0	1.0	1.0	1.0	0.61	0.62	0.63	0.63	0.64	0.64
A2	1.0	1.0	0.99	0.99	0.99	0.99	0.60	0.60	0.61	0.61	0.61	0.62
A3	1.0	1.0	1.0	1.0	1.0	1.0	0.56	0.57	0.57	0.58	0.58	0.58
A4	1.0	1.0	1.0	1.0	1.0	1.0	0.54	0.54	0.55	0.55	0.56	0.56
A5	0.99	0.99	0.99	0.99	0.99	0.99	0.56	0.56	0.57	0.57	0.57	0.57
A6	1.0	1.0	1.0	1.0	1.0	1.0	0.53	0.53	0.54	0.54	0.54	0.54
A7	1.0	1.0	1.0	1.0	1.0	1.0	0.50	0.50	0.51	0.51	0.52	0.52
A8	0.99	0.99	0.99	0.99	0.99	0.99	0.54	0.54	0.55	0.55	0.55	0.55
A9	1.0	1.0	0.99	0.99	0.99	0.99	0.51	0.51	0.52	0.52	0.52	0.52
A10	1.0	1.0	1.0	1.0	1.0	1.0	0.48	0.48	0.49	0.49	0.50	0.50
A11	0.99	0.99	0.99	0.99	0.99	0.99	0.51	0.51	0.51	0.51	0.52	0.52
A12	0.99	0.99	0.98	0.98	0.98	0.98	0.52	0.52	0.52	0.52	0.53	0.53
Flat	0.93	0.93	0.93	0.93	0.93	0.93	0.69	0.69	0.69	0.69	0.68	0.68
Highest ^{c,d} :	1.8	1.8	1.8	1.8	1.8	1.7	3.9	3.9	4.0	4.0	4.0	4.1

^aIgnoring (No), and accounting for (Yes), the calibration-uncertainty correction. ^bSee Table 2 for model-parameter values. ^cRenormalized maximum values of the probability density distribution functions, renormalized such that it is unity for the model with the highest maximum value of the probability density distribution function, for this data set, and the appropriate beamwidth and calibration-uncertainty treatment. The last line of the table gives the value for the model with highest maximum value of the probability density distribution function when the likelihoods are normalized according to $L(Q_{\text{rms-PS}} = 0 \mu\text{K}) = 1$. ^dRenormalized values of the marginalized (over $Q_{\text{rms-PS}}$) probability density distribution functions, renormalized such that it is unity for the model with the highest marginal probability distribution function value, for this data set, and the appropriate beamwidth and calibration-uncertainty treatment. The last line of the table gives the value for the model with the highest marginal probability distribution function value when the likelihoods are normalized according to $L(Q_{\text{rms-PS}} = 0 \mu\text{K}) = 0.1$.

TABLE 15
Renormalized Maximum and Marginalized (over $Q_{\text{rms-PS}}$) Values of the Probability Density Distribution Functions, for the Q2 Data Set

Beamwidth:	-1σ	-1σ	Nom.	Nom.	$+1\sigma$	$+1\sigma$	-1σ	-1σ	Nom.	Nom.	$+1\sigma$	$+1\sigma$
Cal. Corr. ^a :	No	Yes	No	Yes	No	Yes	No	Yes	No	Yes	No	Yes
# ^b	Max. ^c	Max. ^c	Max. ^c	Max. ^c	Max. ^c	Max. ^c	Mar. ^d	Mar. ^d	Mar. ^d	Mar. ^d	Mar. ^d	Mar. ^d
(1)	(2)	(3)	(4)	(5)	(6)	(7)	(8)	(9)	(10)	(11)	(12)	(13)
O1	0.96	0.96	0.97	0.97	0.98	0.98	1.0	1.0	1.0	1.0	1.0	1.0
O2	0.77	0.77	0.79	0.78	0.80	0.80	0.78	0.78	0.79	0.79	0.80	0.80
O3	0.81	0.81	0.82	0.82	0.84	0.84	0.84	0.84	0.85	0.85	0.86	0.86
O4	0.86	0.85	0.87	0.87	0.88	0.88	0.91	0.91	0.92	0.92	0.92	0.92
O5	0.68	0.68	0.69	0.69	0.71	0.71	0.59	0.59	0.60	0.60	0.61	0.61
O6	0.72	0.72	0.74	0.74	0.76	0.75	0.65	0.65	0.66	0.66	0.67	0.67
O7	0.78	0.78	0.79	0.79	0.81	0.81	0.73	0.73	0.73	0.73	0.74	0.74
O8	0.64	0.64	0.66	0.65	0.67	0.67	0.46	0.46	0.47	0.47	0.48	0.48
O9	0.69	0.69	0.71	0.70	0.72	0.72	0.52	0.52	0.53	0.53	0.54	0.54
O10	0.75	0.75	0.77	0.77	0.78	0.78	0.59	0.59	0.59	0.59	0.60	0.60
O11	0.59	0.59	0.61	0.61	0.63	0.62	0.34	0.34	0.35	0.35	0.36	0.36
O12	0.65	0.65	0.67	0.66	0.68	0.68	0.39	0.39	0.40	0.40	0.41	0.41
O13	0.71	0.71	0.73	0.73	0.75	0.74	0.45	0.45	0.46	0.46	0.47	0.47
O14	0.58	0.57	0.59	0.59	0.61	0.61	0.30	0.30	0.31	0.31	0.32	0.32
A1	0.38	0.38	0.40	0.40	0.41	0.41	0.24	0.24	0.25	0.25	0.26	0.26
A2	0.47	0.47	0.48	0.48	0.50	0.50	0.28	0.28	0.29	0.29	0.30	0.30
A3	0.43	0.42	0.44	0.44	0.46	0.46	0.24	0.24	0.25	0.25	0.26	0.26
A4	0.39	0.39	0.41	0.41	0.42	0.42	0.21	0.21	0.22	0.22	0.23	0.23
A5	0.50	0.49	0.52	0.51	0.53	0.53	0.28	0.28	0.29	0.29	0.30	0.30
A6	0.45	0.45	0.47	0.46	0.48	0.48	0.24	0.24	0.25	0.25	0.26	0.26
A7	0.41	0.41	0.42	0.42	0.44	0.44	0.21	0.21	0.21	0.21	0.22	0.22
A8	0.53	0.52	0.55	0.54	0.56	0.56	0.28	0.28	0.29	0.29	0.30	0.30
A9	0.47	0.47	0.49	0.48	0.51	0.50	0.24	0.24	0.25	0.25	0.26	0.26
A10	0.43	0.42	0.44	0.44	0.46	0.46	0.21	0.21	0.21	0.21	0.22	0.22
A11	0.51	0.50	0.53	0.52	0.54	0.54	0.26	0.26	0.27	0.27	0.28	0.28
A12	0.58	0.57	0.59	0.59	0.61	0.61	0.30	0.30	0.31	0.31	0.32	0.32
Flat	1.0	1.0	1.0	1.0	1.0	1.0	0.76	0.76	0.75	0.75	0.74	0.74
Highest ^{c,d} :	2.4	2.2	2.5	2.4	2.7	2.5	5.2	5.2	5.8	5.8	6.4	6.5

^aIgnoring (No), and accounting for (Yes), the calibration-uncertainty correction. ^bSee Table 2 for model-parameter values. ^cRenormalized maximum values of the probability density distribution functions, renormalized such that it is unity for the model with the highest maximum value of the probability density distribution function, for this data set, and the appropriate beamwidth and calibration-uncertainty treatment. The last line of the table gives the value for the model with highest maximum value of the probability density distribution function when the likelihoods are normalized according to $L(Q_{\text{rms-PS}} = 0 \mu\text{K}) = 10^{-6}$. ^dRenormalized values of the marginalized (over $Q_{\text{rms-PS}}$) probability density distribution functions, renormalized such that it is unity for the model with the highest marginal probability distribution function value, for this data set, and the appropriate beamwidth and calibration-uncertainty treatment. The last line of the table gives the value for the model with the highest marginal probability distribution function value when the likelihoods are normalized according to $L(Q_{\text{rms-PS}} = 0 \mu\text{K}) = 10^{-7}$.

TABLE 16
Numerical Values from Likelihood Analyses Using the Ka1 Data Set

Data Set:	DMR	SP94	SP94	SP94	SP94	SP94	SP94
# ^a	$Q_{\text{rms-PS}}^{\text{b}}$ (μK)	$Q_{\text{rms-PS}}^{\text{c}}$ (μK)	$Q_{\text{rms-PS}}^{\text{d}}$ (μK)	δT_l^{d} (μK)	δT_l^{c} (μK)	Max. ^e	Mar. ^f
(1)	(2)	(3)	(4)	(5)	(6)	(7)	(8)
O1	20.5 – 25.6	27 – 63	42	46	30 – 71	0.72	0.93
O2	23.6 – 29.4	27 – 62	41	45	30 – 69	0.80	0.99
O3	23.6 – 29.4	27 – 63	42	45	30 – 69	0.78	1.0
O4	23.6 – 29.4	28 – 65	43	46	30 – 70	0.76	1.0
O5	23.0 – 28.6	23 – 53	35	45	30 – 68	0.85	0.90
O6	23.0 – 28.6	24 – 55	36	45	30 – 69	0.83	0.91
O7	23.0 – 28.6	25 – 57	37	45	30 – 69	0.80	0.92
O8	20.8 – 25.9	19 – 44	29	45	30 – 68	0.88	0.77
O9	20.8 – 25.9	20 – 46	30	45	30 – 68	0.85	0.78
O10	20.8 – 25.9	21 – 47	31	45	30 – 69	0.83	0.79
O11	18.3 – 22.8	16 – 35	23	45	30 – 68	0.91	0.64
O12	18.3 – 22.8	16 – 37	24	45	30 – 68	0.88	0.65
O13	18.3 – 22.8	17 – 39	25	45	30 – 69	0.85	0.66
O14	17.7 – 22.0	14 – 32	21	44	30 – 68	0.95	0.59
A1	22.8 – 28.4	17 – 38	25	44	29 – 67	0.99	0.72
A2	21.1 – 26.3	16 – 37	24	44	30 – 67	0.97	0.69
A3	21.1 – 26.3	15 – 35	23	44	30 – 67	0.99	0.66
A4	21.1 – 26.3	15 – 33	22	44	29 – 67	1.0	0.64
A5	19.8 – 24.7	15 – 34	23	44	30 – 67	0.97	0.65
A6	19.8 – 24.7	14 – 32	21	44	30 – 67	0.99	0.62
A7	19.8 – 24.7	13 – 31	20	44	30 – 67	1.0	0.59
A8	19.0 – 23.7	15 – 33	22	44	30 – 68	0.96	0.62
A9	19.0 – 23.7	14 – 31	21	44	30 – 67	0.98	0.59
A10	19.0 – 23.7	13 – 30	20	44	30 – 67	1.0	0.57
A11	18.5 – 23.1	14 – 31	21	44	30 – 67	0.97	0.59
A12	18.2 – 22.7	14 – 32	21	44	30 – 68	0.95	0.59
Flat	18.2 – 22.6	19 – 45	30	46	30 – 70	0.73	0.69

^aSee Table 2 for model-parameter values. ^bDMR 1σ range for open models is from two-year DMR (galactic-frame, quadrupole-excluded) normalization of Górski et al. (1995) (also see RBGS), for flat- Λ models from two-year DMR (ecliptic-frame, quadrupole-excluded) normalization of Bunn & Sugiyama (1995) (also see RS), and for flat bandpower from two-year DMR (galactic-frame, quadrupole-excluded) normalization of Górski et al. (1994). DMR 1σ range accounts for DMR statistical and systematic uncertainties following Stompor et al. (1995) (also see RBGS; RS).

^cSP94 1σ ($\sim 68.27\%$ HPD) range, accounting for beamwidth- and calibration-uncertainty corrections. Lower limits are from -1σ beamwidth analyses, and upper limits from $+1\sigma$ beamwidth analyses (both account for the calibration-uncertainty correction). ^dValue at the peak of the calibration-uncertainty-corrected, nominal beamwidth, probability density distribution function. ^eRenormalized maximum values of the probability density distribution functions (at the nominal beamwidth and accounting for calibration uncertainty), renormalized such that it is unity for the model with the highest maximum value of the probability density distribution function, for this data set, where, in the convention with $L(Q_{\text{rms-PS}} = 0 \mu\text{K}) = 1$, it is 3.2×10^3 for the model with the highest value. ^fRenormalized values of the marginalized (over $Q_{\text{rms-PS}}$) probability density distribution functions (at the nominal beamwidth and accounting for calibration uncertainty), renormalized such that it is unity for the model with the highest marginal probability distribution function value, for this data set, where, in the convention with $L(Q_{\text{rms-PS}} = 0 \mu\text{K}) = 1$, it is 9.6×10^4 for the model with the highest value.

TABLE 17
Numerical Values from Likelihood Analyses Using the Ka2 Data Set

Data Set:	DMR	SP94	SP94	SP94	SP94	SP94	SP94
# ^a	$Q_{\text{rms-PS}}^{\text{b}}$ (μK)	$Q_{\text{rms-PS}}^{\text{c}}$ (μK)	$Q_{\text{rms-PS}}^{\text{d}}$ (μK)	δT_l^{d} (μK)	δT_l^{c} (μK)	Max. ^e	Mar. ^f
(1)	(2)	(3)	(4)	(5)	(6)	(7)	(8)
O1	20.5 – 25.6	< 40	13	14	< 45	0.93	0.96
O2	23.6 – 29.4	< 40	13	15	< 45	0.96	0.97
O3	23.6 – 29.4	< 41	13	15	< 45	0.95	0.99
O4	23.6 – 29.4	< 42	13	14	< 45	0.94	1.0
O5	23.0 – 28.6	< 34	11	15	< 45	0.97	0.85
O6	23.0 – 28.6	< 35	12	15	< 45	0.96	0.87
O7	23.0 – 28.6	< 36	12	15	< 45	0.95	0.89
O8	20.8 – 25.9	< 28	9.6	15	< 45	0.97	0.71
O9	20.8 – 25.9	< 29	9.8	15	< 45	0.96	0.73
O10	20.8 – 25.9	< 31	10	15	< 45	0.96	0.75
O11	18.3 – 22.8	< 23	7.8	15	< 45	0.98	0.57
O12	18.3 – 22.8	< 24	8.0	15	< 45	0.97	0.59
O13	18.3 – 22.8	< 25	8.3	15	< 45	0.96	0.61
O14	17.7 – 22.0	< 21	7.1	15	< 45	0.98	0.52
Λ 1	22.8 – 28.4	< 25	8.5	15	< 44	1.0	0.63
Λ 2	21.1 – 26.3	< 24	8.2	15	< 44	0.99	0.61
Λ 3	21.1 – 26.3	< 23	7.8	15	< 44	1.0	0.58
Λ 4	21.1 – 26.3	< 21	7.4	15	< 45	1.0	0.55
Λ 5	19.8 – 24.7	< 22	7.7	15	< 45	0.99	0.57
Λ 6	19.8 – 24.7	< 21	7.3	15	< 45	1.0	0.54
Λ 7	19.8 – 24.7	< 20	6.9	15	< 45	1.0	0.51
Λ 8	19.0 – 23.7	< 22	7.4	15	< 45	0.99	0.55
Λ 9	19.0 – 23.7	< 20	7.0	15	< 45	0.99	0.52
Λ 10	19.0 – 23.7	< 19	6.7	15	< 45	1.0	0.49
Λ 11	18.5 – 23.1	< 20	7.0	15	< 45	0.99	0.51
Λ 12	18.2 – 22.7	< 21	7.1	15	< 45	0.98	0.52
Flat	18.2 – 22.6	< 29	9.2	14	< 45	0.93	0.69

^aSee Table 2 for model-parameter values. ^bTwo-year DMR 1σ range accounts for DMR statistical and systematic uncertainties. ^cSP94 2σ ($\sim 97.72\%$ ET) upper limit, accounting for beamwidth- and calibration-uncertainty corrections. ^dValue at the peak of the calibration-uncertainty-corrected, nominal beamwidth, probability density distribution function. ^eRenormalized maximum values of the probability density distribution functions (at the nominal beamwidth and accounting for calibration uncertainty), renormalized such that it is unity for the model with the highest maximum value of the probability density distribution function, for this data set, where, in the convention with $L(Q_{\text{rms-PS}} = 0 \mu\text{K}) = 1$, it is 1.8 for the model with the highest value. ^fRenormalized values of the marginalized (over $Q_{\text{rms-PS}}$) probability density distribution functions (at the nominal beamwidth and accounting for calibration uncertainty), renormalized such that it is unity for the model with the highest marginal probability distribution function value, for this data set, where, in the convention with $L(Q_{\text{rms-PS}} = 0 \mu\text{K}) = 1$, it is 40 for the model with the highest value.

TABLE 18
Numerical Values from Likelihood Analyses Using the Ka3 Data Set

Data Set:	DMR	SP94	SP94	SP94	SP94	SP94	SP94
# ^a	$Q_{\text{rms-PS}}^{\text{b}}$ (μK)	$Q_{\text{rms-PS}}^{\text{c}}$ (μK)	$Q_{\text{rms-PS}}^{\text{d}}$ (μK)	δT_l^{d} (μK)	δT_l^{c} (μK)	Max. ^e	Mar. ^f
(1)	(2)	(3)	(4)	(5)	(6)	(7)	(8)
O1	20.5 – 25.6	19 – 43	29	32	21 – 48	0.97	1.0
O2	23.6 – 29.4	19 – 42	28	32	21 – 47	0.93	0.93
O3	23.6 – 29.4	19 – 43	29	32	21 – 47	0.94	0.97
O4	23.6 – 29.4	20 – 44	29	32	21 – 47	0.95	1.0
O5	23.0 – 28.6	16 – 36	24	32	21 – 48	0.91	0.78
O6	23.0 – 28.6	17 – 37	25	32	21 – 47	0.93	0.82
O7	23.0 – 28.6	17 – 38	26	32	21 – 47	0.94	0.86
O8	20.8 – 25.9	13 – 30	20	32	21 – 48	0.90	0.64
O9	20.8 – 25.9	14 – 31	21	32	21 – 48	0.92	0.68
O10	20.8 – 25.9	14 – 32	22	32	21 – 47	0.94	0.72
O11	18.3 – 22.8	11 – 24	16	32	21 – 48	0.89	0.51
O12	18.3 – 22.8	11 – 25	17	32	21 – 48	0.91	0.54
O13	18.3 – 22.8	12 – 26	18	32	21 – 48	0.93	0.58
O14	17.7 – 22.0	9.8 – 22	15	32	21 – 48	0.89	0.46
A1	22.8 – 28.4	12 – 26	18	32	21 – 48	0.77	0.47
A2	21.1 – 26.3	11 – 25	17	32	21 – 48	0.83	0.49
A3	21.1 – 26.3	11 – 24	16	32	21 – 48	0.80	0.45
A4	21.1 – 26.3	10 – 23	15	32	21 – 48	0.78	0.41
A5	19.8 – 24.7	11 – 24	16	32	21 – 48	0.85	0.47
A6	19.8 – 24.7	9.9 – 22	15	32	21 – 48	0.82	0.43
A7	19.8 – 24.7	9.4 – 21	14	32	21 – 48	0.79	0.39
A8	19.0 – 23.7	10 – 23	15	32	21 – 48	0.86	0.46
A9	19.0 – 23.7	9.6 – 21	14	32	21 – 48	0.83	0.42
A10	19.0 – 23.7	9.1 – 20	14	32	21 – 48	0.80	0.38
A11	18.5 – 23.1	9.6 – 21	14	32	21 – 48	0.85	0.43
A12	18.2 – 22.7	9.8 – 22	15	32	21 – 48	0.89	0.46
Flat	18.2 – 22.6	14 – 30	20	32	21 – 47	1.0	0.74

^aSee Table 2 for model-parameter values. ^bTwo-year DMR 1σ range accounts for DMR statistical and systematic uncertainties. ^cSP94 1σ ($\sim 68.27\%$ HPD) range, accounting for beamwidth- and calibration-uncertainty corrections. ^dValue at the peak of the calibration-uncertainty-corrected, nominal beamwidth, probability density distribution function. ^eRenormalized maximum values of the probability density distribution functions (at the nominal beamwidth and accounting for calibration uncertainty), renormalized such that it is unity for the model with the highest maximum value of the probability density distribution function, for this data set, where, in the convention with $L(Q_{\text{rms-PS}} = 0 \mu\text{K}) = 1$, it is 590 for the model with the highest value. ^fRenormalized values of the marginalized (over $Q_{\text{rms-PS}}$) probability density distribution functions (at the nominal beamwidth and accounting for calibration uncertainty), renormalized such that it is unity for the model with the highest marginal probability distribution function value, for this data set, where, in the convention with $L(Q_{\text{rms-PS}} = 0 \mu\text{K}) = 1$, it is 1.5×10^4 for the model with the highest value.

TABLE 19
Numerical Values from Likelihood Analyses Using the Ka4 Data Set

Data Set:	DMR	SP94	SP94	SP94	SP94	SP94	SP94
# ^a	$Q_{\text{rms-PS}}^{\text{b}}$ (μK)	$Q_{\text{rms-PS}}^{\text{c}}$ (μK)	$Q_{\text{rms-PS}}^{\text{d}}$ (μK)	δT_l^{d} (μK)	δT_l^{c} (μK)	Max. ^e	Mar. ^f
(1)	(2)	(3)	(4)	(5)	(6)	(7)	(8)
O1	20.5 – 25.6	16 – 36	25	27	18 – 41	1.0	1.0
O2	23.6 – 29.4	16 – 36	24	28	18 – 41	0.85	0.84
O3	23.6 – 29.4	16 – 37	25	28	18 – 41	0.88	0.89
O4	23.6 – 29.4	17 – 38	25	27	18 – 41	0.92	0.95
O5	23.0 – 28.6	14 – 31	21	28	18 – 41	0.78	0.66
O6	23.0 – 28.6	14 – 32	22	28	18 – 41	0.81	0.71
O7	23.0 – 28.6	15 – 33	22	28	18 – 41	0.85	0.77
O8	20.8 – 25.9	12 – 26	18	28	18 – 42	0.74	0.53
O9	20.8 – 25.9	12 – 27	18	28	18 – 41	0.78	0.57
O10	20.8 – 25.9	12 – 28	19	28	18 – 41	0.83	0.63
O11	18.3 – 22.8	9.3 – 21	14	28	19 – 42	0.70	0.40
O12	18.3 – 22.8	9.7 – 22	15	28	18 – 42	0.74	0.44
O13	18.3 – 22.8	10 – 23	15	28	18 – 41	0.80	0.49
O14	17.7 – 22.0	8.4 – 19	13	28	19 – 42	0.68	0.35
A1	22.8 – 28.4	9.9 – 23	15	28	19 – 43	0.50	0.31
A2	21.1 – 26.3	9.7 – 22	15	28	19 – 42	0.59	0.35
A3	21.1 – 26.3	9.1 – 21	14	28	19 – 43	0.55	0.31
A4	21.1 – 26.3	8.7 – 20	13	28	19 – 43	0.51	0.28
A5	19.8 – 24.7	9.0 – 20	14	28	19 – 42	0.61	0.34
A6	19.8 – 24.7	8.5 – 19	13	28	19 – 42	0.57	0.30
A7	19.8 – 24.7	8.1 – 18	12	28	19 – 43	0.53	0.27
A8	19.0 – 23.7	8.7 – 20	13	28	19 – 42	0.64	0.34
A9	19.0 – 23.7	8.2 – 19	13	28	19 – 42	0.59	0.30
A10	19.0 – 23.7	7.8 – 18	12	28	19 – 43	0.54	0.26
A11	18.5 – 23.1	8.2 – 19	13	28	19 – 42	0.62	0.32
A12	18.2 – 22.7	8.4 – 19	13	28	19 – 42	0.68	0.35
Flat	18.2 – 22.6	12 – 26	18	27	18 – 40	1.0	0.72

^aSee Table 2 for model-parameter values. ^bTwo-year DMR 1σ range accounts for DMR statistical and systematic uncertainties. ^cSP94 1σ ($\sim 68.27\%$ HPD) range, accounting for beamwidth- and calibration-uncertainty corrections. ^dValue at the peak of the calibration-uncertainty-corrected, nominal beamwidth, probability density distribution function. ^eRenormalized maximum values of the probability density distribution functions (at the nominal beamwidth and accounting for calibration uncertainty), renormalized such that it is unity for the model with the highest maximum value of the probability density distribution function, for this data set, where, in the convention with $L(Q_{\text{rms-PS}} = 0 \mu\text{K}) = 1$, it is 180 for the model with the highest value. ^fRenormalized values of the marginalized (over $Q_{\text{rms-PS}}$) probability density distribution functions (at the nominal beamwidth and accounting for calibration uncertainty), renormalized such that it is unity for the model with the highest marginal probability distribution function value, for this data set, where, in the convention with $L(Q_{\text{rms-PS}} = 0 \mu\text{K}) = 1$, it is 4.2×10^3 for the model with the highest value.

TABLE 20
Numerical Values from Likelihood Analyses Using the Q1 Data Set

Data Set:	DMR	SP94	SP94	SP94	SP94	SP94	SP94
# ^a	$Q_{\text{rms-PS}}^{\text{b}}$ (μK)	$Q_{\text{rms-PS}}^{\text{c}}$ (μK)	$Q_{\text{rms-PS}}^{\text{d}}$ (μK)	δT_l^{d} (μK)	δT_l^{c} (μK)	Max. ^e	Mar. ^f
(1)	(2)	(3)	(4)	(5)	(6)	(7)	(8)
O1	20.5 – 25.6	13 – 37	23	26	14 – 42	0.96	1.0
O2	23.6 – 29.4	12 – 37	23	26	14 – 42	0.88	0.91
O3	23.6 – 29.4	13 – 37	23	26	14 – 42	0.90	0.94
O4	23.6 – 29.4	13 – 38	24	26	14 – 42	0.92	0.99
O5	23.0 – 28.6	< 49	20	26	< 65	0.84	0.74
O6	23.0 – 28.6	< 50	20	26	< 65	0.86	0.79
O7	23.0 – 28.6	11 – 33	21	26	14 – 42	0.89	0.83
O8	20.8 – 25.9	< 40	16	26	< 66	0.82	0.60
O9	20.8 – 25.9	< 42	17	26	< 65	0.84	0.65
O10	20.8 – 25.9	< 43	18	26	< 65	0.88	0.69
O11	18.3 – 22.8	< 32	13	26	< 66	0.79	0.47
O12	18.3 – 22.8	< 34	14	26	< 66	0.82	0.51
O13	18.3 – 22.8	< 35	14	26	< 65	0.86	0.55
O14	17.7 – 22.0	< 29	12	26	< 66	0.78	0.42
A1	22.8 – 28.4	< 35	14	26	< 67	0.66	0.43
A2	21.1 – 26.3	< 34	14	26	< 67	0.71	0.45
A3	21.1 – 26.3	< 32	13	26	< 67	0.69	0.41
A4	21.1 – 26.3	< 30	12	26	< 67	0.66	0.38
A5	19.8 – 24.7	< 31	13	26	< 67	0.73	0.43
A6	19.8 – 24.7	< 30	12	26	< 67	0.70	0.39
A7	19.8 – 24.7	< 28	11	26	< 67	0.68	0.35
A8	19.0 – 23.7	< 30	12	26	< 66	0.75	0.42
A9	19.0 – 23.7	< 29	11	26	< 67	0.72	0.38
A10	19.0 – 23.7	< 27	11	26	< 67	0.69	0.35
A11	18.5 – 23.1	< 29	11	26	< 67	0.74	0.39
A12	18.2 – 22.7	< 29	12	26	< 66	0.78	0.42
Flat	18.2 – 22.6	9.2 – 27	17	26	14 – 41	1.0	0.75

^aSee Table 2 for model-parameter values. ^bTwo-year DMR 1σ range accounts for DMR statistical and systematic uncertainties. ^cSP94 1σ ($\sim 68.27\%$ HPD) range for detections, and 2σ ($\sim 97.72\%$ ET) upper limit for nondetections, accounting for beamwidth- and calibration-uncertainty corrections. ^dValue at the peak of the calibration-uncertainty-corrected, nominal beamwidth, probability density distribution function. ^eRenormalized maximum values of the probability density distribution functions (at the nominal beamwidth and accounting for calibration uncertainty), renormalized such that it is unity for the model with the highest maximum value of the probability density distribution function, for this data set, where, in the convention with $L(Q_{\text{rms-PS}} = 0 \mu\text{K}) = 1$, it is 8.3 for the model with the highest value. ^fRenormalized values of the marginalized (over $Q_{\text{rms-PS}}$) probability density distribution functions (at the nominal beamwidth and accounting for calibration uncertainty), renormalized such that it is unity for the model with the highest marginal probability distribution function value, for this data set, where, in the convention with $L(Q_{\text{rms-PS}} = 0 \mu\text{K}) = 1$, it is 220 for the model with the highest value.

TABLE 21
Numerical Values from Likelihood Analyses Using the Q2 Data Set

Data Set:	DMR	SP94	SP94	SP94	SP94	SP94	SP94
# ^a	$Q_{\text{rms-PS}}^{\text{b}}$ (μK)	$Q_{\text{rms-PS}}^{\text{c}}$ (μK)	$Q_{\text{rms-PS}}^{\text{d}}$ (μK)	δT_l^{d} (μK)	δT_l^{c} (μK)	Max. ^e	Mar. ^f
(1)	(2)	(3)	(4)	(5)	(6)	(7)	(8)
O1	20.5 – 25.6	24 – 47	34	38	27 – 53	0.97	1.0
O2	23.6 – 29.4	24 – 47	33	38	28 – 54	0.78	0.79
O3	23.6 – 29.4	24 – 48	34	38	27 – 54	0.82	0.85
O4	23.6 – 29.4	25 – 49	35	38	27 – 54	0.87	0.92
O5	23.0 – 28.6	21 – 40	29	38	28 – 55	0.69	0.60
O6	23.0 – 28.6	21 – 42	30	38	28 – 54	0.74	0.66
O7	23.0 – 28.6	22 – 43	30	38	28 – 54	0.79	0.73
O8	20.8 – 25.9	17 – 34	24	39	28 – 55	0.65	0.47
O9	20.8 – 25.9	18 – 35	25	38	28 – 55	0.70	0.53
O10	20.8 – 25.9	18 – 36	26	38	28 – 54	0.77	0.59
O11	18.3 – 22.8	14 – 27	19	39	28 – 56	0.61	0.35
O12	18.3 – 22.8	14 – 28	20	39	28 – 55	0.66	0.40
O13	18.3 – 22.8	15 – 29	21	38	28 – 55	0.73	0.46
O14	17.7 – 22.0	12 – 25	17	39	28 – 56	0.59	0.31
A1	22.8 – 28.4	15 – 30	21	40	29 – 58	0.40	0.25
A2	21.1 – 26.3	14 – 28	20	40	29 – 57	0.48	0.29
A3	21.1 – 26.3	14 – 27	19	40	29 – 57	0.44	0.25
A4	21.1 – 26.3	13 – 26	18	40	29 – 58	0.41	0.22
A5	19.8 – 24.7	13 – 26	19	40	29 – 57	0.51	0.29
A6	19.8 – 24.7	13 – 25	18	40	29 – 57	0.46	0.25
A7	19.8 – 24.7	12 – 24	17	40	29 – 58	0.42	0.21
A8	19.0 – 23.7	13 – 25	18	39	29 – 56	0.54	0.29
A9	19.0 – 23.7	12 – 24	17	40	29 – 57	0.48	0.25
A10	19.0 – 23.7	12 – 23	16	40	29 – 58	0.44	0.21
A11	18.5 – 23.1	12 – 24	17	40	29 – 56	0.52	0.27
A12	18.2 – 22.7	12 – 25	17	39	28 – 56	0.59	0.31
Flat	18.2 – 22.6	17 – 34	24	38	27 – 53	1.0	0.75

^aSee Table 2 for model-parameter values. ^bTwo-year DMR 1σ range accounts for DMR statistical and systematic uncertainties. ^cSP94 1σ ($\sim 68.27\%$ HPD) range, accounting for beamwidth- and calibration-uncertainty corrections. ^dValue at the peak of the calibration-uncertainty-corrected, nominal beamwidth, probability density distribution function. ^eRenormalized maximum values of the probability density distribution functions (at the nominal beamwidth and accounting for calibration uncertainty), renormalized such that it is unity for the model with the highest maximum value of the probability density distribution function, for this data set, where, in the convention with $L(Q_{\text{rms-PS}} = 0 \mu\text{K}) = 1$, it is 2.4×10^6 for the model with the highest value. ^fRenormalized values of the marginalized (over $Q_{\text{rms-PS}}$) probability density distribution functions (at the nominal beamwidth and accounting for calibration uncertainty), renormalized such that it is unity for the model with the highest marginal probability distribution function value, for this data set, where, in the convention with $L(Q_{\text{rms-PS}} = 0 \mu\text{K}) = 1$, it is 5.8×10^7 for the model with the highest value.

TABLE 22
Numerical Values from Likelihood Analyses Using the Q3 Data Set

Data Set:	DMR	SP94	SP94	SP94	SP94	SP94	SP94
# ^a	$Q_{\text{rms-PS}}^{\text{b}}$ (μK)	$Q_{\text{rms-PS}}^{\text{c}}$ (μK)	$Q_{\text{rms-PS}}^{\text{d}}$ (μK)	δT_l^{d} (μK)	δT_l^{c} (μK)	Max. ^e	Mar. ^f
(1)	(2)	(3)	(4)	(5)	(6)	(7)	(8)
O1	20.5 – 25.6	26 – 50	35	40	29 – 56	0.95	1.0
O2	23.6 – 29.4	25 – 48	35	40	29 – 56	0.86	0.87
O3	23.6 – 29.4	26 – 50	35	40	29 – 56	0.88	0.92
O4	23.6 – 29.4	26 – 51	36	40	29 – 56	0.91	0.97
O5	23.0 – 28.6	21 – 42	30	40	29 – 57	0.81	0.69
O6	23.0 – 28.6	22 – 43	31	40	29 – 56	0.84	0.75
O7	23.0 – 28.6	23 – 44	32	40	29 – 56	0.87	0.81
O8	20.8 – 25.9	18 – 34	25	40	29 – 57	0.78	0.56
O9	20.8 – 25.9	18 – 36	25	40	29 – 57	0.82	0.61
O10	20.8 – 25.9	19 – 37	26	40	29 – 56	0.86	0.67
O11	18.3 – 22.8	14 – 28	20	40	29 – 57	0.75	0.43
O12	18.3 – 22.8	15 – 29	21	40	29 – 57	0.80	0.48
O13	18.3 – 22.8	16 – 30	22	40	29 – 57	0.84	0.53
O14	17.7 – 22.0	13 – 25	18	40	29 – 57	0.75	0.38
A1	22.8 – 28.4	15 – 29	21	41	30 – 58	0.57	0.34
A2	21.1 – 26.3	15 – 28	20	40	30 – 58	0.65	0.38
A3	21.1 – 26.3	14 – 27	19	41	30 – 58	0.61	0.34
A4	21.1 – 26.3	13 – 26	18	41	30 – 58	0.58	0.30
A5	19.8 – 24.7	14 – 27	19	40	29 – 57	0.68	0.37
A6	19.8 – 24.7	13 – 25	18	41	30 – 58	0.64	0.33
A7	19.8 – 24.7	12 – 24	17	41	30 – 58	0.60	0.29
A8	19.0 – 23.7	13 – 26	18	40	29 – 57	0.71	0.37
A9	19.0 – 23.7	12 – 24	17	40	30 – 58	0.66	0.33
A10	19.0 – 23.7	12 – 23	16	41	30 – 58	0.62	0.29
A11	18.5 – 23.1	12 – 24	17	40	29 – 57	0.69	0.34
A12	18.2 – 22.7	13 – 25	18	40	29 – 57	0.75	0.38
Flat	18.2 – 22.6	19 – 36	26	40	29 – 56	1.0	0.77

^aSee Table 2 for model-parameter values. ^bTwo-year DMR 1σ range accounts for DMR statistical and systematic uncertainties. ^cSP94 1σ ($\sim 68.27\%$ HPD) range, accounting for beamwidth- and calibration-uncertainty corrections. ^dValue at the peak of the calibration-uncertainty-corrected, nominal beamwidth, probability density distribution function. ^eRenormalized maximum values of the probability density distribution functions (at the nominal beamwidth and accounting for calibration uncertainty), renormalized such that it is unity for the model with the highest maximum value of the probability density distribution function, for this data set, where, in the convention with $L(Q_{\text{rms-PS}} = 0 \mu\text{K}) = 1$, it is 4.8×10^6 for the model with the highest value. ^fRenormalized values of the marginalized (over $Q_{\text{rms-PS}}$) probability density distribution functions (at the nominal beamwidth and accounting for calibration uncertainty), renormalized such that it is unity for the model with the highest marginal probability distribution function value, for this data set, where, in the convention with $L(Q_{\text{rms-PS}} = 0 \mu\text{K}) = 1$, it is 1.2×10^8 for the model with the highest value.

TABLE 23
Numerical Values from Likelihood Analyses Using the Ka Data Set

Data Set:	...	DMR	SP94	SP94	SP94	SP94
#	$(\Omega_0, h, \Omega_B h^2)$	$Q_{\text{rms-PS}}^{\text{a}}$	$Q_{\text{rms-PS}}^{\text{b}}$	$Q_{\text{rms-PS}}^{\text{c}}$	Max. ^d	Mar. ^e
(1)	(2)	(μK) (3)	(μK) (4)	(μK) (5)	(6)	(7)
O1	(0.1, 0.75, 0.0125)	20.5 – 25.6	18 – 37	26	0.97	1.0
O2	(0.2, 0.65, 0.0175)	23.6 – 29.4	18 – 37	25	0.86	0.87
O3	(0.2, 0.70, 0.0125)	23.6 – 29.4	18 – 37	26	0.89	0.91
O4	(0.2, 0.75, 0.0075)	23.6 – 29.4	19 – 38	26	0.91	0.96
O5	(0.3, 0.60, 0.0175)	23.0 – 28.6	15 – 32	22	0.81	0.69
O6	(0.3, 0.65, 0.0125)	23.0 – 28.6	16 – 32	22	0.84	0.74
O7	(0.3, 0.70, 0.0075)	23.0 – 28.6	16 – 33	23	0.87	0.80
O8	(0.4, 0.60, 0.0175)	20.8 – 25.9	13 – 26	18	0.78	0.56
O9	(0.4, 0.65, 0.0125)	20.8 – 25.9	13 – 27	19	0.82	0.61
O10	(0.4, 0.70, 0.0075)	20.8 – 25.9	14 – 28	19	0.86	0.66
O11	(0.5, 0.55, 0.0175)	18.3 – 22.8	10 – 21	15	0.75	0.43
O12	(0.5, 0.60, 0.0125)	18.3 – 22.8	11 – 22	15	0.79	0.47
O13	(0.5, 0.65, 0.0075)	18.3 – 22.8	11 – 23	16	0.84	0.53
O14	(1.0, 0.50, 0.0125)	17.7 – 22.0	9.3 – 19	13	0.73	0.38
A1	(0.1, 0.90, 0.0125)	22.8 – 28.4	11 – 23	16	0.55	0.34
A2	(0.2, 0.80, 0.0075)	21.1 – 26.3	11 – 22	15	0.63	0.38
A3	(0.2, 0.75, 0.0125)	21.1 – 26.3	10 – 21	14	0.59	0.33
A4	(0.2, 0.70, 0.0175)	21.1 – 26.3	9.7 – 20	14	0.56	0.30
A5	(0.3, 0.70, 0.0075)	19.8 – 24.7	10 – 21	14	0.66	0.37
A6	(0.3, 0.65, 0.0125)	19.8 – 24.7	9.5 – 19	14	0.62	0.32
A7	(0.3, 0.60, 0.0175)	19.8 – 24.7	9.0 – 18	13	0.58	0.29
A8	(0.4, 0.65, 0.0075)	19.0 – 23.7	9.7 – 20	14	0.69	0.37
A9	(0.4, 0.60, 0.0125)	19.0 – 23.7	9.1 – 19	13	0.64	0.32
A10	(0.4, 0.55, 0.0175)	19.0 – 23.7	8.6 – 18	12	0.60	0.28
A11	(0.5, 0.60, 0.0125)	18.5 – 23.1	9.1 – 19	13	0.67	0.34
A12	(1.0, 0.50, 0.0125)	18.2 – 22.7	9.3 – 19	13	0.73	0.38
Flat	...	18.2 – 22.6	13 – 27	18	1.0	0.75

^aDMR 1σ range for open models is from two-year DMR (galactic-frame, quadrupole-excluded) normalization of Górski et al. (1995) (also see RBGS), for flat- Λ models from two-year DMR (ecliptic-frame, quadrupole-excluded) normalization of Bunn & Sugiyama (1995) (also see RS), and for flat bandpower from two-year DMR (galactic-frame, quadrupole-excluded) normalization of Górski et al. (1994). DMR 1σ range accounts for DMR statistical and systematic uncertainties following Stompor et al. (1995) (also see RBGS; RS). ^bSP94 1σ ($\sim 68.27\%$ HPD) range, accounting for beamwidth- and calibration-uncertainty corrections. Lower limits are from -1σ beamwidth analyses, and upper limits from $+1\sigma$ beamwidth analyses (both account for the calibration-uncertainty correction). ^cValue at the peak of the calibration-uncertainty-corrected, nominal beamwidth, probability density distribution function. ^dRenormalized maximum values of the probability density distribution functions (at the nominal beamwidth and accounting for calibration uncertainty), renormalized such that it is unity for the model with the highest maximum value of the probability density distribution function, for this data set, where, in the convention with $L(Q_{\text{rms-PS}} = 0 \mu\text{K}) = 1$, it is 9.5×10^5 for the model with the highest value. ^eRenormalized values of the marginalized (over $Q_{\text{rms-PS}}$) probability density distribution functions (at the nominal beamwidth and accounting for calibration uncertainty), renormalized such that it is unity for the model with the highest marginal probability distribution function value, for this data set, where, in the convention with $L(Q_{\text{rms-PS}} = 0 \mu\text{K}) = 1$, it is 1.9×10^7 for the model with the highest value.

TABLE 24
Numerical Values from Likelihood Analyses Using the Q Data Set

Data Set:	...	DMR	SP94	SP94	SP94	SP94
#	$(\Omega_0, h, \Omega_B h^2)$	$Q_{\text{rms-PS}}^{\text{a}}$	$Q_{\text{rms-PS}}^{\text{b}}$	$Q_{\text{rms-PS}}^{\text{c}}$	Max. ^d	Mar. ^e
(1)	(2)	(μK) (3)	(μK) (4)	(μK) (5)	(6)	(7)
O1	(0.1, 0.75, 0.0125)	20.5 – 25.6	26 – 49	35	1.0	1.0
O2	(0.2, 0.65, 0.0175)	23.6 – 29.4	25 – 48	34	0.88	0.85
O3	(0.2, 0.70, 0.0125)	23.6 – 29.4	26 – 49	35	0.91	0.90
O4	(0.2, 0.75, 0.0075)	23.6 – 29.4	26 – 50	36	0.93	0.96
O5	(0.3, 0.60, 0.0175)	23.0 – 28.6	22 – 41	30	0.82	0.68
O6	(0.3, 0.65, 0.0125)	23.0 – 28.6	22 – 42	31	0.85	0.73
O7	(0.3, 0.70, 0.0075)	23.0 – 28.6	23 – 44	32	0.89	0.79
O8	(0.4, 0.60, 0.0175)	20.8 – 25.9	18 – 34	25	0.79	0.54
O9	(0.4, 0.65, 0.0125)	20.8 – 25.9	19 – 35	25	0.83	0.59
O10	(0.4, 0.70, 0.0075)	20.8 – 25.9	19 – 37	26	0.87	0.65
O11	(0.5, 0.55, 0.0175)	18.3 – 22.8	14 – 27	20	0.75	0.41
O12	(0.5, 0.60, 0.0125)	18.3 – 22.8	15 – 29	21	0.80	0.46
O13	(0.5, 0.65, 0.0075)	18.3 – 22.8	16 – 30	22	0.85	0.52
O14	(1.0, 0.50, 0.0125)	17.7 – 22.0	13 – 25	18	0.75	0.37
A1	(0.1, 0.90, 0.0125)	22.8 – 28.4	16 – 29	21	0.55	0.32
A2	(0.2, 0.80, 0.0075)	21.1 – 26.3	15 – 28	21	0.64	0.36
A3	(0.2, 0.75, 0.0125)	21.1 – 26.3	14 – 27	19	0.60	0.32
A4	(0.2, 0.70, 0.0175)	21.1 – 26.3	13 – 26	18	0.56	0.28
A5	(0.3, 0.70, 0.0075)	19.8 – 24.7	14 – 27	19	0.68	0.36
A6	(0.3, 0.65, 0.0125)	19.8 – 24.7	13 – 25	18	0.62	0.31
A7	(0.3, 0.60, 0.0175)	19.8 – 24.7	13 – 24	17	0.58	0.27
A8	(0.4, 0.65, 0.0075)	19.0 – 23.7	14 – 26	18	0.71	0.36
A9	(0.4, 0.60, 0.0125)	19.0 – 23.7	13 – 24	17	0.65	0.31
A10	(0.4, 0.55, 0.0175)	19.0 – 23.7	12 – 23	16	0.60	0.27
A11	(0.5, 0.60, 0.0125)	18.5 – 23.1	13 – 24	17	0.69	0.33
A12	(1.0, 0.50, 0.0125)	18.2 – 22.7	13 – 25	18	0.75	0.37
Flat	...	18.2 – 22.6	19 – 35	25	1.0	0.74

^aTwo-year DMR 1σ range accounts for DMR statistical and systematic uncertainties. ^bSP94 1σ ($\sim 68.27\%$ HPD) range, accounting for beamwidth- and calibration-uncertainty corrections. ^cValue at the peak of the calibration-uncertainty-corrected, nominal beamwidth, probability density distribution function. ^dRenormalized maximum values of the probability density distribution functions (at the nominal beamwidth and accounting for calibration uncertainty), renormalized such that it is unity for the model with the highest maximum value of the probability density distribution function, for this data set, where, in the convention with $L(Q_{\text{rms-PS}} = 0 \mu\text{K}) = 1$, it is 2.4×10^9 for the model with the highest value. ^eRenormalized values of the marginalized (over $Q_{\text{rms-PS}}$) probability density distribution functions (at the nominal beamwidth and accounting for calibration uncertainty), renormalized such that it is unity for the model with the highest marginal probability distribution function value, for this data set, where, in the convention with $L(Q_{\text{rms-PS}} = 0 \mu\text{K}) = 1$, it is 5.9×10^{10} for the model with the highest value.

TABLE 25
Numerical Values from Likelihood Analyses Using the Ka + Q Data Set

Data Set:	...	DMR	SP94	SP94	SP94	SP94
#	$(\Omega_0, h, \Omega_B h^2)$	$Q_{\text{rms-PS}}^{\text{a}}$ (μK)	$Q_{\text{rms-PS}}^{\text{b}}$ (μK)	$Q_{\text{rms-PS}}^{\text{c}}$ (μK)	Max. ^d	Mar. ^e
(1)	(2)	(3)	(4)	(5)	(6)	(7)
O1	(0.1, 0.75, 0.0125)	20.5 – 25.6	24 – 46	33	0.99	0.99
O2	(0.2, 0.65, 0.0175)	23.6 – 29.4	24 – 45	32	0.99	0.95
O3	(0.2, 0.70, 0.0125)	23.6 – 29.4	24 – 46	33	0.98	0.97
O4	(0.2, 0.75, 0.0075)	23.6 – 29.4	25 – 47	34	0.98	1.0
O5	(0.3, 0.60, 0.0175)	23.0 – 28.6	20 – 38	28	0.98	0.80
O6	(0.3, 0.65, 0.0125)	23.0 – 28.6	21 – 40	29	0.98	0.83
O7	(0.3, 0.70, 0.0075)	23.0 – 28.6	22 – 41	30	0.98	0.87
O8	(0.4, 0.60, 0.0175)	20.8 – 25.9	17 – 32	23	0.97	0.66
O9	(0.4, 0.65, 0.0125)	20.8 – 25.9	18 – 33	24	0.98	0.69
O10	(0.4, 0.70, 0.0075)	20.8 – 25.9	18 – 34	25	0.99	0.73
O11	(0.5, 0.55, 0.0175)	18.3 – 22.8	14 – 26	18	0.97	0.52
O12	(0.5, 0.60, 0.0125)	18.3 – 22.8	14 – 27	19	0.99	0.56
O13	(0.5, 0.65, 0.0075)	18.3 – 22.8	15 – 28	20	1.0	0.60
O14	(1.0, 0.50, 0.0125)	17.7 – 22.0	12 – 23	17	0.99	0.48
A1	(0.1, 0.90, 0.0125)	22.8 – 28.4	15 – 27	20	0.82	0.47
A2	(0.2, 0.80, 0.0075)	21.1 – 26.3	14 – 26	19	0.91	0.50
A3	(0.2, 0.75, 0.0125)	21.1 – 26.3	13 – 25	18	0.87	0.45
A4	(0.2, 0.70, 0.0175)	21.1 – 26.3	13 – 24	17	0.84	0.42
A5	(0.3, 0.70, 0.0075)	19.8 – 24.7	13 – 25	18	0.93	0.48
A6	(0.3, 0.65, 0.0125)	19.8 – 24.7	12 – 23	17	0.90	0.43
A7	(0.3, 0.60, 0.0175)	19.8 – 24.7	12 – 22	16	0.86	0.40
A8	(0.4, 0.65, 0.0075)	19.0 – 23.7	13 – 24	17	0.96	0.48
A9	(0.4, 0.60, 0.0125)	19.0 – 23.7	12 – 22	16	0.92	0.43
A10	(0.4, 0.55, 0.0175)	19.0 – 23.7	11 – 21	15	0.88	0.39
A11	(0.5, 0.60, 0.0125)	18.5 – 23.1	12 – 22	16	0.95	0.44
A12	(1.0, 0.50, 0.0125)	18.2 – 22.7	12 – 23	17	0.99	0.48
Flat	...	18.2 – 22.6	18 – 34	24	0.93	0.69

^aTwo-year DMR 1σ range accounts for DMR statistical and systematic uncertainties. ^bSP94 1σ ($\sim 68.27\%$ HPD) range, accounting for beamwidth- and calibration-uncertainty corrections. ^cValue at the peak of the calibration-uncertainty-corrected, nominal beamwidth, probability density distribution function. ^dRenormalized maximum values of the probability density distribution functions (at the nominal beamwidth and accounting for calibration uncertainty), renormalized such that it is unity for the model with the highest maximum value of the probability density distribution function, for this data set, where, in the convention with $L(Q_{\text{rms-PS}} = 0 \mu\text{K}) = 1$, it is 1.3×10^{19} for the model with the highest value. ^eRenormalized values of the marginalized (over $Q_{\text{rms-PS}}$) probability density distribution functions (at the nominal beamwidth and accounting for calibration uncertainty), renormalized such that it is unity for the model with the highest marginal probability distribution function value, for this data set, where, in the convention with $L(Q_{\text{rms-PS}} = 0 \mu\text{K}) = 1$, it is 2.9×10^{20} for the model with the highest value.